Photocatalytic oxidation of NOx under indoor conditions
a modeling approach

Pelzers, R.S.

Award date:
2013

EINDHOVEN UNIVERSITY OF TECHNOLOGY
MASTER THESIS

Photocatalytic oxidation of NO_x under indoor conditions: A modeling approach

Student
Ruben Pelzers
Wattstraat 21
6533 HM Nijmegen
nl.linkedin.com/in/rspelzers

Eindhoven University of Technology
Den Dolech 2
5612 AZ Eindhoven

Education
Department of the Built Environment

Unit
Unit Building Physics and Services

Specialization
Physics of the Built Environment (Building Materials)

Supervisors
Prof. dr. ir. H.J.H. (Jos) Brouwers
Dr. Q.L. (Qingliang) Yu
Dr. ir. M.G.L.C. (Marcel) Loomans
R.A. (Rizki) Mangkuto, MSc

Abstract

Photocatalytic Oxidation (PCO) technology offers an alternative to common air purification methods for passive application within the built environment. Still, several aspects require improvement, including PCO modeling. Numerical modeling of PCO predicts the indoor dispersion and degradation of pollutants and can be employed to optimize indoor design, including lighting plans and ventilation strategies, to increase the effectiveness of PCO application. The aim of this thesis is to improve the previous PCO modeling [1, 2] and provide additional insight into indoor PCO application. Three numerical modeling studies were performed. The first modeling study demonstrated that a ray-tracing model, built in RADIANCE v.4.1, could support in predicting the actual surface irradiance on the photocatalytic sample. It was found that the reflection of the photocatalytic sample limited the irradiance reduction of the glass cover of the reactor setup. As a result, the irradiance was overestimated slightly, but when darker substrates are used in the experimental setup [3], the overestimation increased and introduced a substantial modeling error. Subsequently, a validated numerical model in Matlab Simulink R2012a was built, to study the highest-obtainable NO_x degradation for ideal mixed flow conditions in the benchmark room [4] and was compared with regular flow conditions during the last study. In the final modeling study, the CFD modeling of [2] was elaborated by implementing a typical office irradiance distribution, different flow conditions and the NO_x kinetic model using an alternative implementation method, to improve the simulation PCO simulation, using ANSYS FLUENT 6.3. The effects of various parameters (e.g. inlet location, turbulent length, source type and volumetric flow rate, NO_x mass flow composition, and photocatalyst dosage) were considered. It was primarily found that that locally under low velocities and high irradiance levels, stagnation may considerably increases local photocatalytic activity. Also, with respect to a regular flow, ideal mixing can increase the NO_x conversion significantly up to circa 49%. Furthermore, it was found that the concentrations of the generated intermediate NO_2 were primarily raised near the photocatalyst-coated wall, while the remaining concentrations in the room were substantially lower. Under specific conditions, however, the kinetic model could not be solved by the continuous solver. The results from this study provided new insights into PCO application and can be used to refine PCO modeling and PCO application in the indoor environment.

Preface

After graduation in building technology from the HBO, during my gap year as building technology engineer, I became interested in the physics of the built environment. I introduced myself into the classical field of physics as a consequence of following online open-courses and reading physics books. In particular, the lectures of Walter Lewin from MIT open course website and the 52-part series '*The Mechanical Universe*' presented by David Goodstein inspired me to explore this territory on my own. Eventually, this was one of the reasons which motivated me to start a supplementary study at the Eindhoven University of Technology, namely Physics of the Built Environment. Later on, during this study, I decided to devote my graduation thesis to photocatalytic oxidation (PCO). This innovative field offered me a learning experience within a wide range of physical-related topics. Moreover, PCO was in line with my previous graduation project from the HBO about green roofs, since both graduation topics were related with air purification.

After a year of working on this thesis, I hope to have actively contributed to the research on PCO, as it may be used as a starting point for future modeling studies that can aid PCO-application into the built environment. During the process, I gained various insights in the application of PCO and user-experience with the RADIANCE, Matlab and FLUENT software. It gave me a healthy appetite to venture further into the field of computational modeling by using state of the art software. Also, I am grateful to the many people who have helped me and gave advice during this process. First of all, I would like to thank Qingliang Yu for his valuable feedback, devoted tutoring and the many discussions and meetings that we had, despite his occupation throughout his PhD completion and the start of his postdoctoral career. Without his guidance and help this report would not have been possible. Secondly, I would like to thank Jos Brouwers for his positive, yet critical view on my work and his valuable advices which helped me throughout my process. Also, I would like to thank Marcel Loomans for his dedicated supervision and his immediate response to all of my CFD-related questions. Furthermore, I am grateful to Rizki Mangkuto for his support and advice during both the radiance modeling and during our visit to the 11th International Radiance Workshop in Copenhagen. Finally, I wish to thank my parents for their support and encouragement throughout my study and graduation process.

Contents

Chapter 1. **Introduction**

1.1. **Prologue**

Indoor air quality (IAQ) refers to air quality within buildings and transport vehicles wherein the health and comfort of occupants is considered. The IAQ is affected by air pollution, such as biological contaminants, particulate matters (PM_x), gasses (e.g. CO_x, SO_x, NO_x, VOCs) or radon, and leads to discomfort and adverse health effects among occupants. Recently, the World Health Organization (WHO) reported that indoor smoke from solid fuels is the number ten of global risks for mortality worldwide and listed indoor air pollution in 2004 as the second largest cause for lung cancer [5]. In particular, people in modern urban areas spend 85%-90% of their lives indoor [6]. Moreover, worldwide, 30% of the new and reconstructed buildings are estimated to be a source of extreme complains related to IAQ [7], partially caused by poor mechanical ventilation [8]. Meanwhile in the previous decades, huge changes occurred in indoor application of building materials and consumer products [9]. These products release a range of chemicals, resulting in indoor air pollution and a loss of IAQ [10, 11, 12, 13].

Consequently, international organizations, such as the European Union [14], WHO [15] and Environmental Protection Agency (EPA) [16], defined standards and guidelines for maximal concentration levels and product-related emissions, based on numerous risk assessments and evaluation reports, to limit exposure of indoor pollutants to occupants. Up to this day however, only modest regulations for limitation or prevention of exposure to product-related emissions exist within the US and Europe [14], thereby hindering complete coverage. Most information on pollutants is available for carbon oxides, nitrogen oxides, radon, asbestos and organic compounds. Nonetheless, exposure of occupants to indoor pollutants consists of a complex mixture of substances from different sources that can mutually contribute to toxic effects, while most toxicology data refer to exposures to single substance [17]. Also, the effects of other pollutants, such as secondary pollutants created by indoor chemistry or various microorganisms, are still underexposed [18].

Generally, pollutants are removed from the indoor environment by source control, increasing ventilation rates or air purification. Nevertheless, in most circumstances, air purification remains the most feasible option [19], although common air purification methods only adsorb a selective range of pollutants. However, more advanced methods, such as photocatalytic oxidation (PCO), ozone generators or thermal oxidation destruction, offer alternatives [20]. Also, recent research demonstrates that the capabilities of plants and organisms to degrade organic pollutants may effective contribute to air purification [21].

Possibly, PCO is a potential technology for indoor air purification, because it degrades a wide range of pollutants, both organic and inorganic. Conversely, current PCO research is primarily focused on the development of photocatalytic reactors, kinetic models and photocatalysts, while the practical application in the built environment is rarely discussed. Moreover, the current photocatalysts ineffectively degrades indoor pollutants. As a result, applications in HVAC systems or mobile PCO units have relatively high power consumption and there is incomplete data on the complexity of the PCO process [22]. During the photocatalytic degradation process, pollutants can be incompletely destroyed and in doing so create new pollutants that negatively affect the health of occupants. Nonetheless, a photocatalyst can be applied to a wide range of building materials, such as glass, plastics and cementitious materials [23]. Therefore, PCO offers an alternative to common air purification methods for passive application. Still, various aspects require improvement, including PCO modeling. Clearly, modeling of PCO application in the built environment may predict the dispersion and degradation of pollutants in indoor spaces. In turn, various aspects can be optimized indoors, such as lighting plans and ventilation strategies.

1.2. Problem statement

In previous work on PCO modeling [1, 3], a kinetic model for NO_x was developed and validated. This kinetic model describes the photocatalytic degradation of the inorganic pollutant nitrogen monoxide (NO) under indoor conditions. In the experiments, NO was supplied into a reactor under indoor conditions and was successively converted to nitric acid (HNO_3) by visible light (400-570 nm) on a photocatalyst (C-doped TiO_2), while nitrogen dioxide (NO_2) was generated as an intermediate substance [1]. Furthermore, in a follow-up study [2], this kinetic model was implemented in a CFD model to predict the NO_x degradation in both the reactor [3] and in the benchmark room model [4].

In the majority of the CFD models [2], low NO_x conversions of 0-4% were obtained. As a result, it was questioned by which amount the conversion of NO_x could be amplified through optimizing the flow conditions in the room for increased performance. Furthermore, [2] proposed a volume-based implementation method to implement the kinetic model into CFD model. However, the required height of the cell volume was not incorporated. Consequently, the cell volume affected the NO mass flow created by the kinetics and may be a potential source of physical modeling errors in future modeling work.

Also, recent research [1, 2, 3] considered the irradiance field only to a modest degree, raising the number of required assumptions in both the kinetic model and CFD models. For example, during the kinetic model development on NO_x [1], the influence of the reactor setup on the received irradiance by the photocatalyst was neglected, causing a potentially chance on errors in the irradiance approximation. Similarly, during the CFD modeling of the benchmark room, it was assumed that the photocatalyst-coated walls were uniformly irradiated by 10 W m^{-2} [2]. Moreover, examination of the interdependent relationship between the available irradiance and the required illuminance levels for occupant activities inside the room was excluded from the previous study. Therefore, the available radiation for photocatalytic activity in the room may differ considerably from what is anticipated. Additionally, in recent years, it has been demonstrated how basic radiance modeling in photocatalytic reactors can be performed [24, 25, 26]. However, these radiance modeling efforts are only valid for reactor systems and can therefore predict the distribution only within simple geometries. In contrast, PCO modeling in the indoor environment requires more complex modeling approach to incorporate the large geometry in which various materials are applied. Therefore, a more comprehensive approach is required.

1.3. Objectives

The prime objective of this thesis is to contribute to PCO-related research by: employing and incorporating a radiance model into the previous PCO modeling studies; estimating the optimization potential of NO_x conversion under idealized flow conditions; extending the previous CFD research to develop a more accurate PCO modeling approach; and gain better understanding of the PCO mechanisms inside a room. Consequently, the numerical modeling efforts in this work may assist the future modeling studies in the implementation and observation of PCO application in the built environment. In order to achieve the prime objectives, three modeling studies were performed, for which several research questions are formulated in the next section.

1.4. Research questions

1) How can the irradiance behavior inside a photocatalytic reactor influence the removal efficiency of NO_x by a photocatalytically active sample?
2) What is the photocatalytic removal efficiency of NO_x in a ideally mixed room?
3) How does a typical irradiance distribution of an office and different flow fields influence the photocatalytic removal efficiency of NO_x and IAQ?
4) What is the assessment capability of the $NO_{x_{con}}$ performance indicator for the photocatalytic removal efficiency of NO_x, when different external pollution sources for different ACH values are considered?
5) How does the turbulent intensity at the inlet affect the photocatalytic degradation of NO_x?
6) How does the catalyst dosage influence the photocatalytic degradation of NO_x when a regular or ideal mixed flow is assumed?

1.5. Modeling framework

Before proceeding, it would be beneficial to establish a modeling framework to provide an overview, as defined in Figure 1. The framework offers an overview of the modeling requirements and serves as a starting point for PCO modeling in the built environment. In the last simulation study (Chapter 6), the framework is applied as basic structure for modeling.

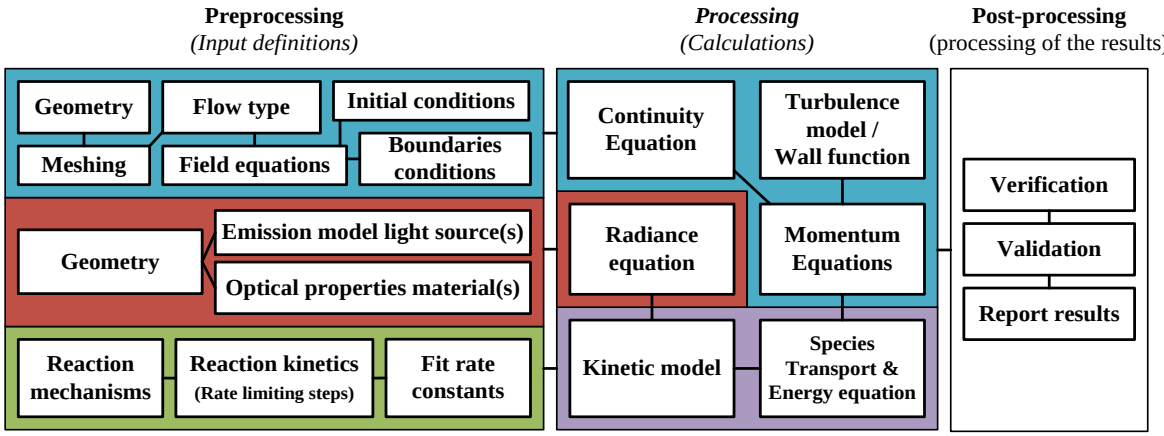

Figure 1: A modeling framework for photocatalytic modeling in the built environment: consisting of a preprocessing, simulation and post-processing phase.

As can be seen from Figure 1, the framework is composed out of three phases: preprocessing, processing and post-processing. The input parameters define the conditions of the studied system and are subdivided into Computational Fluid Dynamics (CFD) (see Figure 1: *blue and purple*), radiation modeling (*red*) and kinetic modeling (*green*). The current principles of the kinetic modeling are based on of Langmuir-Hinshelwood kinetics (L-H kinetics). During the CFD simulation the set of (coupled) partial differential equations (PDE) are solved, which normally consist of the continuity equation and momentum equations (*blue*). Dependent on the flow characteristics, additional models (e.g. turbulence model and wall functions) are added (*blue*). Simultaneously, CFD modeling of PCO is expanded by species transport equations (*purple*) to predict pollutant dispersion and (de-)generation of pollutants [2], as result of PCO. The kinetic model for PCO reactions (*purple*) is integrated into the CFD model by user-defined equations function. After simulation, the post-processing begins; the results are verified, validated and reported.

1.6. Research results

The objective of this thesis was to examine and improve the PCO modeling of NO_x at typical indoor air levels using modified titanium dioxide under typical indoor lighting. In the current work, several measurements and three numerical studies were performed in which (1) the rate constant in the kinetic model of NO_x [1] was corrected for the optical properties of the reactor; (2) a computational model was constructed which successfully predicted the experiment results from [3] and the conversion of NO_x in a ideally mixed room; (3) following by an alternative implementation method for incorporating the kinetic model into CFD to analyze the conversion of NO_x in the benchmark room using commercial CFD software for additional parameters such as required illuminance levels, turbulent intensity, catalyst dosage and ideal mixing.

1.7. Reading structure

A reading structure is provided to accommodate further reading and understanding of this work. First of all in this current chapter, the necessity for and current state of research on PCO modeling was shortly described. Also, the problem, objectives, research questions and main results were identified. In the following chapter, Chapter 2, the background on PCO and NO_x degradation, and a deeper understanding in the theory of (spectral) radiance modeling in RADIANCE, reactor modeling and alternative kinetic model implementation into CFD is provided. Following with the experimental work needed for the radiance modeling, which is reported in Chapter 3. Then, in Chapter 4, the first modeling study is presented, in which a more accurate understanding of the irradiance behavior in the reactor setup is obtained, resulting the refinement of a rate constant in the kinetic model of NO_x. In Chapter 5, the second modeling study reports on the modeling of both the ideal plug flow reactor and the ideally mixed room, by using the improved kinetic model for investigation of the photocatalytic performance under ideal mixed flow conditions. Next in Chapter 6, the third modeling study illustrates how irradiance data from a radiance model is integrated into several CFD models to provide more accurate results of the photocatalyst performance, based on the benchmark room model. In addition, including the effect of flow, required illuminance, turbulence at the inlet, different pollution types and catalyst dosage values are studied for a number of cases. Finally, 0 summarizes the foremost conclusions of this thesis and proposes recommendations. Prior to the experimental and simulation studies, the theory is explained first in the following chapter.

Chapter 2. **Theory**

2.1. **Initial principles of photocatalytic oxidation**

Currently, the anatase mineral form of titanium dioxide (TiO_2) is primarily selected as photocatalyst for photocatalytic oxidation (PCO) technology. Still, other semiconductors such as ZnO, ZnS, CdS, Fe_2O_3, SnO_2 may also serve as photocatalysts. TiO_2, however, is preferable, since it is relatively inexpensive and easily produced, chemically and biologically inert [19], photocatalytically stable and harmless for humans [2]. For example, TiO_2 is used as food coloring substance (E171). TiO_2 can be prepared in powder, crystals or thin films, ranging from a few nanometers (nm) to numerous micrometers (μm). Mainly two crystal modification of TiO_2 are applied; rutile and anatase with band gaps of 3.02 eV and 3.20 eV respectively. The band gaps of the rutile and anatase crystal modification allow irradiation below 384 and 410 nm (UV light) to initiate the PCO of indoor pollutants [27]. While the radiation from the sun contains 3-5% UV light (< 84 Wm^{-2}) (83), only < 0.05 Wm^{-2} UV light is emitted by indoor lighting causing extremely low PCO activity indoors. In turn, modification of the photocatalyst allows lower band gap energies, resulting in adsorption of radiation with larger wavelengths (> 410 nm). For example, in a recent study [28], the band gap of the photocatalyst was reduced to 2.1 eV by doping metals or non-metals materials onto the photocatalyst. Also, in the previous research on NO_x [3], a C-doped TiO_2 catalyst with a band gap of 2.32 eV was applied, resulting in PCO activities under visible light up to 524 nm (green-blue).

Fundamentally, a photocatalyst facilitates the creation of photo-induced redox reactions, allowing the transfer of electrons between substances which creates ions or radicals as can be seen in Figure 2. Figure 2 illustrates the initial PCO process on a photocatalyst particle in a coating, enriched with a photocatalyst. Physically, PCO is initiated by absorbing a photon with $hv \geq E_g$ (E_g [eV] is the minimum required energy for excitation), that induces the excitation of an electron/hole pair, creating an electron (e^-) and a hole (h^+) in the photocatalyst (PC). The excitation process is frequently described by the band gap theory. In short, this theory considers the discrete energy of individual electrons as a collective energy state of the system in the form of bands [29].

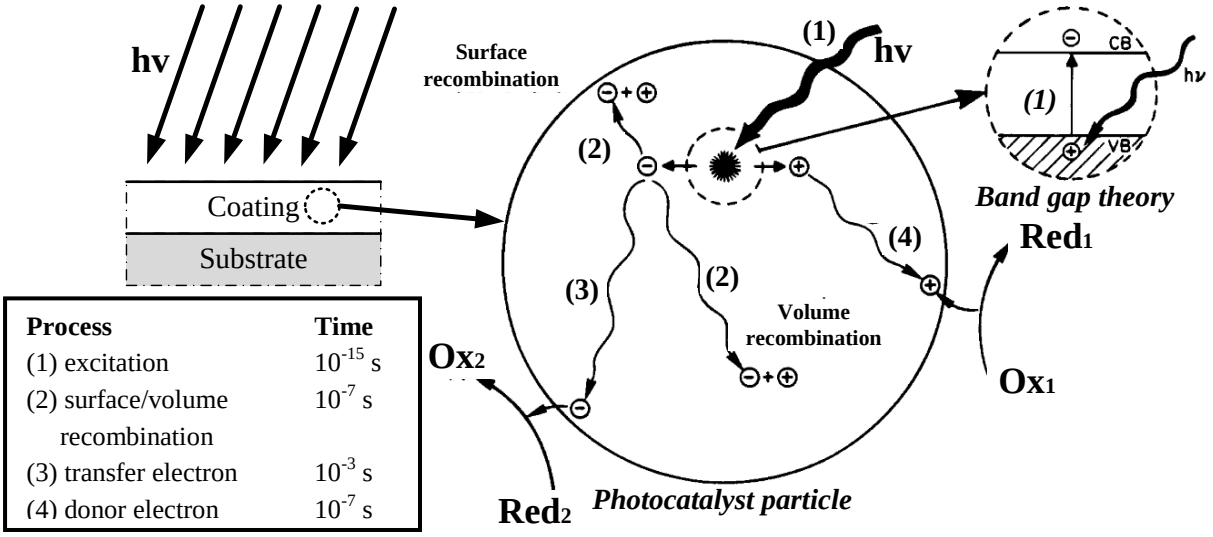

Figure 2: Schematic representation of the steps in a photocatalytic reaction on a TiO_2 particle [30, 31]. (1) Excitation of the e^-/h^+ pair by a photon; (2) Surface and volume recombination of the e^-/h^+ pair; (3) Transfer of the electron to an adsorbed oxidizable substance on the conduction band and (4) donation of another electron from an absorbed reductable particle to the photocatalyst particle.

The free electron, created by the excitation of a photon expressed by equation (2-1), is transferred to an adsorbed reducible substance on the surface ($Ox_{1_{ads}}$), creating a reduced substance ($Red_{1_{\mathrm{ads}}}$) on the conduction band (see Figure 2: 3), as described by equation (2-3). Simultaneously, the catalyst accepts another electron from an adsorbed oxidizable substance ($Red_{2_{ads}}$), filling the hole and creating an oxidized substance ($Ox_{2_{ads}}$) on the valence band (see Figure 2: 4), as reported by equation (2-4). Depending on the chemical composition, the newly created adsorbed substances ($Ox_{2_{\mathrm{ads}}}$ & $Red_{1_{ads}}$) can desorb from the surface. However, they can also react with the catalyst, or react with other adsorbed substances. The photocatalyst remains unaltered in the overall process, as the net flow of electrons remains null [32]. The remaining electron/hole pairs recombine either on the surface or in the volume (see Figure 2: 2) which creates heat, as expressed by equation (2-2).

$$PC \xrightarrow[h\nu \geq E_g]{} PC\ (e^- + h^+) \tag{2-1}$$

$$h^+ + e^- \rightarrow \Delta H\ (heat) \tag{2-2}$$

$$Ox_1 \rightarrow Ox_{1_{ads}} \qquad e^-_{cb} + Ox_{1_{ads}} \rightarrow Red_{1_{ads}} \tag{2-3}$$

$$Red_2 \rightarrow Red_{2_{ads}} \qquad h^+_{vb} + Red_{2_{ads}} \rightarrow Ox_{2_{ads}} \tag{2-4}$$

Despite the fact that, during the photocatalytic degradation, the primary reactions are induced on the photocatalyst by photons, newly-created intermediates, including reactive oxygen species (i.e. radicals) or ions, can initiate secondary reactions via oxidation with other molecules [31]. This adds up to the network of chemical reactions in the overall degradation pathway of a pollutant. Experimental studies on toluene suggest that the degradation network of a pollutant can be complex, since during degradation up to 30 different intermediates can be generated dependent on the composition of the carrier gas [5, 33, 34, 35]. For example, [5] demonstrated that water vapor influences the intermediate generation. However, for smaller molecules, such as NO or NO_2, which have a low molecular weight and are composed of a few atoms, the degradation network is less complex, as will be explained in the following section.

2.2. The photocatalytic degradation mechanism of NO_x

In this thesis, NO and NO_2, also referred to as respectively nitrogen monoxide and nitrogen dioxide, are the target pollutants during the modeling studies. Generally, these mono-nitrogen oxides are denoted in literature by a generic term, NO_x, as done in the title.

NO_x is mainly formed in ambient air by several combinations of oxygen and nitrogen at high temperatures during the combustion process. In a typical household, it is estimated that in a typical household an emission of 1 μg s^{-1} NO_x is released [36], predominantly because of combustion. During typical combustion processes, 90-95% of the NO_x is emitted as NO and 5–10% as NO_2, but varies per source [37]. However, the formation of NO_x near the building dependent on local conditions and originates from a wide range of both human activities, mainly from combustion of fossil fuel, but also natural processes, such as lighting, biomass burning and microbiological emissions from soil [38]. Typically, a range for NO_x concentration between 1-366 μg m^{-3} can be found outdoors, while in the indoor environment NO_x concentrations may range between 1-264 μg m^{-3} [39]. The suggested reaction mechanism for NO_x degradation by [3] is discussed and supplemented below, while considering synthetic air as carrier gas composed out of nitrogen, oxygen and water.

As already was stated in Section 2.1, the mechanism of photocatalytic degradation is initiated by excitation of an electron/hole, as was expressed by equation (2-1). To promote reacting electron/hole pairs, it is essential that the reactants are adsorbed according to [3]:

$$H_2O \rightleftharpoons H_2O_{ads} \tag{2-5}$$

$$NO \rightleftharpoons NO_{ads} \tag{2-6}$$

$$O_2 \rightleftharpoons O_{2_{ads}} \tag{2-7}$$

Now, the trapping of the generated holes and electrons may occur by the following reaction scheme [3]:

$$h^+ + H_2O_{ads} \rightarrow OH^\bullet + H^+ \tag{2-8}$$

$$e^- + O_{2_{ads}} \rightarrow O_2^-{}_{ads} \tag{2-9}$$

The remaining generated holes and electrons recombine, according to [3]:

$$e^- + h^+ \rightarrow \Delta H\ (heat) \tag{2-10}$$

In turn, [3] proposes that the absorbed NO is attacked by the $OH^{\cdot}$ radical via oxidation creating nitrous acid, nitrogen dioxide and eventually nitrate which reacts to nitrate and a hydrogen ion [3]:

$$NO + OH^\bullet \rightarrow HNO_2 \tag{2-11}$$

$$HNO_2 + OH^\bullet \rightarrow NO_2 + H_2O \tag{2-12}$$

$$NO_2 + OH^\bullet \rightarrow NO_3^- + H^+ \tag{2-13}$$

Eventually, nitric acid (HNO_3), under indoor conditions a colorless liquid, is created from equation [1].

While in the previous reaction equations the effect of the adsorbed oxygen ion, created in equation (2-9), was not considered, associated literature is used to extend the theory. However, this additional theory is not applied further in this thesis, but is only described to support future work. To begin with, several sources suggest that, the hydrogen ion in equation (2-14) may react with an oxygen ion creating a hydroperoxyl radical [40, 41]:

$$O_2^-{}_{ads} + H^+{}_{ads} \rightarrow HO_2^\bullet \tag{2-14}$$

Subsequently, two hydroperoxyl radicals react to produce hydrogen peroxide via a reduction on the conduction band [40, 41] or react directly [31]:

$$HO_2^\bullet + H^+ + e^-{}_{cb} \rightarrow H_2O_2 \tag{2-15}$$

$$2HO_2^\bullet \rightarrow H_2O_2 + O_2 \tag{2-16}$$

Then, the hydrogen peroxide reacts via the catalyst to form two hydroxide [40]. The hydrogen peroxide can be adsorbed on the catalyst and react with an oxygen ion [40, 41, 42, 43], or (while adsorbed) react with an electron on the conduction band [31]:

$$H_2O_{2_{ads}} + O_2^-{}_{ads} \rightarrow OH^- + OH^\bullet + O_2 \tag{2-17}$$

$$H_2O_{2_{ads}} + e^-{}_{cb} \rightarrow OH^- + OH^\bullet \tag{2-18}$$

In turn, the created hydroxyl ion (OH^-) would presumably donate an electron to the catalyst:

$$OH^-_{ads} + h^+_{vb} \rightarrow OH^\bullet \tag{2-19}$$

Now, the reaction mechanism of water and oxygen with the photocatalyst can be proposed, creating a net flow of zero electrons, by substituting equations (2-5), (2-7), (2-8), (2-14), (2-15), (2-18) and (2-19) to:

$$O_2 + 3e^- + 3h^+ + 2H_2O \rightarrow 4OH^\bullet \tag{2-20}$$

Additionally, the net reaction of photocatalytic degradation of NO_x in in air can be proposed, using oxygen and water, whereas the remaining gasses (i.e. N_2) remain inert during the reaction. First, equations (2-6), (2-11), (2-12) and (2-13) are substituted to a reaction scheme which is formulated as:

$$NO + 3OH^\bullet \rightarrow HNO_3 + H_2O \tag{2-21}$$

Consequently, equation (2-20) is combined with equation (2-21) to propose the net reaction:

$$4NO + 3O_2 + 9e^- + 9h^+ + 6H_2O \rightarrow 4HNO_3 \tag{2-22}$$

The net reaction, expressed by equation (2-22), provides the ratios between the reacting compounds for 100% conversion of NO_x in synthetic air.

In the majority of the experimental studies, synthetic air is applied as the carrier gas. Normally, in line with [3], a composition of 80% nitrogen (N_2) and 20% oxygen is used [33, 44]. However, noble gasses such as helium (He) and argon (Ar) are frequently applied as substitute for N_2 [45, 46]. Noble gasses are also considered to be inert, because the outer electron shell of these gasses is saturation by electrons and therefore are not affected by oxidation. The effect of N_2 on PCO is also neglected, as the bond energy of N_2 (945 kJ mol^{-1} ≈ 9.8 eV $molecule^{-1}$), known from the Haber-Bosch process (nitrogen fertilizer production), is considered to be one of the strongest bonds [47]. In the next Section, the theory on irradiance dispersion modeling is elaborated which is required to predict the amount of photons which initiate the surface reaction on the photocatalyst and is used in the modeling studies.

2.3. Modeling irradiance dispersion using ray-tracing in RADIANCE

The irradiance dispersion in a system, being either a room or reactor, has a major impact on the perceived irradiance by a photocatalyst and thus influences the generation of electron/hole pairs. Normally, the irradiance dispersion in an arbitrary system can be modeled by either a physical approach, based on electromagnetic wave theory [48], or by more conventional geometric optical methods [49]. Within the built environment, geometric optical methods, such as ray-tracing (forward or backward) or radiosity methods, are frequently employed for lighting simulation and may also be used for other types of electromagnetic radiation. These methods approximate the particle or wavelike behavior of light by a large number of narrow beams (rays) which travel instantaneous between surfaces through a vacuum. Therefore, interference, diffraction or polarization effects cannot be taken into account.

The radiocity method is a view independent rendering method in which light is traced from a light source and is reflected diffusely a specific number of times. During rendering, all surfaces are considered opaque and behave as perfect diffuse reflectors (Lambertian reflection). In turn, the ray-tracing method is a view dependent method for rendering an image by the tracing light particles from the viewpoint back to the light source (backward ray-tracing) or vice versa (forward ray-tracing). In this thesis, the backward ray-tracing method is employed, for modeling the irradiance dispersion, by using the software-package RADIANCE.

RADIANCE development began in the last 90's for the UNIX computers and is used free of charge [50]. The software-package is composed out of 100 different programs, functioning as modules, creating and simulating a model via a text-based file structure (ASCII formats), defining the geometry, materials, luminaire data and scenes of the radiance model. In contrast to MS Windows and the Mac OS, the UNIX philosophy does not provide GUI-based interface, but provides highly modular software. In turn, this allows huge flexibility, but limits flexibility with what the user knows [51].

In RADIANCE, objects and light sources are defined by a geometry and material. Sequentially, the material definition is specified by a material type, but can be extended by a texture or a pattern function. While the texture function influences the reflected spectrum (color), the pattern function influences the amount of reflection, also commonly referred to as bump mapping. The material type characterizes the behavior of the material from a set of predefined reflection/transmission models, such as the *mirror*, *dielectric*, or *metal* material types. Both the materials and geometries are created with different text files; with a **.mat* and **.rad* extension respectively. During modeling, dimensions can be specified in any unit as long as the units are consistent throughout the model. Alternatively, geometries can be imported from CAD files. Before a radiance model can be processed, the model files are compiled to a single **.oct* file (octree) via the *oconv* command, allowing accelerated calculation times. Scenes are defined in **.rv* files and are collectively used with an **.oct* file in a rendering command (the *rvu* command). Also, predefined sampling point can be calculated and deported to a text file [51]. RADIANCE can render direct image or save it as numerical data; either contour plot or image. In Figure 3, the main components of the software-package RADIANCE are illustrated.

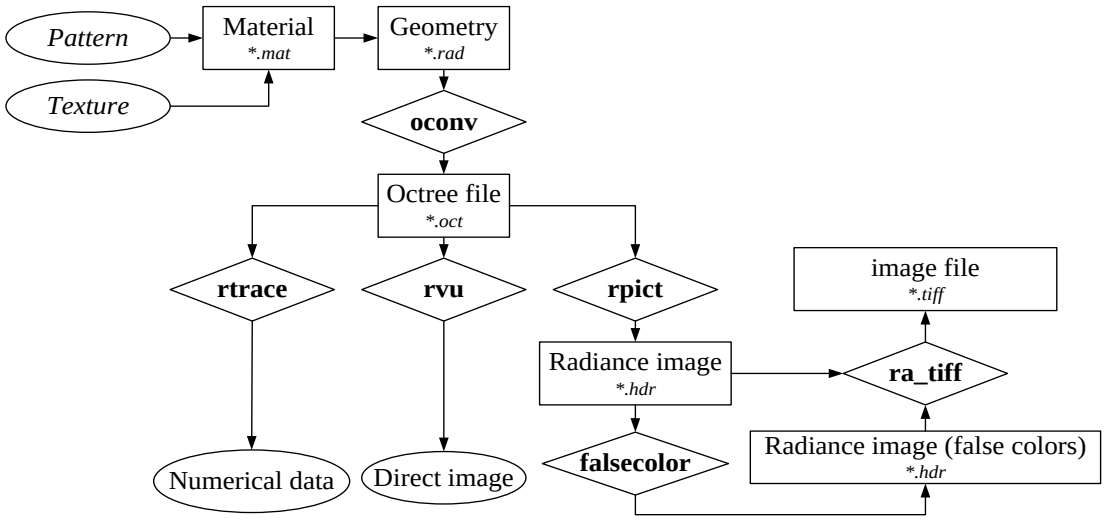

Figure 3: The main components of the software-package RADIANCE. The bold printed texts in the diamonds are commands (programs), whereas texts in the rectangles represent files. The texts in the ellipses are not specified.

During rendering, RADIANCE calculates the trichromatic light dispersion for the values, Red, Green and Blue (RGB) separately and sums them up to a single value, according to the RADIANCE RGB model, to incorporate the sensitivity of the human eye for the visual range. However, there are more commonly accepted weighting functions, based on the trichromatic theories primarily developed at the International Commission on Illumination (CIE) [52]. The calculation method in RADIANCE allows spectral rendering for certain spectrum intervals, without applying the RADIANCE RGB model [53], by using the radiance equation. The radiance equation and solving algorithms are shortly described in the next section.

2.4. The radiance equation and solving algorithms in RADIANCE

2.4.1. The radiance equation, reflection and emission

The backward ray-tracing method in RADIANCE calculates the outgoing radiance (L_o) as the sum of total reflected radiance (L_r) and emitted radiance (L_e) on a surface (dA) to another surface in a spherical coordinate system, defined by the radiance equation [52]:

$$L_o(\psi_o, \theta_o) = L_e(\psi_o, \theta_o) + L_r(\psi_o, \theta_o, \psi_i, \theta_i) \tag{2-23}$$

Where $L_o(\psi_o, \theta_o)$ [Wsr^{-1}m^{-2}] is the outgoing radiance in a direction given by the angles ψ_o and θ_o expressed in [radials]; which is composed out of $L_e(\psi_o, \theta_o)$ [Wsr^{-1}m^{-2}], the emitted radiance, and $L_r(\psi_o, \theta_o, \psi_i, \theta_i)$ [Wsr^{-1}m^{-2}], the reflected radiance [54] as function of the incoming angles ψ_i and θ_i and outgoing angles φ_o and θ_o, given in [radials]. In turn, the reflection is written as a function of the incoming radiation (L_i) [52]:

$$L_r(\psi_o, \theta_o, \psi_i, \theta_i) = \int_{\psi_i} \int_{\theta_i} f_r(\psi_o, \theta_o, \psi_i, \theta_i) L_i(\psi_i, \theta_i) |cos(\theta_i)| \, sin(\theta_i) \, d\theta_i d\psi_i \tag{2-24}$$

Where $f_r(\psi_o, \theta_o, \psi_i, \theta_i)$ [sr^{-1}] is the reflection model as function of outgoing angles ψ_o and θ_o and the incoming angles ψ_i and θ_i, given in [radials]. Furthermore, the L_i [W sr^{-1}m^{-2}] is the incoming irradiance from a specific projection, as function of the incoming angles (ψ_i and θ_i [radials]) of the incoming ray representing that projection. The incoming radiance is integrated over the incoming angles or solid angle Ω_i [sr] of the incoming radiance. The solid angle is a 2-dimensional angle with represent the domain of incoming/outgoing directions of radiation and is related to first angle θ [radials] and the second angle ψ [radials] by [55]:

$$d\Omega = sin(\theta) \, d\psi d\theta \tag{2-25}$$

The maximum domain of Ω for surface is 2π (a hemisphere). Furthermore, the total radiance flux (ϕ [W]) on dA is related to the radiance (L [Wsr^{-1}m^{-2}]) or irradiance (E [Wm^{-2}]), described by:

$$L = \frac{d^2\phi}{dA d\Omega \, cos\,\theta} \approx \frac{\phi}{A\Omega \, cos\,\theta} = \frac{E}{\Omega \, cos\,\theta} \tag{2-26}$$

Where A [m^2] is the area of the surface; Ω [sr] is the solid angle of the radiance (L). In Figure 4, a schematic illustration is given of the radiance equation.

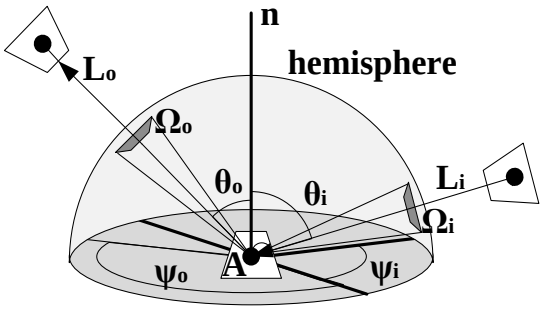

Figure 4: Schematic representation of radiance equation and corresponding variables; equation (2-23) and (2-24).

The reflection of a surface in RADIANCE is either described by a Bidirectional Reflectance Distribution Function (BRDF) or, when transmission is included, by a Bidirectional Reflectance Transmittance Distribution Function (BRTDF). The BRDF function is approximated by a reflection model or is obtained from experimental data in which the actual angular distribution of the surface reflection is measured [56], typically obtained with a gonioreflectrometer [57]. The BRDF is defined as [58]:

$$f_r(\theta_i, \psi_i, \theta_o, \psi_o) = \frac{L_r(\theta_i, \psi_i, \theta_o, \psi_o)}{E_i(\theta_i, \psi_i)} \tag{2-27}$$

Where f_r [sr^{-1}] is the BRDF function; E_i [Wm^{-2}] is the incoming irradiance; and L_r [$Wm^{-2}sr^{-1}$] is the reflected radiance. The Lambertian reflection model is the most basic reflection model for the BRDF. The model approximates an ideal diffuse reflection, based on Lambert's cosine law expressed by [58]:

$$f_r = f_{Lambertian} = \frac{\sigma}{\pi} \tag{2-28}$$

Where σ [-] is the reflection coefficient (albedo). In general, a Lambertian surface reflects radiant flux (ϕ_A [W]) from any point A with a cosine angular distribution independent. This implies that any viewable point seen from point A at equal distance receive the same E [Wm^{-2}]. As a result, the surface at point A appears equally bright from all viewing angles (θ_o, ψ_o) [55]. In nature, there are no actual Lambertian surfaces and only a limited number of surfaces can accurately be approximated by equation (2-28), including matte paper [55]. Therefore, most surfaces are more accurately defined by a more comprehensive reflection model.

In RADIANCE, complex reflection behavior can be approximated by predefined BRDF models combine an additive mixture of ideal reflection types from which reflection is generated [58], including perfect diffuse (f_d) and specular reflection (f_s), as illustrated in Figure 5. These predefined reflection models, such the material types *plastic*, *metal* [51], are defined by a reflection coefficient (σ [-]) and a specular component (S [-]) which may be acquired by an integrating sphere-based photospectrometer such as the Minolta CM-2001 [52]. While the S of non-metallic surfaces rarely exceed 6%, polished metal surfaces may have an S of <50% [52]. Both *plastic* and *metal* models are nearly identical, although plastic does not correct the specular component (or specular highlight) for the color, in contrast to *metal* [56].

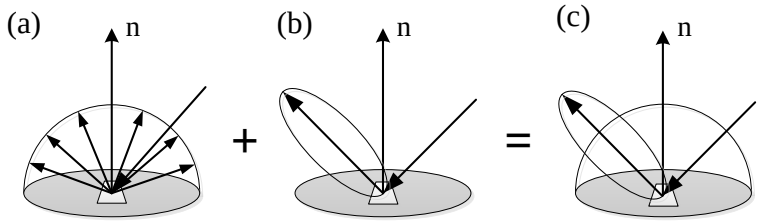

Figure 5: Components of a general BRDF model: (a) diffuse reflection; (b) Specular reflection; (c) Both components.

In line with reflection, the emission of a light source may be modeled by a comparable method, in which the source is either described by material type or obtained from photometric data, using a moving-cell photometer [59]. The material type *light* is applied as light source material in this thesis and emits radiation perpendicular to the surface on which the material type is applied. In turn, the radiation [L_l] is related to the total radiant flux of the light source (ϕ_l [W]) and the light source surface (A_l [m^2]) by [59]:

$$L_l = \frac{\phi_l}{\pi A_l} \tag{2-29}$$

2.4.2. Solving algorithms in RADIANCE

Typically, the radiance equation used in the ray-tracing technique is solved by a deterministic or a stochastic solving algorithm. While the stochastic ray-tracing technique causes interference in the simulation results, it is frequently more accurate as the deterministic ray-tracing approach [52]. However, neither a deterministic nor a stochastic method is entirely satisfactory. Therefore, RADIANCE combined these solving algorithms to optimize the payoff between rendering time and accuracy. The hybrid deterministic/stochastic (Monte Carlo) backward ray-tracing method in RADIANCE calculates the direct irradiance deterministically, while during the stochastic approach the indirect irradiance is calculated by a carefully-chosen subset of surface points used to estimate neighboring values generated from the random amount of distributed rays. However, additional solving algorithms are provided to reduce calculation time or optimize accuracy [52] for both the direct and indirect calculation and are customized by rendering parameters that are addressed via a command (i.e. *rtrace*, *rvu* or *rpict*) [49, 60]. Nevertheless, the '*correct settings*' of these rendering parameters vary depending on the characteristics of the model [60]. As starting point for the numerical models reported in Chapter 4 and Chapter 6, Table 1 is provided to give an overview of the main rendering parameters and recommended setting. Note that, for a rapid view of a scene (via the *rvu* command), lower rendering settings are recommended. Also, the maximum settings need to be avoided, as these settings cause extremely long calculation times and the parameters $-dr$ and $-dp$ should only be considered when perfect specular material types are included in the model. An in-depth explanation about the applied rendering parameters and solving algorithms can be found in Appendix 1. Consequently, an overview of all rendering parameters can be found in [52] or can be requested in the program by typing *-defaults* behind a command in the command line.

Table 1: The main rendering parameters for the (in-)direct calculation of a scene [49, 61] with the default, maximum and and recommended settings and their effect on the calculation time [51, 62].

Name	Rendering parameter	Settings			Effect on simulation time (t)
		Default	Maximum	Recommended	
Direct Relay	$-\boldsymbol{dr}$ $[N]$	2	6	2	$N \propto t$, dependant on the scene
Direct Pre-sampling	$-\boldsymbol{dp}$ $[res]$	512	0 (off)	1024	None
Ambient Bounces	$-\boldsymbol{ab}$ $[N]$	0	8	4 or 5	$N \propto t$
Ambient Resolution	$-\boldsymbol{ar}$ $[res]$	256	∞	128	$res \propto 2t$
Ambient Divisions	$-\boldsymbol{ad}$ $[N]$	1024	4096	512	$N \propto t$
Ambient Accuracy	$-\boldsymbol{aa}$ $[acc]$	0.1	0	0.15	$acc \propto 1/t$
Ambient Super-sample	$-\boldsymbol{as}$ $[N]$	512	1012	256	Depends on $-\boldsymbol{ad}$

2.4.3. Errors in radiance modeling

Similar to CFD modeling [63], during radiance modeling several types of errors can emerge, such as physical modeling errors, stochastic uncertainty errors, spectral errors and sensitivity errors. In addition, RADIANCE always calculates up to 5 digits, which can cause rounding-off errors. The most noticeable errors, however, emerges due to physical modeling errors that are related to incorrect formulation of surface material or intended simplification of a material or geometry. Furthermore, stochastic uncertainty errors emerge in the model as results of the indirect calculation, as recalculation of a model will yield slightly different results. In addition, spectral errors, which also can be considered as physical modeling errors, are defined by the wavelength range for which the rays are traced.

For each wavelength, materials can have different optical properties. However, to simplify a radiance model, identical optical properties for several or more wavelengths are adopted. This simplification is required, but the magnitude of the spectral error depends on the scene and applied materials. For instance, [64] demonstrated that the spectral modeling error in the standard RADIANCE RGB model makes default RADIANCE simulations less accurate than a spectral rendering.

Finally, there are the sensitivity errors which affect the results and are caused by incorrect settings of rendering parameters. These rendering parameters need to be addressed before executing a rendering/calculation command since they define the simulation accuracy. Normally, sensitivity errors decrease by changing the rendering parameters to a higher accuracy setting. For the most scenes, the *ambient bounce* ($-ab\,[N]$) will be the main influential rendering parameter for the sensitivity error. Therefore, verification for the *ambient bounce* rendering parameter is mandatory. Verification can be performed by running several simulations, while using different values for a rendering parameter through which several sampling points (using the *rtrace* command) in the model are calculated. While a parameter-independent solution is not computable due to the stochastic characteristics of the solving algorithm, these simulation runs can provide a lower parameter-dependent solution within the limits of the stochastic uncertainty error.

In this thesis, the stochastic uncertainty error is estimated for E_X [W m^{-2}] in any sampling point X for n simulations by applying statistics [65]:

$$\bar{E}_X = \frac{\sum_{i=1}^{n} E_{X\_i}}{n}, i = \{1,2,\dots,n\} \tag{2-30}$$

Where $\bar{E}_X$ [Wm^{-2}] is the average calculated irradiance value in point X obtained from all n simulations. In turn, the standard deviation of n is calculated by [65]:

$$sd(E_X) = \sqrt{\sum_{i=1}^{n} E_{X_i} \cdot \left(\frac{1}{n}\right)^2}, i = \{1,2,\dots,n\} \tag{2-31}$$

Where $sd(E_{sX})$ [Wm^{-2}] is the standard deviation of the irradiance value in point X from all n simulations. Now, given a 95% certainty interval, the range of the actual irradiance value in point X ($\bar{E}_{aX}$ [W m^{-2}]), assuming a normal distribution, is calculated according to *the central limit theorem* [65]:

$$\bar{E}_{aX} = \bar{E}_X \pm 1.833 \cdot \frac{sd(E_X)}{\sqrt{n}} \tag{2-32}$$

Alternatively, certain rendering parameters can be increased to decrease the stochastic uncertainty error (e.g. raising $-ar, -ad, -aa$ or $-as$). Convergence to a parameter-independent solution is not computable (e.g. typically calculated during CFD modeling [63]), since there is always a stochastic uncertainty involved. Nonetheless, while performing a validation analysis of a rendering parameter a criterion can be defined. For example, in this report, the *ambient bounce* parameter is defined by:

$$\text{If } \bar{E}_{X;\,ab_N+1} - \bar{E}_{X;\,ab_N} \leq \frac{1.833}{\sqrt{n}}\left(sd\left(E_{X;\,ab_N+1}\right) + sd(E_{X;\,ab_N})\right), \quad \text{then } N+1 \text{ is sufficient.} \tag{2-33}$$

Where N is the value given to the *ambient bounce* rendering parameter for simulation N. In the following section, an approach for spectral rendering with RADIANCE and sensitivity of the human eye is explained. In the next chapters, these methods will be used.

2.5. Spectral rendering and eye sensitivity

2.5.1. Spectral rendering in RADIANCE and the photometric system

Originally, RADIANCE was developed as a lighting modeling tool to analyze and visualize lighting design. Architects and engineers employ RADIANCE to predict the illumination, visual quality and the appearance of designed spaces, while researchers evaluate new lighting and day-lighting solutions [66]. For these purposes, the results are frequently expressed in photometric units, while, during processing, all parameters in the radiance equation are calculated by using the radiometric system. Therefore, after processing, the radiometric units need to be converted to the photometric units.

Generally, the photometric system describes the average spectral sensitivity of human visual perception for radiation (brightness). The human eye is perceives light with several different receptors which are located on the retina in the eye and can be classified into ganglion cells (circadian receptors), rods (scotopic receptors) and cones (photopic receptors). Normally, under normal luminance levels (> 1 cd m^{-2}), mainly the cones are active [67]. The conversion function which correlates the photometric and radiometric units is derived from the sensitivity of the receptors, which is estimated with a Brightness Luminous-efficiency Function (BLF) [67]. In RADIANCE, a BLF is incorporated into the RADIANCE RBG model.

Together with the assessment of lighting design, recent developments within the RADIANCE community led to spectral rendering efforts with RADIANCE for new purposes [52]. As was mentioned earlier, [53] showed that spectral rendering with RADIANCE can actually be more accurate than rendering with the default method. As was briefly mentioned in Section 2.3, RADIANCE solves the radiance equation for the RBG values separately. While the RGB values for individual points (using *rtrace*) are calculated separately, when rendering a picture, the RGB values are converted to a single value using the RADIANCE RGB model, since RADIANCE was originally developed for the assessment of lighting design. Basically, during the rendering of a picture, the RGB values are summed up, according to [64]:

$$L_i(L_R, L_G, L_B) = L_R \cdot 0.265 + L_G \cdot 0.670 + L_B \cdot 0.0648 \tag{2-34}$$

Then, L_i can be manually multiplied with a conversion factor (= 179 lmW^{-1} [52]) to complete the weighting for the eye sensitivity. However, in this thesis a spectral rendering approach is applied, the RADIANCE RGB model is not applied. In fact, the RADIANCE RGB model differs slightly from the more commonly accepted weighting functions [52].

Generally, the use of RADIANCE RGB model can be prevented with several techniques in order to render spectrally. First of all, if the correct reflection / emission models are selected for the materials in a scene, the three RGB values could represent a specific wavelength band, as these values are calculated separately when using the command *rtrace*. As a result, the radiance model can be processed for three different specific wavelength bands at once. However, during rendering, either a gray scale (monochromatic scale) or N-algorithm method [53] should be adapted in order to generate a correct data.

During the modeling studies in this report, a grey scale is assumed, implying that the optical properties for all included wavelengths are identical. Therefore, both the calculation of points and pictures can be processed, without the intervention of additional operations. However, in Chapter 6, the irradiance quantities will be defined based on the amount of required illumination of the room. Since the RADIANCE RGB model is not used, a new conversion factor is necessary to convert the obtained radiometric units to photometric units and vice versa. Furthermore, the required illuminance values need to be linked with general indoor activities, which are explained in the next section.

2.5.2. The luminous-efficiency function for the human eye and general indoor activities

In general, for the conversion between the radiometric units and photometric units is considered for the spectral range of light, a general definition defined as:

$$\Phi_p = K_p \int_{380nm}^{780nm} \Phi_r(\lambda) V_{prf}(\lambda) d\lambda \tag{2-35}$$

Where Φ_p [lm] luminous flux; K_p [683 lmW^{-1}] a constant for photopic region (normalized for the wavelength to which the eye is most sensitive; 555 nm); Φ_r [W] is the radiant flux; V_{prf} [-] is the BLF for the photopic response function of the human eye. Note that the BLF can differ per age [68]. Furthermore, multiple photopic BLF can be found in literature. For normal lighting intensities, the photopic BLF is the best approximation for the sensitivity of the human eye. Conversely, at lower light levels, the scotopic BLF should be applied.

Additionally, the luminous efficacy of the light sources needs to be taken into account, because during modeling the gray-scale approach is adapted. In general, for the spectral range of light, the luminous efficacy (ϑ[%]) is defined by:

$$\vartheta = 100 \cdot \frac{\Phi_p}{\Phi_r} = 100 \cdot \frac{\int_{380nm}^{780nm} \Phi_r(\lambda) V_{prf}(\lambda) d\lambda}{\int_{380nm}^{780nm} \Phi_r(\lambda) d\lambda} \tag{2-36}$$

Where Φ_r[W] is the radiant flux. Equation (2-36) implies that, an ideal deal monochromatic source of 555 nm would have a ϑ of 1. Note that for visibility, also contrast is considered for the assessment of perceived light from a light source by the human eye.

The required illuminance value in a room depends on the indoor activity of that room. In turn, the amount of available illuminance determines the amount of irradiance that initiates photocatalytic reactions on the surface of the photocatalyst. In Table 2, the recommended illuminance values for various activities are reported according to the Illuminating Engineering Society (IES) [69]. These values can provide an estimation of the light quantity needed within a room for certain indoor activity. These relations will be studied in Chapter 6, during the third modeling study. However, before the third modeling study is performed, the second modeling study will be presented for which additional theory is explained in the following section.

Table 2: IES Illuminance Categories and Values - For Generic Indoor Activities [69].

Activity	Category	Illuminance [lux]
Public spaces with dark surroundings	A	20-30-50
Simple orientation for short temporary visits	B	50-75-100
Working spaces where visual tasks are only occasionally performed	C	100-150-200
Performance of visual tasks of high contrast or large size	D	200-300-500
Performance of visual tasks of medium contrast or small size	E	500-750-1000
Performance of visual tasks of low contrast or very small size	F	1000-1500-2000
Performance of visual tasks of low contrast or very small size over a prolonged period	G	2000-3000-5000
Performance of very prolonged and exacting visual tasks	H	5000-7500-10000
Performance of very special visual tasks of extremely low contrast	I	10000-15000-20000

2.6. Ideal reactor characterization

During the second modeling study in Chapter 5, an ideally mixed room model is developed based on the principles of an ideal plug flow reactor concept which was applied in [1] to derive the rate constants from the kinetic experiments [3]. The understanding of a reactor system is required to determine both the reaction mechanisms and kinetics. Therefore, reactors are often built to approach ideal reactors. In these ideal reactors, such as the ideal plug flow reactor or an ideal mixed reactor, ideal flows are assumed to be able to fully describe the performance by a set of mass or mole balance equations. Likewise, similar equations can be applied to describe the ideally mixed room. In this section, the concepts behind the ideal flows within these systems are discussed.

In previous experimental studies on NO_x degradation [3, 70, 71], similar reactor setups were employed, based on ISO 22197-1 [72]. Since the reactor setup was not controlled by interfacial mass transport [71] (usually, described by the Damköhler number [73]), a constant concentration of a pollutant was adapted over the height and depth of the reactor system. As a result, the behavior of the reactor could be descripted by the conceptual model of an ideal plug flow reactor, as illustrated in Figure 6a. As is clarified in Figure 6a, for any arbitrary compound *p* during a steady state in the ideal plug flow reactor, a mole balance can be defined according to the following definition [1, 70, 71]:

$$u_x \frac{dC_p}{dx} = -a_v r_p D_{TiO2} \tag{2-37}$$

Where u_x [m s^{-1}] is the velocity magnitude in the x-direction; $\frac{dC_p}{dx}$ [mol $m^{-3}m^{-1}$] is the change of concentration for compound *p* over distance x; a_v [m^{-1}] is the active surface area per reactor volume (A_c/V); r_p [mol $m^{-2}s^{-1}$] is the surface reaction rate of compound *p*; and D_{TiO2} [-] is the photocatalyst dosage. Consecutively, a forward discretization approach (the Euler approach) was applied in [1, 70, 71] to solve equation (2-37), as illustrated in Figure 6b. Generally, for the forward discretization approach, the mole balance in segment *j* is defined as:

$$u_x \frac{C_{p;i+1} - C_{p;i}}{x_{i+1} - x_i} = -a_{v;j} r_{p;j} D_{TiO2} \tag{2-38}$$

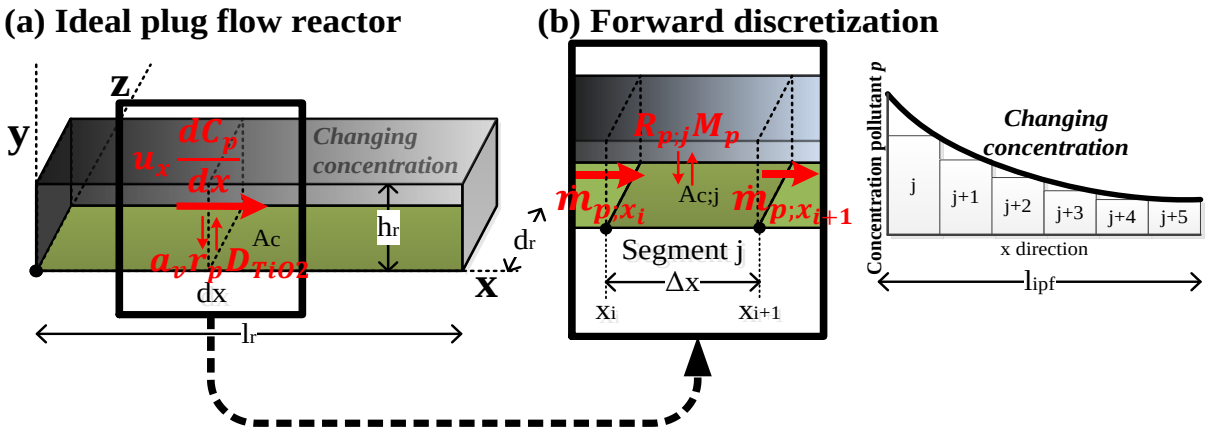

Figure 6: (a) The ideal plug flow model concept. The black printed variables are; A_c [m^{-2}], the catalyst surface area; and h_r, l_r and d_r [m], the special dimensions of the model. The red printed variables are; u_x [m s^{-1}] the velocity magnitude in the x-direction; dC_p/dx [mol $m^{-3}m^{-1}$] the change of compound *p* concentration over x; $\dot{m}_{p;x_i}$ and $\dot{m}_{p;x_{i+1}}$ [kg s^{-1}] the mass flow at respectively x and x+1; $R_{p;j}$ [mol $m^{-3}s^{-1}$] the apparent volume reaction rate in segment *j* for compound *p*; and M_p [kg mol^{-1}] the molar mass of compound *p*. (b) The concept of forward discretization of the ideal plug flow model for m=6.

The forward discretization approach implies that the ideal plug flow in the reactor setup can be approximated by a series of connected ideal mixed flow model. This is demonstrated by rewriting equation (2-38). To start with, $a_{v;j}$ is further defined as:

$$a_{v;j} = A_{c;j}/V_j \tag{2-39}$$

Where V_j [m^3] is the volume of segment j. Furthermore, u_x is expressed as:

$$u_x = \Delta x/\tau_j \tag{2-40}$$

Where τ_j [s] is the residence time in segment j, which is in turn defined as:

$$\tau_j = \frac{V_j}{Q}, Q = Q_j \tag{2-41}$$

Where Q [m^3s^{-1}] is the volumetric flow rate through the system which is equal for all elements. Now, given that $x_{i+1} - x_i = \Delta x$, equations (2-39)-(2-41) are substituted into equation (2-38), yields:

$$Q\frac{\Delta x}{V_j}\frac{C_{p;i+1} - C_{p;i}}{\Delta x} = -\frac{A_{c;j}}{V_j} r_{p;j} D_{TiO2} \tag{2-42}$$

Which is rewritten, by canceling out Δx and V_j, giving the following definition:

$$Q\left(C_{p;i+1} - C_{p;i}\right) = -A_{c;j} r_{p;j} D_{TiO2} \tag{2-43}$$

That is analogous to the expression for an ideal mixed flow [74]. Alternatively, in line with the terms from Figure 6b, equation (2-43) can be rewritten to a mass balance expression which is formulated by:

$$\dot{m}_{p;x} - \dot{m}_{x+1} = -A_{c;j} r_{p;j} D_{TiO2} M = -R_{p;j} M = -\dot{m}_{r;p;j} \tag{2-44}$$

Where $\dot{m}_{p;x_i}$ and $\dot{m}_{p;x_{i+1}}$ [kg s^{-1}] are the mass flow of pollutant *p* at respectively position x and x+1; $R_{p;j}$ [mol $m^{-3}s^{-1}$] is the apparent volume reaction rate of pollutant *p* in segment *j*; M_p [kg mol^{-1}] is the molar mass of pollutant *p*; and $\dot{m}_{r;p;j}$ is the mass flow created by the photocatalyst of pollutant *p* in segment *j*. Lastly, $\dot{m}_{p;x}$ and $\dot{m}_{p;x+1}$ can be further defined by:

$$\dot{m}_{p;x} = Q\gamma_{p;x}\rho_{air} \qquad \dot{m}_{p;x+1} = Q\gamma_{p;x+1}\rho_{air} \tag{2-45}$$

Where $\gamma_{p;x}$ and $\gamma_{p;x+1}$ [-] is the mass fraction of pollutant *p* at respectively position x and x+1; Q [m^3s^{-1}] is the volumetric flow rate through the system; and ρ_{air} [kg m^{-3}] is the total density of the carrier gas, which is assumed to be 1.204 kg m^{-3}, for an air temperature at 293.15 K and a pressure of 101325 Pa. The expressions in equation (2-44) and equation (2-45) are applied later in Chapter 5, during the second modeling study, as initial principles from which the ideally mixed room model is built. Additionally, in analogous with the mass flow expression in equation (2-44), a new approach for the implementation of the kinetic model in a CFD model is derived in the next section. This new approach will be later employed in Chapter 6, during CFD modeling.

2.7. New approach for the kinetic model implementation into CFD

A CFD model of the reactor was developed in [2] validated with experimental data. However, the implementation method of [2] may cause a potential source of error for future modeling work, since the cells height in which the kinetic model was applied were not incorporated. Therefore, a new implementation method is suggested, based on the volume-based implementation method of [2].

The volume-based implementation method of [2] was applied by creating an User Defined Function (UDF) to define the reaction surface rate as source term (S_s [kg m^{-3} s^{-1}]) in the species transport equation used in FLUENT. The species transport equation conserves the mass of any used compound in the system modeled in FLUENT. The general terms in a species transport equation may be expressed for any arbitrary compound *P*, per cell (node), by the following definition [75]:

$$\rho \frac{dY_p}{dt} = -\nabla \cdot (\rho Y_p \vec{u}) - \nabla \cdot \left(D_{p,air} \rho \nabla Y_p\right) + S_s \tag{2-46}$$

Where Y_p [-] is the mass fraction of compound p; $D_{p,air}$ [m^2 s^{-1}] is the diffusion coefficient of pollutant p in air; and S_s [kg m^{-3} s^{-1}] is a source term. As demonstrated in Figure 7, the source term in the adjacent cells layer near a photocatalyst-coated wall was defined by $f(\dots)$, while the source term remained zero for the remaining cells.

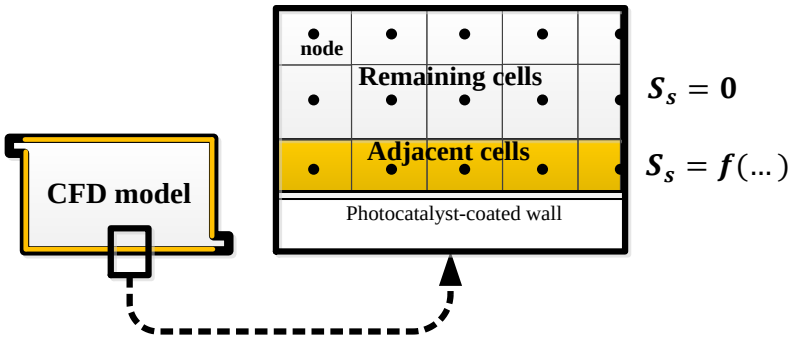

Figure 7: The volume-based implementation method for a NO_x kinetic model using the source term (S [kg m^{-3} s^{-1}]) of [2].

Consequently, $f(\dots)$ was further defined by [2], as a result the source term for this adjacent cell layer is defined as:

$$S_s = a_v r_p M_p D_{TiO2} \tag{2-47}$$

Where r_p [mol m^{-2}s^{-1}] and M_p [kg mol^{-1}] are respectively the surface reaction rate and molar mass of compound *p*. In turn, a_v [m^{-1}] is the active surface area per reactor volume (A_c/V) which is a fixed value of 0.003 m [2]. Hence, the cell height was not included.

Nonetheless, in [2], small variations in the cell height demonstrated that the UDF definition, in equation (2-47), affected the mass flow only by a small amount during the reactor modeling. Even so, the cell height did influence the results. Furthermore, bigger cell dimensions were applied in the second part of [2], during the analysis of the room model. As a result, the results of the room model in [2] are unreliable and would hinder further implementation of the kinetic model in future CFD modeling. Therefore, a new approach is suggested to incorporate the cell height.

The new approach is derived from two observed systems, as illustrated in Figure 8. While in system A (Figure 8a), the actual surface reaction on the photocatalyst-coated surface is considered, system B (Figure 8b) considers a cell volume representing the actual surface reaction on the photocatalyst-coated surface. In fact, in the volume-based implementation method, system A is substituted by system B by stating the following condition:

$$\dot{m}_{r;p} = \dot{m}_{r;p;A} = \dot{m}_{r;p;B} \tag{2-48}$$

Where $\dot{m}_{r;p;A}$ and $\dot{m}_{r;p;B}$ [kg s^{-1}] are the total mass flows due to chemical reactions in respectively system A and B.

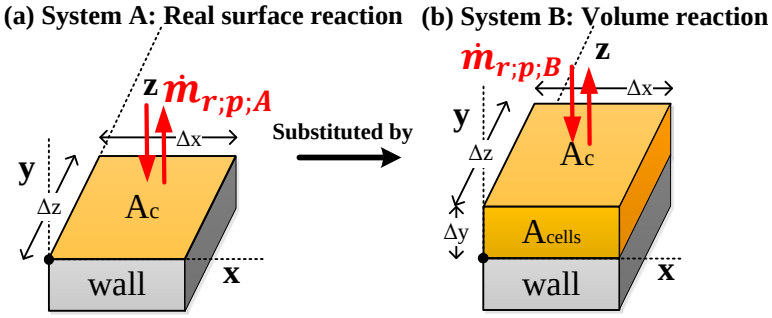

Figure 8: (a) The real surface reaction which is (b) substituted by a volume-based reaction for compound *p* when implemented in a CDF model.

Now, equation (2-48) is extended by stating $\dot{m}_{r;p;A} = r_p A_{c;A} M_p$ and $\dot{m}_{r;p;B} = V_B r_{p;B} M_p$, so that:

$$\dot{m}_{r;p} = r_p A_c M_p \ = V_B r_{p;B} M_p = M r_{p;B} A_c \Delta y \tag{2-49}$$

Where A_c [m^2] is the photocatalyst-coated area; and V_B [m^3] and $r_{p;B}$ are correspondingly the volume and the volume reaction rate of system B. Evidently:

$$A_c = \Delta x \Delta z \tag{2-50}$$

By canceling out A_c and M_p in equation (2-49), and with rearrangement, the relation between the reaction rates in both systems is obtained:

$$r_{p;B} = r_p / \Delta y \tag{2-51}$$

Subsequently, the source term in the field equation, expressed by equation (2-46), is further specified by:

$$\dot{m}_{r;p} / \Delta z A_{cells} = S_s \tag{2-52}$$

And A_{cells} [m^2], the area of the cells is defined by:

$$A_{cells} = \Delta x \Delta y \tag{2-53}$$

So that equation (2-53), equation (2-51), and the last term in equation (2-50) and equation (2-49) can be substituted into equation (2-52), and canceling out Δx, Δy and Δz, to provide:

$$\frac{M_p r_p}{\Delta y} = S_s \tag{2-54}$$

Equation (2-54) replaces the additional term $f(\dots)$, so that the source term in the adjacent layer of cells is redefined. In Section 6.3.4, the new implementation method is verified by simulation. However, preceding Chapter 6, the optical experiments are discussed in the following section.

Chapter 3. Optical experiments

3.1. Overview

In this chapter, the optical properties required for the modeling studies are measured. Three experiments were executed to generate input for the first and third modeling study. Furthermore, experimental data for validation of the reactor setup model and the derivation of a conversion factor for definition of the ratio between the photometric and radiometric data was required. An overview of the reactor setup is found below in Figure 9. Both the main components and materials are presented. As shown by the back arrow, during experiments the luminaire is placed on the reactor casing.

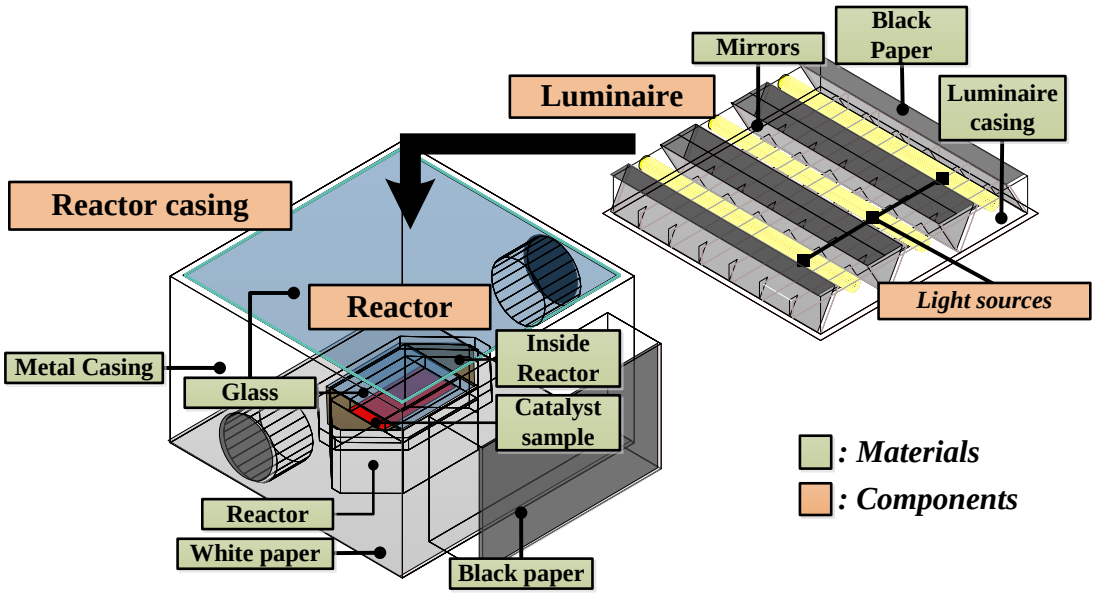

Figure 9: The reactor setup: materials and components. For experiments, the luminaire is placed on the reactor casing.

During the first experiment, the spectral transmission in the range of 300-750 nm of the glass cover of the reactor in the reactor setup was obtained. In addition, the spectral transmission was successfully compared with an analytical calculation, so that the refraction index (applied in the analytical calculation) could be applied in the first and third modeling study for the description of the optical characteristics of borosilicate glass. The spectral transmission was used for the modeling of the glass plate of the reactor in the first modeling study.

Secondly, a series of spectral reflection measurements were performed to obtain the reflection coefficient and specular component of the materials in the reactor setup and the photocatalytically active sample used in [3] for the range of 400-570 nm. Both the reflection coefficient and specular component were necessary for the radiance simulations in both the first and last modeling study.

In the third experiment, the emission spectrum between the 300-750 nm of the light sources in the reactor setup was acquired, for the development of a conversion factor between the photometric and radiometric units, needed in the third modeling study. Lastly, the irradiance on the glass plate in the reactor setup was measured to validate the first modeling study. In the next sections, the method and results of the experiment are reported.

3.2. Transmission

3.2.1. Methodology

Since the refraction index of the glass cover was unknown, a transmittance measurement of the glass cover is performed and compared with an analytical calculation to verify the selected refraction index. Subsequently, the refraction index (n) of SCHOTT Borofloat® 33 glass, a broadly applied borosilicate glass type, was selected; which is 1.4768 for 480 nm [76]. The refraction index of borosilicate glass will be used to model the glass cover in the reactor setup during the radiance modeling.

The analytical calculation of the transmittance of a glass cover was performed according to the schematic model in Figure 10.

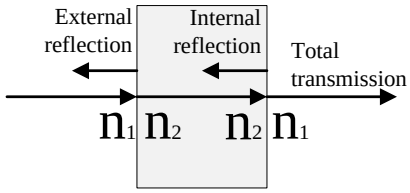

Figure 10: The schematic model of the transmittance calculation of glass [77].

According to the schematic model shown in Figure 10, by applying Fresnel's equation at normal incidence ($\theta_i = 0$) [78], the transmittance of the glass (τ_{glass} [-]) is obtained by:

$$\tau_{glass} = \left(1 - \left(\frac{n_2 - n_1}{n_2 + n_1}\right)^2\right) \cdot \left(1 - \left(\frac{n_1 - n_2}{n_1 + n_2}\right)^2\right) \quad (3\text{-}1)$$

Where n_1 and n_2 [-] are the refraction index of air and SCHOTT Borofloat® 33 respectively.

Consecutively, the transmission experiment is performed applying the setup, as shown in Figure 11. All equipment was obtained from Ocean Optics, with the exception of the filter and the external computer.

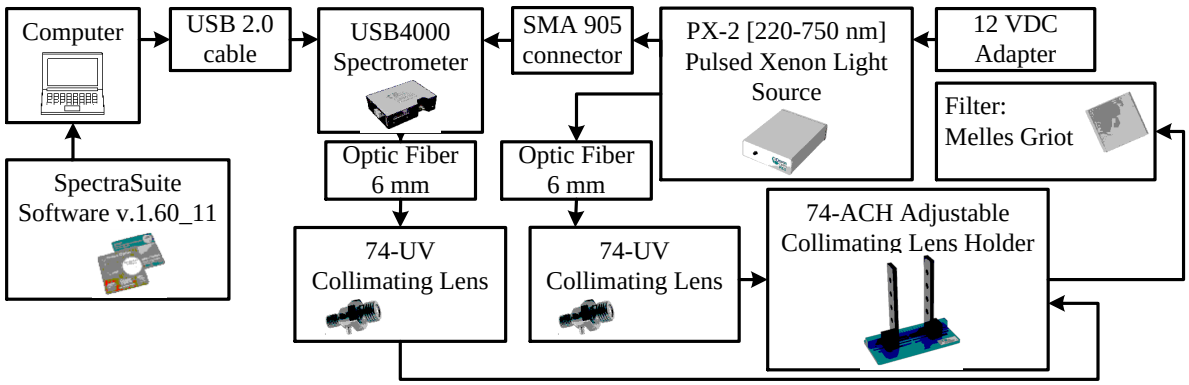

Figure 11: Setup for the basic transmittance measurement.

During the experiment, the glass cover (8 mm thick) was fixed by supportive perspex plates in the 74-ACH collimating lens holder perpendicular to the two collimating lenses, with a total distance of 1 cm on both sites of the sample. The two collimating lenses corrected the radiation in the optic fiber cables to a distribution of only 2% wide [79]. Preliminary measurements did not yield any valid results, since the USB4000 spectrometer received an excessive amount of radiant flux from the PX-2 xenon light source. Therefore, a filter was fitted between the two collimating lenses, to lower the amount of radiant flux. The filter was fixated against the supportive perspex plate between the collimating lenses on the side of the light source using tape. Both the dark ($\tau = 0$) and light ($\tau = 1$) calibration were conducted with the filter to correct for the influence of the filter on the transmittance. The xenon light source is turned off and on, respectively during the dark and light calibration. During a measurement, 30 scans within 3 seconds were taken giving an interval of 100 ms between the scans and averaged for the measurement. The xenon light source and the spectrometer are attached by the SMA 905 connector allowing the pulses of the light source to be adjusted to the scanning time of the spectroscope. The spectrometer registered the spectrum over an interval of 0.26 nm between 220-750 nm. Furthermore, the experiment was performed in a dark condition, by turning off the laboratory lights. No windows were present in the laboratory. The specifications of the spectrometer and the xenon light source are presented in Table 3.

Table 3: Technical data of the USB4000 spectrometer [80] and the PX-2 xenon light source [81].

	USB4000 spectrometer	**PX-2 xenon light source**
Optical resolution	Depends on the grating and the size of the entrance aperture	-
Integration time	3.8 ms to 10 s	-
Dimensions / Weight	148.6x104.8x45.1 mm / 570 g	153.5x104.9x40.9 mm / 390 g
Range	200-1100 nm	220-750 nm
Lifetime	-	10^9 pulses

3.2.2. **Results**

First, the transmittance was analytically computed, assuming that the index of refraction of air (n_1) and the glass cover (n_2) are respectively 1 and 1.4768 (for 480 nm) [76], yielding a τ_{glass} of 0.9273. Secondly, the transmittance was measured. Figure 12 illustrates the measured values of the spectral transmittance of the glass cover and the required filter. An average transmittance of 0.9276 between 400-570 nm was obtained.

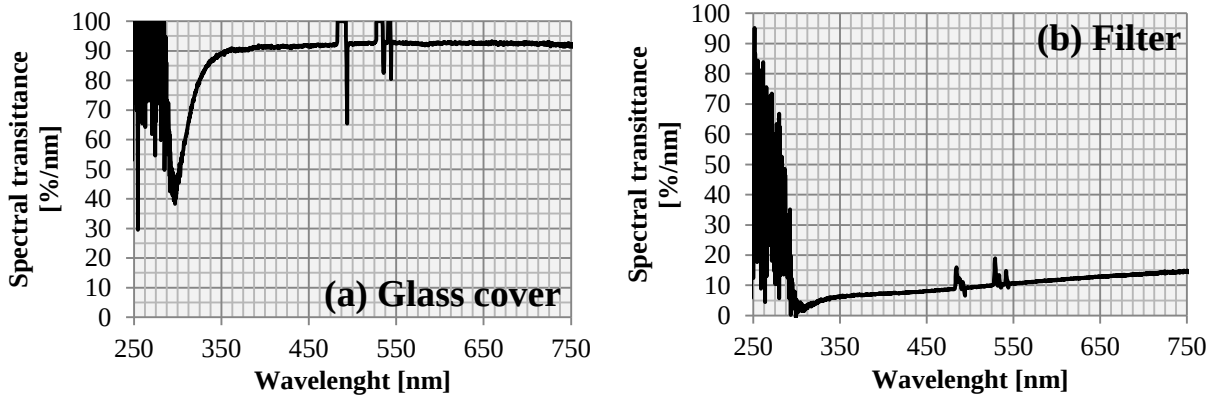

Figure 12: The measured spectral transmittance of (a) the glass cover and (b) the filter.

3.2.3. **Discussion**

A filter was applied to lower radiant flux burden on the spectroscope, even though the filter caused a incorrect data output between 480-495 nm, 525-545 nm and below 300 nm. Therefore, the values between 480-495 nm and 525-545 nm were assumed to be parallel to adjacent values. Alternatively, according to Ocean Optics, the radiant flux burden on the spectroscope could also be lowered by applying an optic fiber cable of 0.5 mm rather than an optic fiber cable of 6 mm, which was applied. Still, other filters may also provide a viable alternative, as the calibrations adjust the measurement for any applied filter.

Furthermore, the current setup can be used to determine the transmittance of other samples with specular reflection, however, can be improved. In the current setup, measurement errors may arise by ignoring absorption. While it was assumed that the adsorption of the glass cover between 350-750 nm is minimal, for other glass samples or wavelength ranges additional absorption can occur. Therefore, an absorption measurement should be included in order to make the setup more accurate.

3.2.4. **Conclusion**

The measurement of the transmittance yielded a averaged value of 0.9276 for 400-570 nm, while the analyical calculation produced a value of 0.9273. Since the relative difference is 0.032%, the refraction index (n) of SCHOTT Borofloat® 33 glass can be used for modeling of the glass cover without producing any significant error.

3.3. **Reflection**

3.3.1. **Methodology**

Both the spectral reflection coefficients and specular components are needed for the definition of the materials during radiance modeling. Therefore, reflection measurements are performed with the (sphere-based) CM-2600d spectrophotometer. Details of the measurement principle of the CM-2600d spectrophotometer are given in Figure 13. The inside of the integrating sphere of the spectrophotometer has a (high) diffusive reflection coefficient (barium sulfate). Both source ① and ② are xenon light sources. During a single measurement, both the Specular Component Included (SCI) and Specular Component Excluded (SCE) are simultaneously obtained from two illumination samples within 1.5 seconds. First, the SCI is obtained for which the illumination of source ① and ② is needed (Figure 13a). During the second sampling, the illumination of source ① and ② is separately measured (Figure 13b).

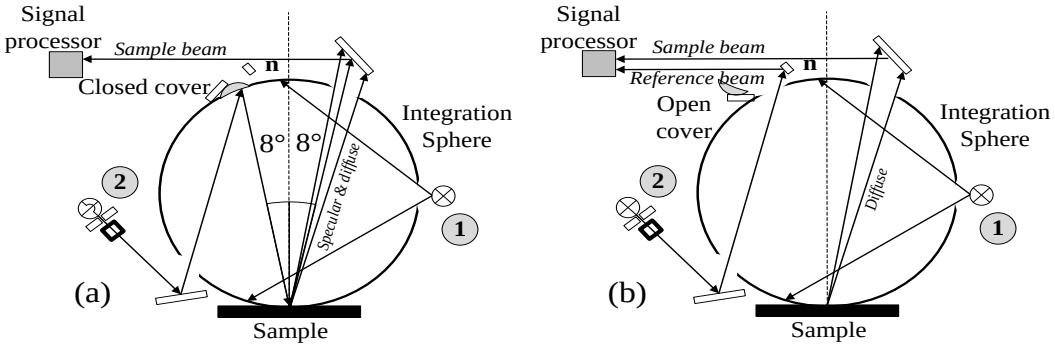

Figure 13: The measurement principle of the CM02600d Spectrophotometer [82]. First the SCI (a) is sampled and then the SCE (b) is sampled. ① and ② represent the two xenon light sources in the setup.

The numerical values of the specular component (S [-]) are obtained by combining and calculating the data obtained from both samplings. From the obtained SCI and SCE, a specular component is derived:

$$S = \frac{SCI - SCE}{SCI} \tag{3-2}$$

The specular component expresses the specular capability of a surface. For instance, a surface can be specular ($S = 1$), diffuse ($S = 0$) or somewhere in between. In turn, the reflection coefficient σ [%] is defined as:

$$\sigma = SCI \tag{3-3}$$

The requirements and setup of the reflection measurement are illustrated in Figure 14. The CM-2600d Spectrophotometer from Konica Minolta and the external computer with SpectraMagic Software v.3.6. were attached by an RS232C Cable. Before performing the experiments, the spectrophotometer is calibrated for a dark spectrum ($\sigma = 0\%$), created by empty space, and for a light spectrum ($\sigma = 100\%$) on the diffuse reflection standard, using the wizard included in the software. The spectrophotometer provided the reflectance with the specular component included (SCI) and specular component excluded (SCE) by scanning during two flashes of the xenon lamp an interval of 10 nm between 400-700 nm. The main specifications of the photospectrometer are included in Table 4.

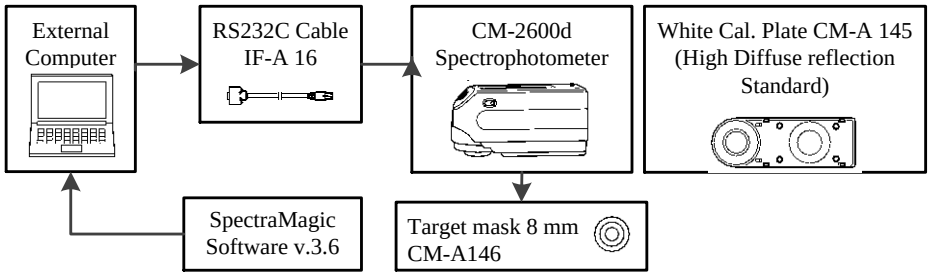

Figure 14: Basic setup of the reflection measurement [82].

Table 4: Main specifications of the CM-2600d according to [82].

Integrating sphere	**Ø 52 mm**
Measurement area	Ø 8 mm
Dimensions	96x193x69 mm (Height Length Width)
Range	360-740 nm (Xenon lamp)
Standard Deviation	0.1% (340-380 nm within 0.2%)

3.3.2. **Results**

In Figure 15, the calculated specular component (*S*) and spectral reflection coefficient per nm (10 nm interval) for the measured materials are illustrated. The average, minimum and maximum values for specular component (red) and reflection coefficient (black) were obtained from 10 different samples.

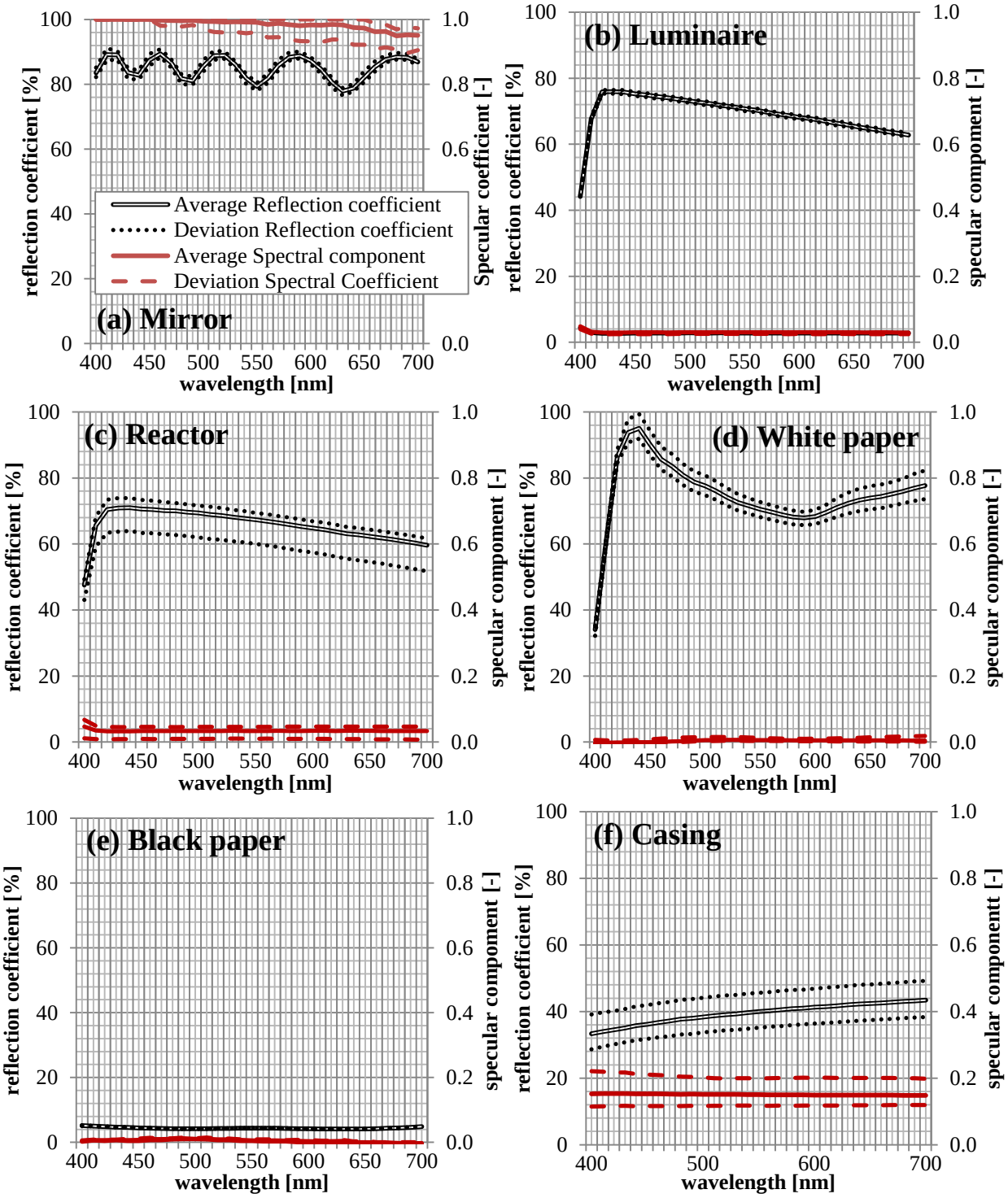

Figure 15: The calculated specular component and spectral reflection coefficient of the materials in the reactor setup. The continuous lines represent the average reflection coefficient (black) and spectral component (red). In turn, the dashed lines represent the minimum and maximum values found.

In turn, the photocatalytically active sample, used in [3], was measured and illustrated in Figure 16.

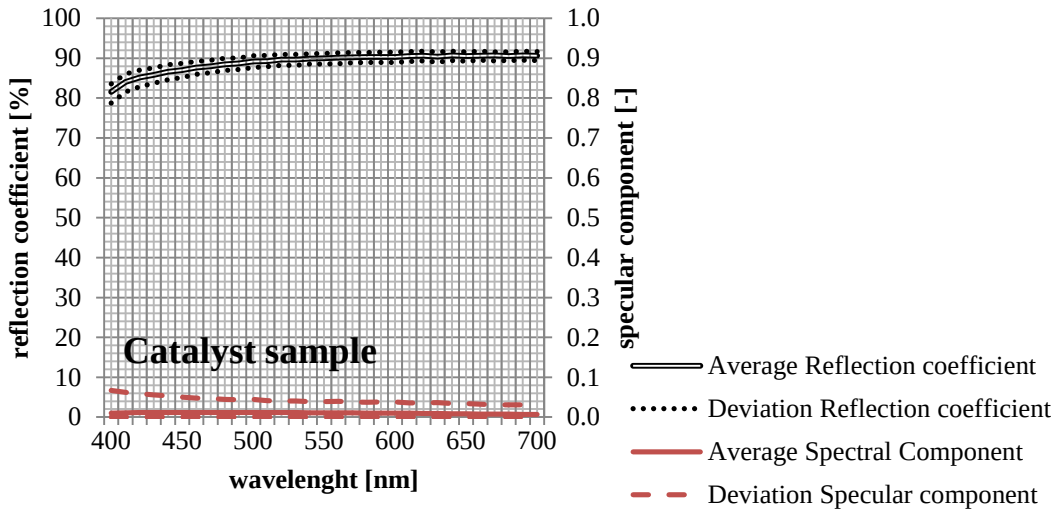

Figure 16: The calculated specular and spectral reflection coefficient of the photocatalytically active sample. The continuous lines represent the average reflection coefficient (black) and spectral component (red). In turn, the dashed/dotted lines represent the minimum and maximum values found.

3.3.3. Discussion & recommendations

According to [52], the applied method is adequate for obtaining the reflection behavior of common materials. However, when a gonioreflectrometer is used, the BRDF of any surface can be obtained [83]. Nonetheless, a gonioreflectrometer measurement may yield around 12000 samplings per material, that sequentially provide to 100 million BSDF data-points, dependent on the function (i.e. BRDF or BRTDF) [84]. In principle, experimental data can be imported via data tables as input in RADIANCE via data files explained in [84]. Furthermore, Ocean Optics supplies integrating spheres which may be combined with the Spectrometer (USB4000) [79], allowing measurement of the total reflectance of a surface within a broader range. However, some surfaces may cause fluorescence effects when exposed to UV. Optionally, the CM-2600d spectrophotometer can be used to correct it.

3.4. Irradiance

3.4.1. Methodology

The reactor setup model in the first modeling study was validated by experimental data. At the start, the experimental data was obtained with the UV-VIS radiometer RM-12, by using the VISBG sensor [85]. The irradiance was measured in the reactor setup within the target range of 400-570 nm, deduced from [3], over 21 sampling points, using a grid, illustrated in Figure 17. During the measurement, the output of the light sources was maximized and the irradiance measured threefold per sampling point giving 72 output values. The technical data of the radiometer and VISBG sensor is reported in Table 5.

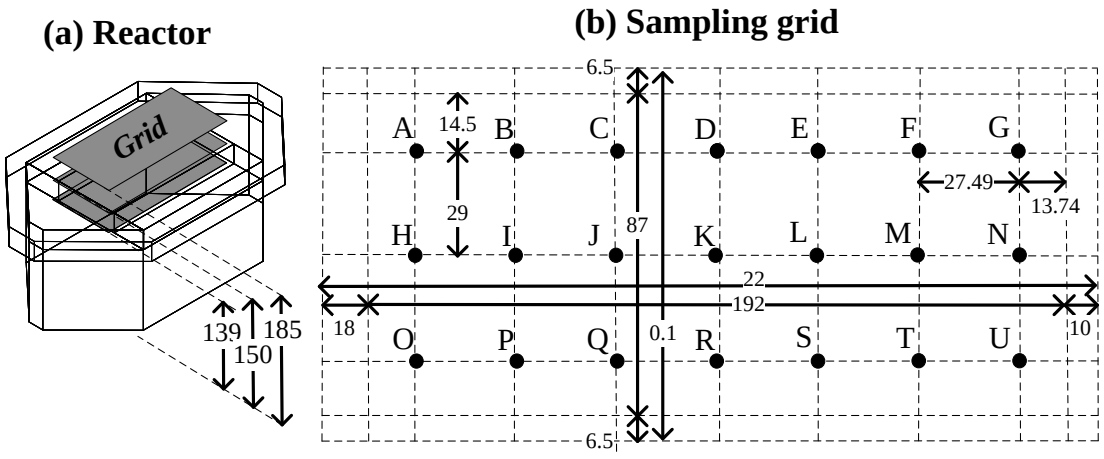

Figure 17: In the middle of reactor setup (a) direct above the reactor (b), the sampling grid (c) is located on a height of 185mm (dimensions are given in mm).

Table 5: Technical data of the RM-12 Radiometer and VISBG sensor [85].

Dimensions radiometer	**160 x 85 x 35 mm (length width height)**
Dimensions sensor	Ø 40 mm, h 35 mm (Diameter height)
Range sensor	400-570 nm, 0-200 $mWcm^{-2}$
Resolution sensor	0.01 $mWcm^{-2}$

3.4.2. Results

The average irradiance and deviation are illustrated in Figure 18. A maximum deviation of 0.11 Wm^{-2} was found in the sampling point U. The irradiance values will be used to validate the radiance model in the first modeling study.

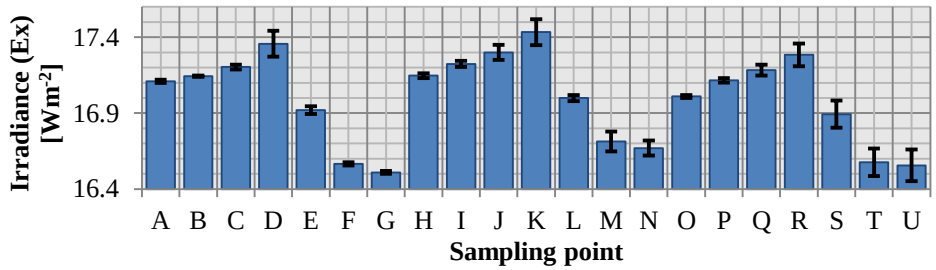

Figure 18: The average irradiance per sampling point (E_X) and deviation for 3 measurements using maximum output.

3.5. Emission

3.5.1. Methodology

The emission of the light sources was obtained using the setup as shown in Figure 19. Before the emissions of the light sources were measured, the setup is calibrated with a calibration lamp (HL-2000-CAL) on 12/8/11 between the 300-1050 nm [86]. The angle of incidence of the optic fiber (25°) is corrected with a cosine corrector, allowing an angle of incidence of 180 degrees (a hemisphere). The cosines corrector was detained on the light source surface in the middle of the bulb for the measurement. From each individual light source in the reactor setup, a single measurement was taken and averaged collectively to a single emission spectrum. During the measurement, the output of the light sources was maximized; the effect of lower output settings was not considered.

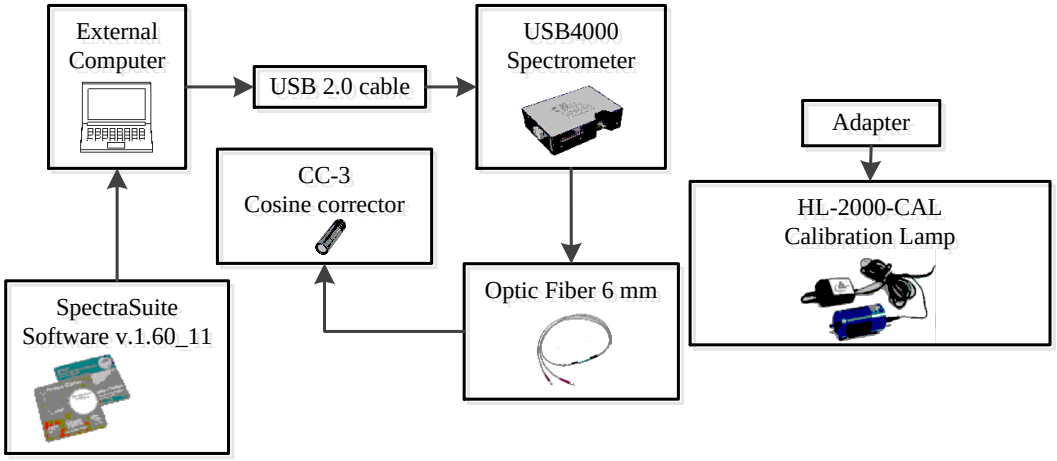

Figure 19: The setup of the spectral irradiance measurement.

3.5.2. Results

In Figure 20, the averaged spectral irradiance is illustrated. This data will be applied in Section 6.2.5 to calculate the conversion factor by normalizing the spectrum.

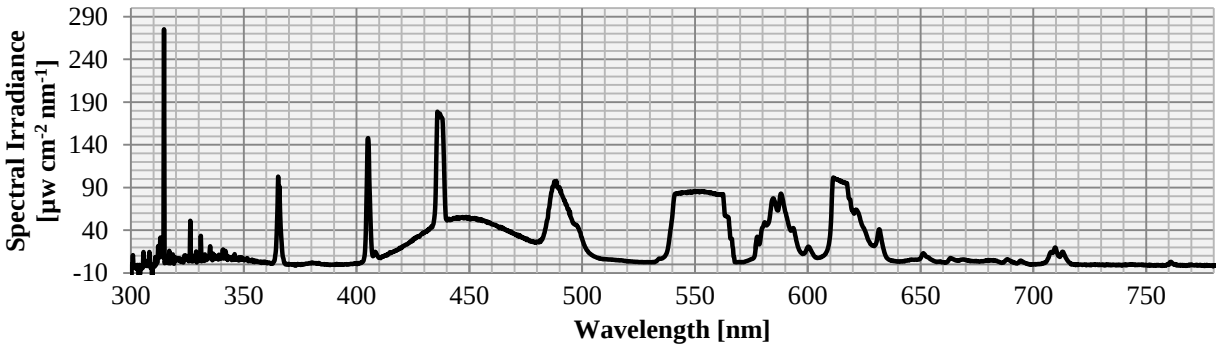

Figure 20: Average spectral irradiance of the light sources (PHILIPS Master TL-D 18 W/854) between 300-780 nm.

3.5.3. Recommendations

If the total emission energy is required, equation (2-29) should not be applied. In fact, the total radiant energy of the light sources can be measured by measuring the light source in an integrating sphere.

3.6. Concluding remarks

Within this chapter, various experiments for the built of the models in Chapter 4 and Chapter 6 were performed. In the following chapter, the obtained data from optical experiments from the transmission measurement in Section 3.2 and the reflection measurement in Section 3.3 are used to build the model of the reactor setup. Consequently, the irradiance data from Section 3.4 is used to validate the model. The emission data from Section 3.5 and the theory of Section 2.5.2 will be used in the last modeling study of Chapter 6 to develop the conversion factor. In addition, the reflection data on the photocatalytic sample is applied in Chapter 6 for the construction of the radiance model. Prior to the radiance model in Chapter 6, however, the radiance model of the reactor setup is presented in the following chapter.

Chapter 4. First modeling study: the reactor setup

4.1. Introduction

In the previous work [1, 2], during the development of the kinetic model of NO_x, the optical effects of the glass cover on the reactor were not take into account and a uniform irradiance distribution was assumed on the surface of the photocatalytically active sample. In this modeling study, a radiance model is constructed in order to provide insight in the previously made assumptions, therefore a more refined kinetic model for NO_x can be developed. A monochromatic radiance model is built with RADIANCE (v4.1) (available from [50]), installed in the emulator Oracle VM Virtual Box (v4.0.2) on Ubuntu OS (v.10.10). An extended overview of RADIANCE can be found elsewhere [51, 52].

4.2. Methodology

4.2.1. Geometry

The geometry of the reactor setup was categorized in the geometry files (**.rad*) of the radiance model by three main components, including the luminaire, casing and reactor, as indicated in Figure 21. The luminaire component is subdivided into a light source model and two mirror types. The input for the geometry files is found in Appendix 1. In contrast to CFD modeling, the geometry did not require meshing; as an alternative the calculation is defined by the rendering parameters (Section 2.4.2). The base dimensions of the luminaire are 0.59x0.59x0.085 m^3, while the casing has the dimensions of 0.65x0.65x0.4 m^3. In the overview of Figure 21, the main dimensions of the setup are reported, excluding the dimensions of the mirrors and light sources. Whereas these components are simplified in Figure 21, the mirrors and light source models are further specified in the following section.

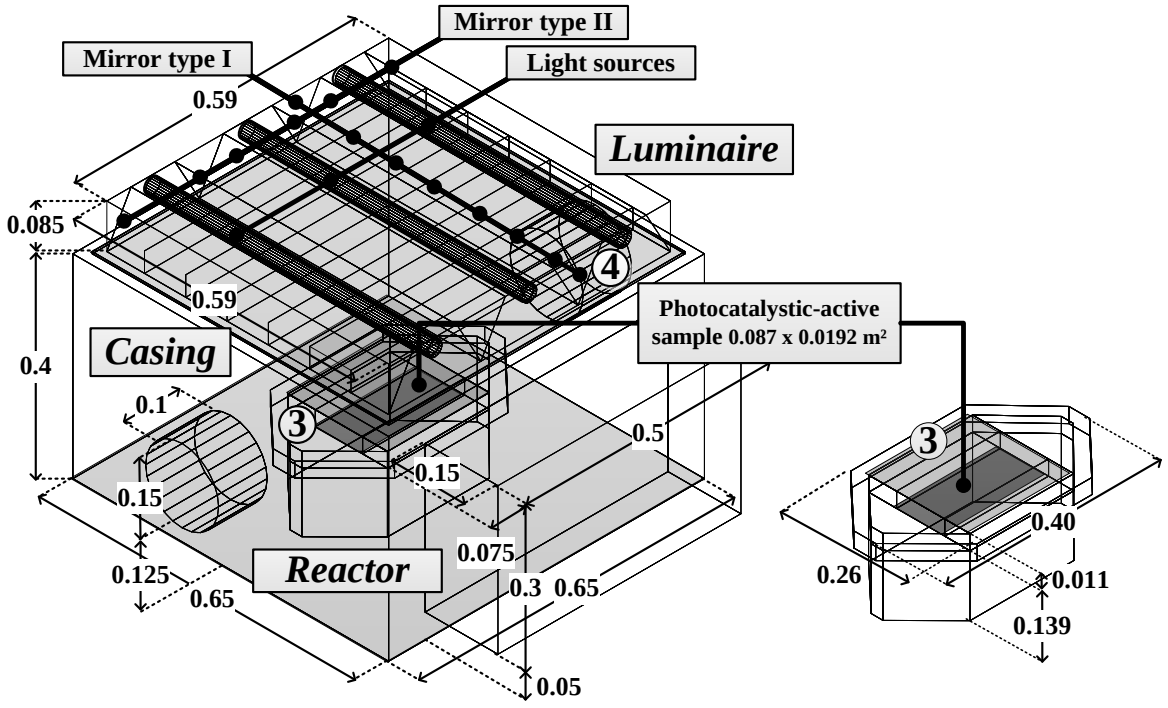

Figure 21: The main dimensions (in [m]) of the reactor setup. The main components are the luminaire, the casing and the reactor. Furthermore, the several other sub-components are identified: (1) mirrors, (2) large glass cover 5 mm, (3) small glass cover 8 mm (covering the photocatalytically active sample), (4) two tube outlets, (5) rectangular outlet.

4.2.2. **Luminaire components: mirror types and light source model**

The geometry of the light source model is presented in Figure 22a, which is composed of the (1) lamp base, (2) border region and (3) central light emitting area. Consequently, the materials *black paper*, *light1 and light2* are applied to the lamp base, border region and central light emitting area. This model was applied for all three light sources in the luminaire.

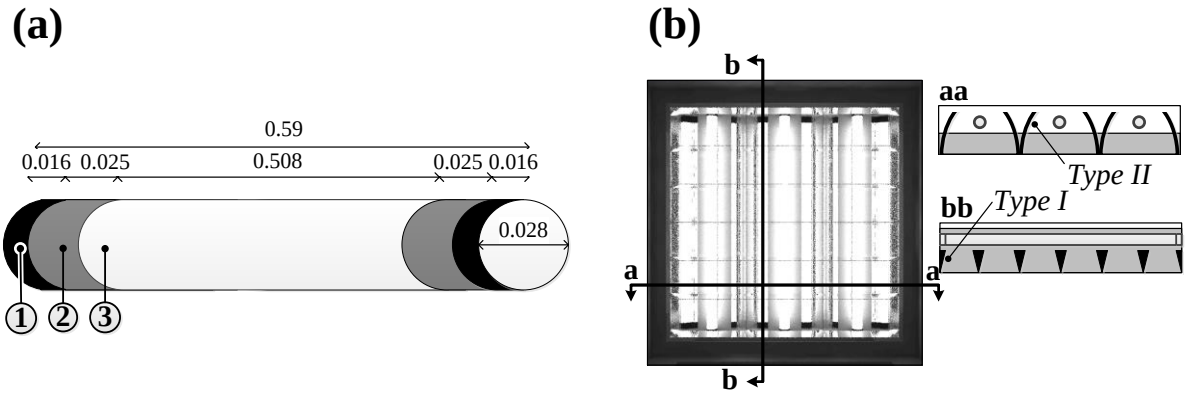

Figure 22: (a) The light source model (dimensions in mm), composed of: (1) the lamp base (no emission), (2) border region, (3) central light emitting area, which emit radiance omnidirectional, expressed by L_l [Wm^{-2}sr^{-1}]. (b) A down-top rendering of the casing in which the mirrors are schematically shown: type I and type II.

For the emission of the light source model, an omnidirectional radiance distribution over the longitudinal axis of the light source was assumed, radiating with L_l [Wm^{-2}sr^{-1}]. In turn, the radiance of both the border region and main light emitting area are related with L_l by $L_{light1} = 0.5L_l$ and $L_{light2} = L_l$ respectively. L_{light1} and L_{light2} are the radiance values applied to the material type of both surfaces. The total radiant flux of the light source model is defined by rewriting equation (2-29) and the surface description of a cylinder ($S_l = \pi dl$) to:

$$\phi_{model} = \pi^2 0.028\left(L_{light1}0.508 + L_{light2}0.05\right) \tag{4-1}$$

Where, ϕ_{model} [W] is the total radiant flux of the light source; L_{light1} and L_{light2} [Wm^{-2}sr^{-1}] are the given radiation given for the material *light1* and *light2* respectively.

In the luminaire, the two mirrors types (I & II) were composed of a base of $5{\cdot}10^{-4}$ m width (x) and 0.59 m length (z) and a curved surface generated by the gensurf command in RADIANCE. The curvature of the curved surface for type I is defined as:

$$x = b0.0045a^{2.5};\ \ y = b0.04a;\ z = b0.59a\ ;\ \ 0 \le a \le 1 \tag{4-2}$$

Similarly, the curved surface for type II is defined by:

$$x = 0.0487b(0.7606a^4 - 0.5951a^3 + 0.4611a^2 + 0.3698a - 0.0022);$$
$$y = b0.08a;\ z = b0.59a;\ \ 0 \le a \le 1 \tag{4-3}$$

Where, a [-] representing a series between 0 and 1 with $1/m$ steps, using m=25; b [m] is a constant of 1 m to correct the units; x, y and z [m] are respectively the x, y and z position of a point. The points are connected to generate 576 (= 24·24) quadrilateral surfaces per curved surface section per mirror. In total, 18 mirrors were included in the luminaire of which 12 type I and 6 type II, as illustrated Figure 22b. Both the base and the curved rim of mirrors were composed of the material type *mirror*.

4.2.3. **Materials**

Various different materials needed to be defined, as illustrated in Figure 23.

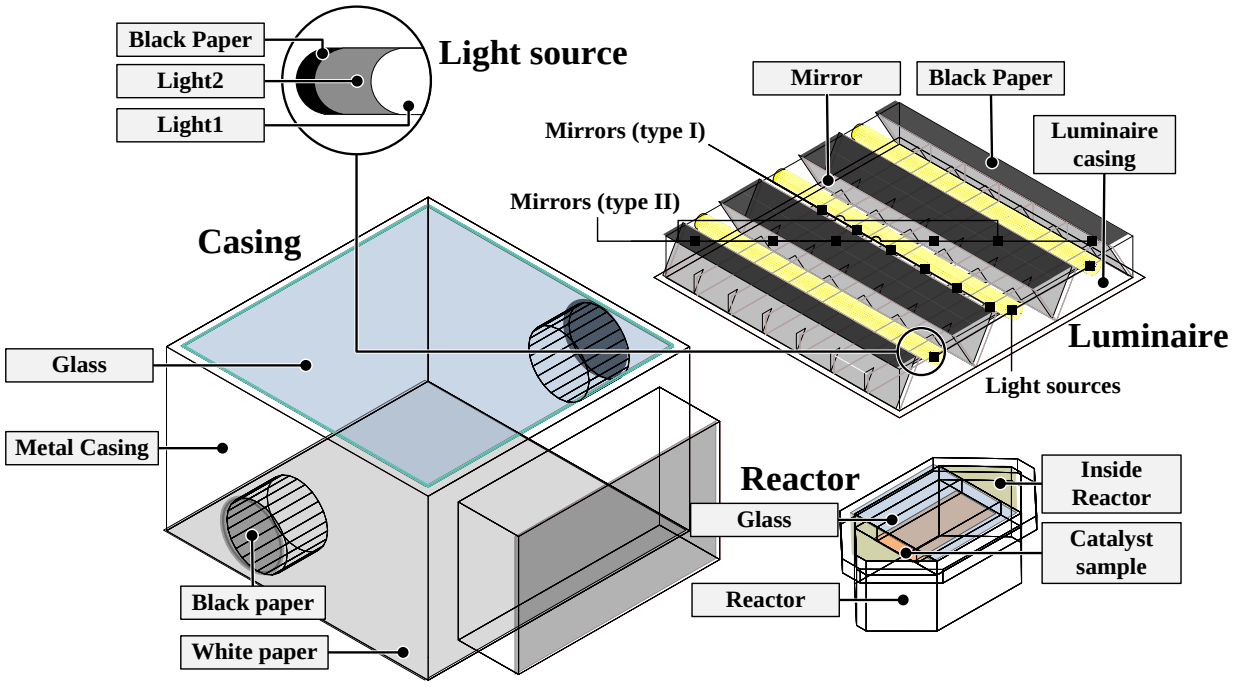

Figure 23: The materials of the three main components of the reactor setup (the casing, luminaire and reactor). In turn, the luminaire is co-composed out of the light source, mirror type I and type II sub-components.

The materials *light1* and *light2* defined the radiance originating from the light sources (the PHILIPS Master TL-D 18 W/854) and were defined in RADIANCE by:

```
# Light1
void light lighting_mat
0
0
3 L_R1 L_G1 L_B1
```

```
# Light2
void light lighting2_mat
0
0
3 L_R2 L_G2 L_B2
```

In which L_{R1}, L_{G1} and L_{B1} [W m^{-2}sr^{-1}] are the radiance component red, green and blue for *light1* and L_{R2}, L_{G2} and L_{B2} [W m^{-2}sr^{-1}] are radiance component of *light2* respectively.). Since a monochromatic model was built, $L_l = L_{R1} = L_{G1} = L_{B1} = 2L_{R2} = 2L_{G2} = 2L_{B2}$.

In turn, the *glass* material is simulated with the *dielectric* material type, which is based on Fresnel's equations [56] in a BRTDF model. The glass is modeled by:

```
# Borosilicate glass
void dielectric glass_mat
0
0
5 tR tG tB n H
```

Where t_R, t_G and t_B [m^{-1}] are the transmissivity per unit length for the components Red, Green and Blue; n [-] is the refraction index; and H [-] is the Hartmann constant which describes the linear change of n as function of the wavelength (if $H = 0$ there is no change in n as function of the wavelength). Since a monochromatic model was built, $t_R = t_G = t_B = 1$ and $H = 0$. The refraction index $n = 1.4768$ is adapted from [76], based on the verification in Section 3.2.

The remaining materials are opaque and are defined in RADIANCE by:

```
# General template for opaque materials
void metal [name]_mat
0
0
5 σR σG σB S R
```

Where σ_R, σ_G and σ_B [-] are the reflection coefficient for the components red, green and blue; S [-] is the specular component; and R [-] is the roughness coefficient. In the model, the roughness coefficient (R) of the materials was not taken into consideration ($R=0$). Normally, this value can vary within the range of 0.0-0.2 [84]. Both the reflection coefficient and specular component (S) were assumed to be equal for all wavelengths between 400-570 nm and are therefore calculated as an arithmetic average, therefore $\sigma_R = \sigma_G = \sigma_B = \sigma_{400-570}$. Sequentially, the inside of the reactor could not be measured and is assumed to have an$\sigma_{400-570}$ of 0.300. In Table 6, the input parameters of the opaque materials are reported.

Table 6: The input parameters of the opaque materials.

Material	Reflection coefficient ($\sigma_{400-570}$ [-])	Specular component (S [-])
Black paper	0.044	0.01
White paper	0.761	0.00
Luminaire casing	0.713	0.03
Metal casing	0.375	0.15
Reactor	0.678	0.03
Inside Reactor	0.300	0.00
Mirror	0.845	0.85
Photocatalytically active sample	0.883	0.01

4.2.4. **Sampling grid**

For the calibration and calculation of the irradiance on the glass cover and photocatalytically active sample surface, three sampling grid, identical to Section 3.4, were adapted. While the horizontal coordinates ($\boldsymbol{x}$ and $\boldsymbol{y}$-axis) of the sampling points in the grid were equal, their z-axis differed. A height of 139, 159 and 185 mm was adapted for the three sampling grids, as illustrated in Figure 24. They respectively correspond to the measuring heights of irradiance on the catalyst surface, the glass cover, and the calibration height.

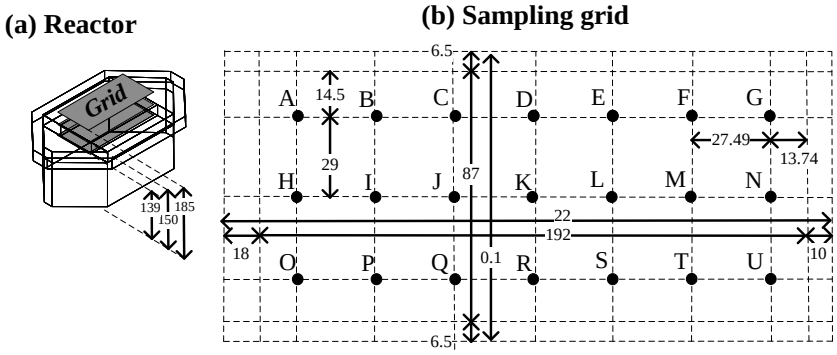

Figure 24: In the middle of photoreactor setup (a) direct above the reactor (b), the sampling grid (c) is located on a height of 185mm (dimensions are given in mm).

4.2.5. Standard rendering settings

All numerical data and renders were obtained via the settings reported in Table 7. In turn, for all other rendering parameters, the default values of RADIANCE were adapted. However, when indicated, other values for the rendering parameters may have been applied, for example for the validation of the model.

Table 7: The standard settings of the rendering parameters for the calculation of all numerical data.

-ab	-dj	-ds	-aa	-ar	-ad	-as	-dr
5	1.0	0.05	0.1	256	1024	64	4

4.2.6. Analytical calculation and error estimation

The analytical calculation was performed to understand if the effects of the glass and reflection of the photocatalytically active sample could be estimated by an analytical approximation. As illustrated in Figure 25, the analytical calculation is based on a schematic model and provides an explanation for the effects of the glass cover and the photocatalytically active sample.

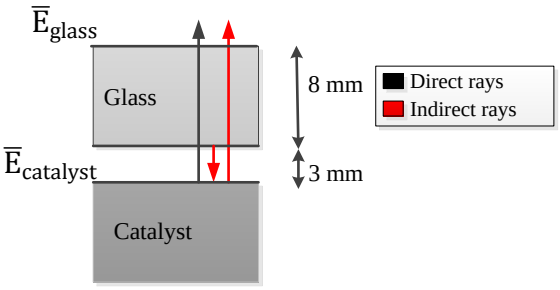

Figure 25: The schematic model of the analytical calculation.

For the derivation of the analytical calculation, the ratio between $\bar{E}_{catalyst}$ and $\bar{E}_{glass}$ is expressed by:

$$\frac{\bar{E}_{catalyst}}{\bar{E}_{glass}} = \tau_{direct} + \tau_{indirect} \tag{4-4}$$

Where $\bar{E}_{catalyst}$ and $\bar{E}_{glass}$ [Wm^{-2}] are the average irradiance on the photocatalytically active sample and glass cover respectively; and τ_{direct} and $\tau_{indirect}$ [-] are the direct and indirect transmission components. Equation (4-4) expresses the ratio between the received irradiance by the catalyst and by the glass cover of the reactor, where:

$$\tau_{direct} = \tau_{glass} \tag{4-5}$$

In which τ_{glass} [-] is the transmission of the glass cover. And:

$$\tau_{indirect} = \sum_{i=1}^{n} \left((1 - \tau_{glass})^i \sigma_{catalyst}{}^i \tau_{glass} \right) \tag{4-6}$$

Where $\sigma_{catalyst}$ [-] is the reflection coefficient; and n is the number of interactions of a ray.

Now, τ_{glass} is calculated by applying Fresnel's equation at an angle of incidence of 0 degrees:

$$\tau_{glass} = \sum_{i=1}^{n} \left(1 - \left(\frac{n_2 - n_1}{n_2 + n_1}\right)^2\right) \cdot \left(1 - \left(\frac{n_1 - n_2}{n_1 + n_2}\right)^2\right) \cdot \left(\frac{n_1 - n_2}{n_1 + n_2}\right)^{4(i-1)} \quad (4\text{-}7)$$

Where n_1 and n_2 [-] are the refraction index of respectively air and SCHOTT Borofloat® 33. Equation (4-4) can be rewritten to obtain $\overline{E}_{catalyst}$ which was initially measured in:

$$\bar{E}_{catalyst} = \bar{E}_{glass}(\tau_{direct} + \tau_{indirect}) \quad (4\text{-}8)$$

Now, the analytical model is fully defined. However, in comparison with the radiance model, the analytical calculation includes a range of simplifications. First of all, the analytical approach assumes that all rays have an angle of incidence of 0 degrees with n interactions (bounces) per ray, while the surface of the photocatalytically active sample is specular. An assessment of the analytical approach and the radiance simulations are presented in Section 4.4.1.

Furthermore, the error estimation is executed by calculating the uncertainty between the simulations and the measurements, based on numerical data obtained at 185 mm height from the sampling grid. The error estimation is performed according to:

$$\varepsilon_{eX} = 100 \cdot \left(1 - \frac{E_{sX} \pm 1.833 \cdot \frac{sd(E_{sX})}{\sqrt{n}}}{E_{mX} \pm E_d}\right), X = \{A, B \dots, P\} \quad (4\text{-}9)$$

Where ε_{eX} [%] is the error in point X; E_{sX} and $sd(E_{sX})$ [Wm^{-2}] are respectively the average and standard deviation of the simulated irradiance values for sampling point X; and E_{mX} and E_d [Wm^{-2}] are the measured irradiance and uncertainty respectively.

4.3. Validation and verification

4.3.1. Verification of the independent calculation of the RGB values

Three random sampling points of the sampling grid on 185 mm height are computed for several L_i in Figure 26 to confirm that the three components (RGB) can be calculated independently for the current applied reflection models (*metal* or *dielectric*). As can be seen in Figure 26, the amount of irradiation is linearly related with the distribution, thereby showing that the RGB components are calculated separately. Note that the starting numbers are caused by the accuracy of 5 decimal places in RADIANCE.

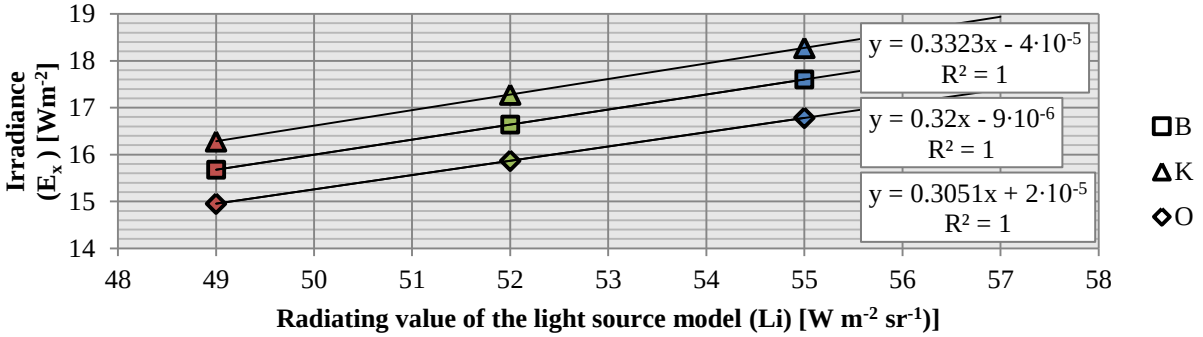

Figure 26: The linear relationship between the irradiance in point B, K and O and the emission of the light source model, expressed for by the red, green and blue component. L_i was varied by 49, 52 and 55 Wm^{-2}sr^{-1} for respectively the R, G and B components.

4.3.2. Uncertainty analysis of the –ab rendering parameter

The influence of the $-ab$ rendering parameters was considered before the actual calibration was performed. In Figure 27, the influence of $-ab$ on the average irradiance of the grid of 185 mm is illustrated, using L_l of 52 $Wm^{-2}sr^{-1}$. By using six simulations, an uncertainty interval was calculated, using equations (2-31) and (2-32). The criterion, defined in Section 2.4.3 by equation (2-33), is applied, as illustrated in Table 8. However, for a higher safety margin, a value of 5 was selected for $-ab$ rendering parameter, while a value of 3 passed the criterion test.

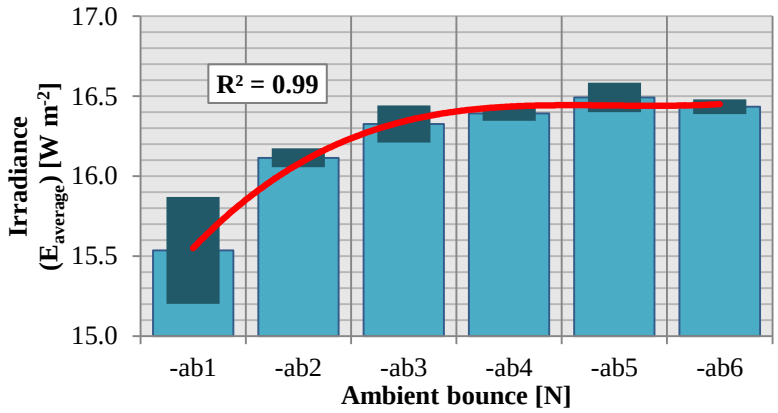

Figure 27: The average irradiance and uncertainty interval from the sampling grid on 185 mm height per 6 simulations for different ambient bounce settings, using L_l of 52 $Wm^{-2}sr^{-1}$.

Table 8: The criterion test for different $-ab$ settings, calculated according to equation (2-33).

N	$N+1$	$\bar{E}_{X;\,ab_N+1} - \bar{E}_{X;\,ab_N}$	$\frac{1.833}{\sqrt{6}}\left(sd(E_{X;\,ab_N+1}) + sd(E_{X;\,ab_N})\right)$	Criterion
1	2	0.58	0.39	False
2	3	0.21	0.18	False
3	4	0.07	0.16	True
4	5	0.10	0.14	True
5	6	-0.06	0.14	True

4.3.3. Estimating sources of a spectral error

In Section 2.4.3 was explained that during spectral rendering, spectral errors could emerge. In this modeling study, all surfaces were simulated by applying an arithmetic-averaged reflection coefficient for 400-570 nm (Section 4.2.3). Although the specular component is nearly identical for each wavelength, the reflection coefficient may differ. Therefore, the origin of any spectral error is estimated in this section.

First, the ratio between the different $-ab$ settings for average irradiance values (Section 4.3.1) was calculated on the height of 185mm, illustrated in Table 9. The ratios provide an insight into the relationship between direct and indirect incoming rays and the geometry on the incoming irradiance, as demonstrated in Figure 28.

Table 9: The average irradiance ($\overline{E}_s$) and corresponding deviation, and $\overline{E}_{s-ab[N]}/\overline{E}_{s-ab5}$ ratio and corresponding deviation per ambient bounce using the sampling grid on 139 mm height.

	$\overline{E}_s$ [Wm^{-2}]	$\overline{E}_{s-ab[N]}/\overline{E}_{s-ab5}$ ratio [%]
-ab0	7.80 ± 0.03	52.72 ± 0.39
-ab1	13.17 ± 0.05	88.99 ± 0.61
-ab2	14.37 ± 0.06	97.11 ± 0.75
-ab3	14.61 ± 0.03	98.72 ± 0.55
-ab4	14.72 ± 0.04	99.49 ± 0.59
-ab5	14.79 ± 0.05	100.00 ± 0.68

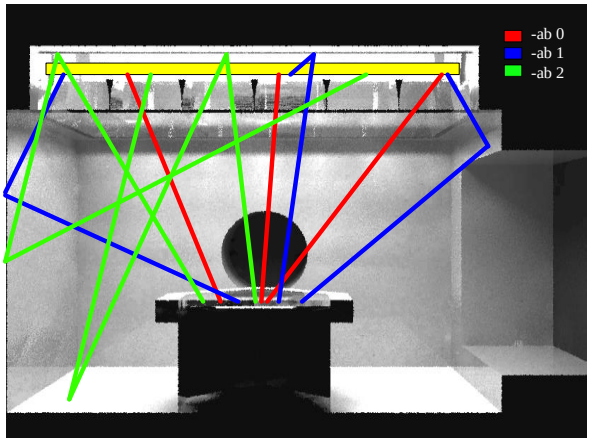

Figure 28: A cross-section of the model with several rays which are incoming on the catalyst sampling using 0, 1 or 2 interactions (reflections), by applying –ab0, -ab1 and –ab2 respectively. Note that the interactions of the *dielectric* material type are not included.

The standard deviation for $\sigma_{400-570}$ is computed to the degree of dispersion of the spectral reflection coefficients within the 400-570 nm bandwidth, calculated for each opaque material, as illustrated in Table 10.

Table 10: The standard deviation of the reflection of the opaque materials.

Material	Standard deviation of $\sigma_{400-570}$
Black paper	0.29
White paper	13.93
Luminaire casing	7.14
Metal casing	2.24
Reactor	5.29
Inside reactor	-
Mirror	1.92
Photocatalytically-active sample	2.45

The data from Table 9 and Table 10 provide more numerical-founded insight into the source of a spectral error within the model, although it is not a comprehensive analysis.

4.3.4. Calibration and error estimation

For the error estimation, the setting of L_l is estimated first by calibrating the model to the measurement results from Section 3.4. By fitting the model to the experimental data, a L_l of 53.56 $Wm^{-2}sr^{-1}$ is obtained. As can be seen in Figure 29, both the calibrated simulation and the measured results using the sampling grid at 185 mm are of similar magnitudes.

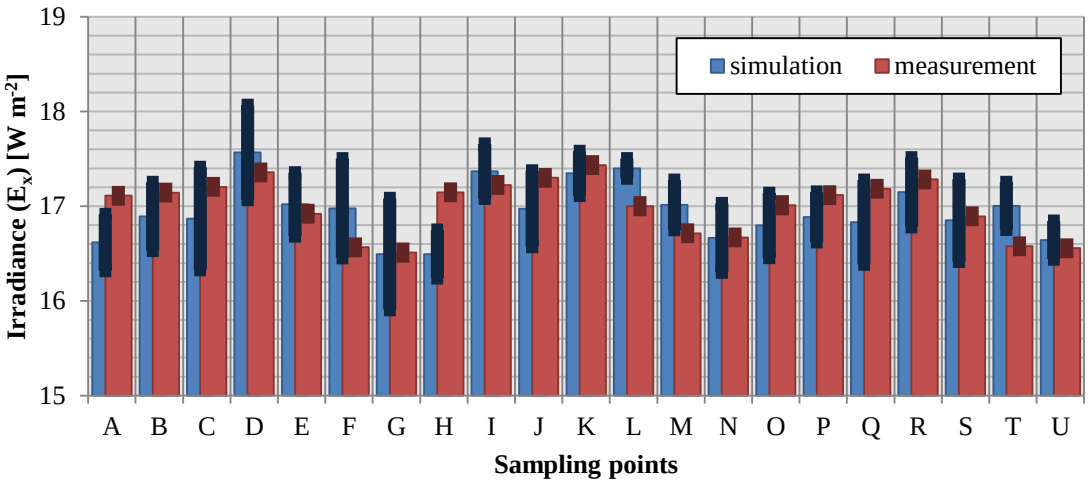

Figure 29: The calibrated simulation and measurement per sampling point (h=185 mm), using a L_l of 53.56 $Wm^{-2}sr^{-1}$.

Consecutively, equation (4-9) is applied to determine the modeling error, as demonstrated in Figure 30. The overall modeling error for all sampling points is 2.2%, while uncertainty raises the error per sampling point to a maximum of 6.2% in sampling point F. However, when the uncertainty is included in the overall error, the overall modeling error turn out to be 4.1%, which is below the commonly accepted error margin for spectral rendering of 5% [53]. Therefore, it can be assumed that the model is valid.

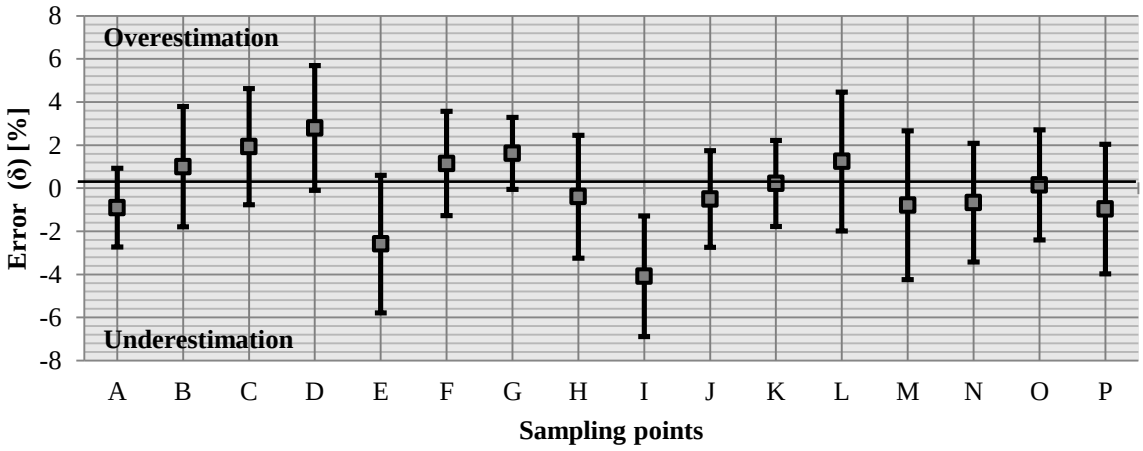

Figure 30: The error between the simulations and measurements, obtained according to equation (4-9). Both the error and the uncertainty per sampling point is illustrated.

4.4. Results

4.4.1. Irradiance distribution and equation derivation

The results of the irradiance distribution are calculated and rendered respectively with the command *rtrace* and *rpic*. First of all, the irradiance distribution on the catalyst surface ($E_{catalyst}$) is rendered, using L_l (36.65 $Wm^{-2}sr^{-1}$), as illustrated in Figure 31. The value for L_l is obtained by fitting the model to an average irradiance of 10 Wm^{-2} on the glass cover ($\bar{E}_{glass} \approx 10\ Wm^{-2}$), in line with the default value of [1]. In Figure 31, it is shown that the difference between the lowest and height values is 1 Wm^{-2}.

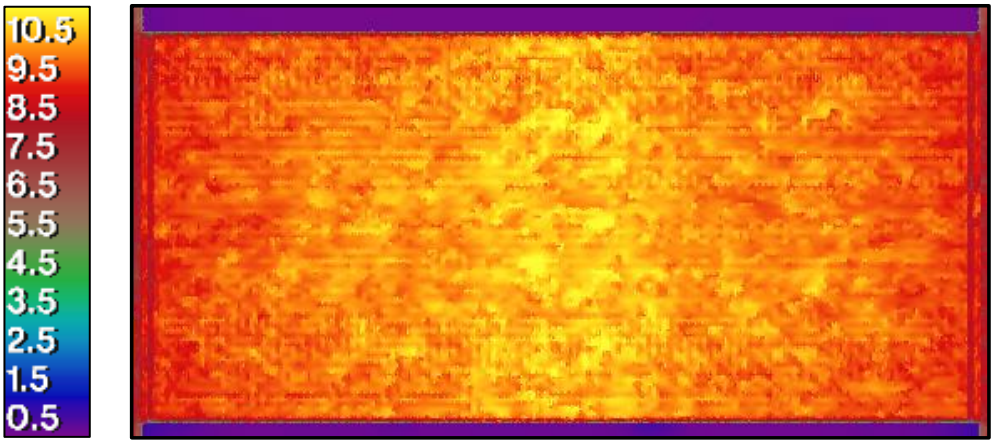

Figure 31: The distribution of for $E_{catalyst}$ in [Wm^{-2}] on a height of 139 mm, using L_l=36.65 $Wm^{-2}sr^{-1}$.

The findings of Figure 31 are confirmed by the computation of the irradiance on the sampling grid on a height of 139 and 150 mm respectively. Both height 139 and 150 mm correspond respectively to E_{glass} and $E_{catalyst}$. Figure 32 confirms the difference of 1 Wm^{-2} found in Figure 31 by a found difference of 0.98 Wm^{-2}.

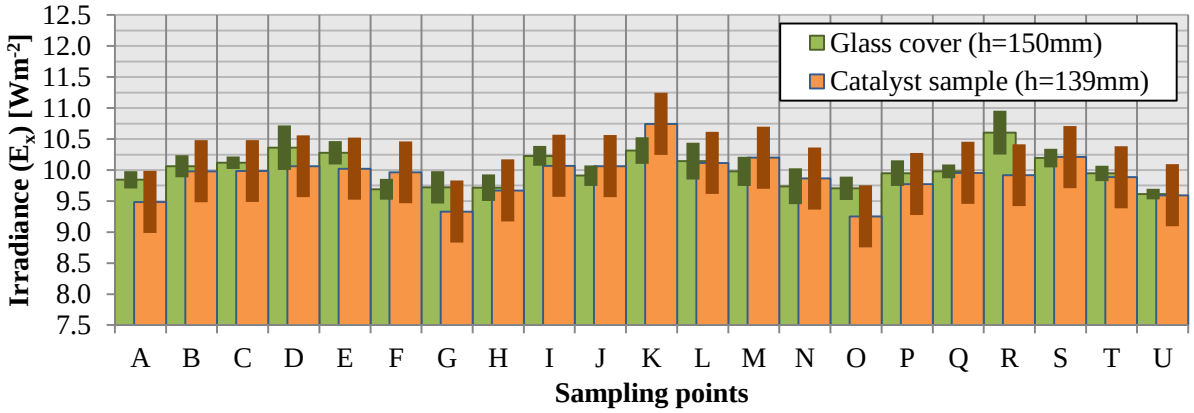

Figure 32: The $E_{catalyst}$ and E_{glass} per sampling point on a height of 139 mm and 150 mm, using L_l=34.84 $Wm^{-2}sr^{-1}$.

Furthermore, a series of simulation were performed to compute the average ratio between $E_{catalyst}$ and average E_{glass} for different reflection coefficients to the photocatalytically active sample ($\sigma_{catalyst}$). For each $\sigma_{catalyst}$, 4 simulations were performed to calculate the deviation, according to equation (2-32). In line with the simulations, the analytical calculation (Section 4.2.6) was applied for similar values of $\sigma_{catalyst}$. The results of both the analytical calculation and the simulations are illustrated in Figure 33.

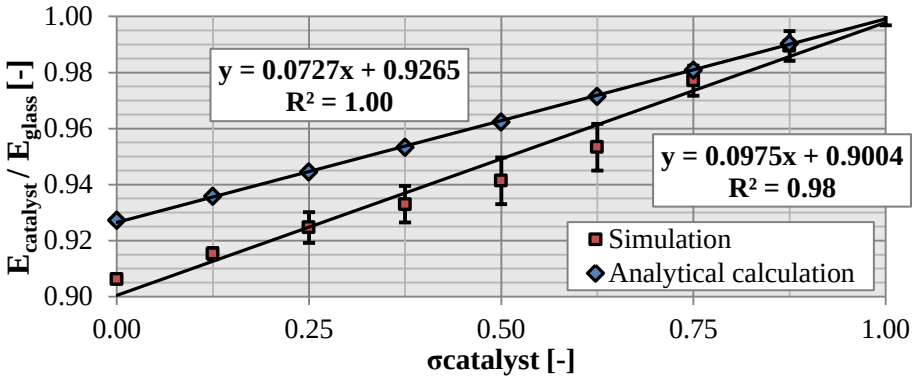

Figure 33: The ratio $E_{catalyst}/E_{glass}$ as a function of $\sigma_{catalyst}$, obtained from the simulations and analytical calculation. For both the simulation and the analytical calculation, an equation is derived.

The trend line in Figure 33 of the simulations is rewritten to a correction factor *C* [-]:

$$E_{catalyst} = E_{glass}C = E_{glass}\left(0.0978\sigma_{catalyst} + 0.9009\right) \tag{4-10}$$

Then, the kinetic model of [1] is recalled for the surface reaction of NO for an ideal mixed system:

$$r_{no} = \frac{-k_{NO}\beta K_{NO}C_{NO}K_{H_2O}C_{H_2O}D_{TiO_2}T}{\left(4k_{NO}K_{NO}C_{NO} + 2k_{NO_2}K_{NO_2}C_{NO_2}\right)\left(1 + K_{NO}C_{NO} + K_{NO_2}C_{NO_2} + K_{H_2O}C_{H_2O}\right)} \tag{4-11}$$

Where k_{NO}, k_{NO_2} and k_{H_2O} [m^2 mol^{-1} s^{-1}], β [mol m^{-2} s^{-1}], K_{NO}, K_{NO_2} and K_{H_2O} [m^3 mol^{-1}] are the rate constants of the kinetic model; and C_{NO}, C_{NO_2} and C_{H_2O} [mol m^{-3}] are the concentrations of respectively NO, NO_2 and H_2O. Sequentially, the expression *T*, which is identical in both the surface reaction expression of NO as for NO_2, is defined as:

$$T = \sqrt{\left(1 + \frac{4\alpha E\left(1 + K_{NO}C_{NO} + K_{NO_2}C_{NO_2} + K_{H_2O}C_{H_2O}\right)}{\beta K_{H_2O}C_{H_2O}}\right)} - 1 \tag{4-12}$$

Where E is the perceived irradiance by the photocatalyst; and α [mol W^{-1} s^{-1}] the irradiance related rate constant. In the photoreactor setup of [88] it was assumed that $E = E_{glass}$. Therefore, equation (4-10) can be substituted into equation (4-12) which yields the following expression:

$$T = \sqrt{\left(1 + 4\left(\frac{\alpha E_{catalyst}}{0.0978\sigma_{catalyst} + 0.9009}\right)\left(\frac{1 + K_{NO}C_{NO} + K_{NO_2}C_{NO_2} + K_{H_2O}C_{H_2O}}{\beta K_{H_2O}C_{H_2O}}\right)\right)} - 1 \tag{4-13}$$

Now, the irradiance term can be redefined, given that $E_{catalyst} = E$ in the corrected state and $\alpha/C = \alpha_c$, where α_c [mol W^{-1} s^{-1}] is the corrected rate constant, to:

$$T = \sqrt{\left(1 + 4\alpha_c E\left(\frac{1 + K_{NO}C_{NO} + K_{NO_2}C_{NO_2} + K_{H_2O}C_{H_2O}}{\beta K_{H_2O}C_{H_2O}}\right)\right)} - 1 \tag{4-14}$$

It was found that reflection coefficient for the bandwidth of 400-570 nm of the photocatalytic-active sample in [2] was 0.883. Therefore, given that α is $7.20 \cdot 10^{-6}$ mol W^{-1} s^{-1} [2], the value of $7.30 \cdot 10^{-6}$ mol W^{-1} s^{-1} is computed for α_c. As a result, the relative difference is 1.4%, which can be considered as a minor error.

4.5. Discussion

While a single simulation run yields results with an unknown deviation, more accurate results were obtained by conducting multiple simulation runs and statistics (Section 2.4.3). An uncertainty margin was derived with the central limit theorem that provided a range in which the actual numerical value was located. However, the execution of multiple simulations was more time consuming. Furthermore, with the current rendering settings (Section 4.2.5), relatively high uncertainty margins were obtained (max. ± 0.59 Wm^{-2}, average ± 0.30 Wm^{-2}). Nonetheless, the simulations were within the acceptable limit of 5% error, which is a commonly accepted error margin for spectral rendering [53]. In principle, the uncertainty margin is lowered by increasing the rendering accuracy of the rendering parameters, as was illustrated in Section 2.4.2, or increase the amount of simulations per model, as was described by equation (2-32). However, the simulation time can increase intensely, when rendering parameters are increased for more accuracy. Additionally, more accurate results are also obtained from averaged (ir)radiance values of a number of sampling points nearby each other, while using a single simulation run.

Furthermore, in the monochromatic radiance model, the surfaces with high fluctuating reflectance coefficients within the wavelength band of 400-570 nm may create a spectral error. Consequently, the approach in Section 4.3.3 gave a more comprehensive understanding the sources of a possible spectral error. The influence of both the number of bounces and the geometry on the incoming irradiance, and the standard deviation of the reflection of the opaque materials provided additional understanding. While 53% of the received irradiance by the photocatalytic sample originates directly from the light sources, more than 36% originates from single reflected rays. Practically all single-reflected rays were reflected via the mirrors in the luminaire, whereas the remaining single-reflected rays were primarily reflected via the casing. As a result, the other materials in the reactor setup had only a minor effect on the incoming radiation. For example, the paper (ground surface), the black paper (covering material) and reactor geometry have nearly no effect on the received irradiance (≈ 3%). Moreover, the materials which affected the fourth bounce had a negligible impact on the irradiance (> 0.5%). Therefore, the materials *luminaire*, *reactor*, and the *white paper* which had the highest deviation of $\sigma_{400-570}$ (Table 10) and thus could be largest potential sources of a spectral error, provide little contribution to the total irradiation on the catalyst surface. Probably the largest spectral error was caused by the casing. Still, no comprehensive quantification method for the spectral error was proposed and therefore future work is required.

In addition, an alternative notation for α is proposed despite the notation of [1]. Since α [mol W^{-1} s^{-1}] can be written as α [mol J^{-1}], as [W] = [Js^{-1}], the Stark–Einstein law (also known as the Photochemical Equivalence Law) can be applied. The Stark–Einstein law is given by:

$$E_{mol}(\lambda) = N_a h\, c/\lambda \tag{4-15}$$

Where $E_{mol}(\lambda)$ [J $Einstein^{-1}$] is the amount of energy per photons mole with wavelength λ;c [m s^{-1}] is the speed of light in vacuum ($2.99792458 \cdot 10^{8}$ m s^{-1} [87]); N_a [mol^{-1}] is Avogadro's constant ($6.02214 \cdot 10^{-23}$ mol^{-1}); h [Js] is Planck's constant ($6.62607 \cdot 10^{-34}$ Js [87]); λ [m] is the wavelength of the photons.

Next, the definition of the quantum yield, ϕ_q [mol/Einstein], is recalled [40]:

$$\phi_q = \frac{r_{act}}{E_a[einstein\ m^{-2}s^{-1}]} \tag{4-16}$$

Where E_a does not quantify light in [Wm^{-2}], but in [Einstein $m^{-2}s^{-1}$]. Additionally, the definition of the reaction rate of the photocatalyst activation in [1] is recalled:

$$r_{act} = \alpha E_a \tag{4-17}$$

Where r_{act} [mol m^{-2} s^{-1}] is the reaction rate of the photocatalyst activation. Now, both equation (4-15) and equation (4-17) may be substituted into (4-16) and rewritten to:

$$r_{act} = \alpha E_a = \int_{\lambda 1}^{\lambda 2} E_a(\lambda) \frac{\phi_q(\lambda)}{E_{mol}(\lambda)} d\lambda = E_a \bar{\lambda}_{\lambda 1;\lambda 2} \frac{\phi_q}{N_a hc} \tag{4-18}$$

Where, $\lambda 1$ and $\lambda 2$ [m] are respectively the lower and upper boundary of the integral of the wavelength band (which are 400 nm and 570 nm for the current model). Furthermore, $\bar{\lambda}_{\lambda 1;\lambda 2}$ [nm] is average wavelength of the wavelength bandwidth. It should be remarked that this expression is similar to [40]. Optionally, the expression in equation (4-18) can be applied in future work for a more fundamental description of photocatalyst activation per wavelength.

During modeling it was found that the default light emitting materials in RADIANCE do not support reflection. Typical radiance model include real-size rooms where the reflection of light sources can be neglected. It is believed that in the reactor setup model, the reflection by the light emitting materials on the total irradiance on the catalyst surface is insignificant. However, more research is required to investigate this assumption.

Furthermore, while photocatalytically active sample in the present study was irradiated uniformly, for an actual room size, it is believed that the irradiance distribution cannot be regarded as uniform anymore. As a result, PCO efficiency will be strongly influenced by the location of the photocatalyst in the room due to radiance dispersion. This assumption will be further investigated in Chapter 6.

4.6. Conclusion

A series of simulations were performed in RADIANCE to gain understanding of the effect of the glass cover and photocatalyst in the behavior of irradiance received by photocatalyst surface in the reactor. The data could not be obtained through experimental means, since the irradiance on the surface of photocatalyst was affected by both the glass plate glass cover and photocatalyst. Also, the analytical calculation could not predict the effects correctly. Therefore, an equation was derived from the radiance model, and provided the relationship: $E_{catalyst} = (0.0978\sigma_{catalyst} + 0.9009)E_{glass}$. Where, E_{glass} and $E_{catalyst}$ [Wm^{-2}] are respectively the incoming irradiance glass cover and catalyst; and $\sigma_{catalyst}$ [-] the reflection coefficient of the catalyst-sampling surface. This equation was substituted into the kinetic model of NO_x [1]. Consequently, the rate constant α ($7.20 \cdot 10^{-6}$ mol $W^{-1}s^{-1}$) was replaced by α_c ($7.30 \cdot 10^{-6}$ mol $W^{-1}s^{-1}$), implying that the actual irradiance on the photocatalyst surface was approximately 1.4% lower than initially was assumed [1, 3]. Moreover, the reflection of the photocatalytically active sample limits the irradiance reduction of the glass cover. Therefore, in [1], when using a light substrate, no significant error was made. However, when darker substrates were to be used in the experimental setup, the actual irradiance can be overestimated up to 9.8%. As a result, if same experiments in [1] are repeated with the same setup, while using a darker substrate, a considerable error will be introduced.

Chapter 5. Second modeling study: the ideally mixed room

5.1. Introduction

During the previous investigation on the NO_x conversion in the benchmark room [2], low conversions (1-4%) were computed, suggesting that the photocatalyst was ineffective. However, a higher conversion, up to 100%, is desirable for effective air purification within buildings. It is presumed that raising NO_x conversion can be done by increases the mixing of the air inside the room. In [2], the effects of different flow conditions were analyzed to a narrow extend, as the effects of mixing were not considered.

In contrast, the current work considers the maximum attainable NO_x conversion in an ideal mixing flow under various indoor conditions by a validated numerical method in Matlab Simulink, based on the benchmark room [4]. To approach ideal flow conditions, an ideal flow model is developed to analyze an ideal mixed flow and an ideal plug flow, based on the theory of Section 2.6. The ideal plug flow is used to validate the method with the experiments of [3], while the ideal mixed flow is constructed to predict NO_x conversion in the ideally mixed room. The models are constructed from ordinary or partial differential equations (respectively ODE's or PDE's) through which the mass / mole balance equations and the mass fraction conservation equation could be defined. The differential equations were solved using the ODE113 solver algorithm in Matlab Simulink version R2012a. The method was verified with an analytical approach for which a first-order reaction in respectively an ideal mixed flow and an ideal plug flow was calculated. Since at low discretization a modeling error was introduced in the ideal plug flow, an estimation method for the discretization error was proposed. After verification and validation, the maximum attainable NO_x conversion in the ideally mixed room under various indoor conditions was studied. In the following section, the method for the construction of the first-order reactions in the ideal flow model and the analytical calculations are explained.

5.2. Methodology

5.2.1. The ideal flow model for the first-order reaction of compound *p*

Equation (2-44) and equation (2-45) presented in Section 2.6 are applied as a starting point for the construction of the ideal flow model of arbitrary compound *p*. The ideal flow model of compound *p* is used to verify the numerical method of both flow types and to verify the estimation method for the discretization error, used for estimation of the plug flow reactor [3]. First of all, for the required ODE definitions, the $\dot{m}_{r;p;j}$ term from equation (2-44) is defined for the first-order reaction rate for compound *p*. Therefore, the mass flow $\dot{m}_{r;p;j}$, which is created by the first order surface reaction of compound *p* in segment *j*, is defined in the model by:

$$\dot{m}_{r;p;j} = M_p k_{1st} A_c C_{p;j} = M_p k_{1st} A_c \gamma_{p;j} \rho_{air} \tag{5-1}$$

Where k_{1st} [m s^{-1}] is the first order reaction rate; and $\gamma_{p;j}$ [-] is the mass fraction of compound *p* in section *j* for which is substituted $\gamma_{p;j} = \gamma_{p;x+1}$. Sequentially, substitution of equation (5-1) and equation (2-45) into equation (2-44) yields the final definition of the required ODE:

$$dm_{p;j}/dt = Q\gamma_{p;x}\rho_{air} - Q\gamma_{p;x+1}\rho_{air} + M_p k_{1st} A_c \gamma_{p;x+1} \rho_{air} \tag{5-2}$$

Where $\mathrm{d}m_{p;j}/\mathrm{d}t$ is the term which representing the change in mass of compound *p* in segment *j* due to time (which is equal to zero in a steady state). The variable $\gamma_{p;x+1}$ in equation (5-3) is solved by the ODE113 solver. Next, the analytical calculations are described.

5.2.2. **Analytical equations**

The analytical calculation for a steady-state expression for a first order reaction rate of compound p in an ideal mixed reactor is defined as [74]:

$$C_{p;out} = \frac{C_{p\_in}}{1 + \frac{a_v k_{1st} V_r}{Q}} \tag{5-3}$$

Where C_{p_in} and $C_{p;out}$ [mol m^{-3}] is the concentration of compound p at respectively the inlet and the outlet or in the reactor; V_r is the volume of the reactor in which an ideal mixed flow is assumed. Furthermore, a_v is defined as 1/ h_r; where h_r [-] is the height of the reactor. In turn, the steady state expression for a first order reaction rate of compound p in an ideal plug flow reactor is defined by [74]:

$$C_{p;out} = C_{p;in} exp\left(-\frac{k_{1st} k}{Q}\right) \tag{5-4}$$

Where, for the ideal plug flow, $Q = u_x h_r d_r$, given that u_x [m s^{-1}] is the velocity magnitude in the *x* direction; and h_r and d_r [m] are respectively the height and depth of the reactor in which the ideal plug flow is assumed. With both equations (5-3) and (5-4) the numerical model in Section 5.3 is validated.

5.2.3. **The ideal flow model of NO_x**

In agreement with Section 5.2.1, the principles of Section 2.6 for both modeling reactor setup [3] and the ideally mixed room model are adapted described by the ideal flow model of NO_x. For the ideal flow model of NO_x, an additional PDE for the mass fraction conservation in segment *j* is required, denote by $\gamma_{air;j}$[-], in which five compounds are considered (i.e. NO, NO_2, H_2O, O_2 and N_2). Also, two PDE's for the mass balance of respectively NO and NO_2 are needed. To decrease iteration times, all terms in the two mass balances are divided by the molar mass (M) of the corresponding compound. Therefore, the PDE for NO is defined as a mole balance in segment *j* as:

$$\frac{dn_{NO;j}}{dt} = 0 = Q\frac{\rho_{air}}{M_{NO}}\left(\gamma_{NO;x} - \gamma_{NO;x+1}\right) + r_{NO;j} A_c D_{TiO2} \tag{5-5}$$

Where n_{NO} [mol] is the amount of NO; M_{NO} [kg mol^{-1}] is the molar mass of NO (≈ 0.03 kg mol^{-1}); $\gamma_{NO;x}$ and $\gamma_{NO;x+1}$ [-] are the mass fractions of NO of the air at respectively the position *x* and *x+1*; A_c [m^2] is the amount of photocatalyst-coated surface in the room; and ρ_{air} [kg m^{-3}] is the density of air. Note that, $\gamma_{NO;x+1}$ also represent the mass fraction in segment *j*, where segment *j* is considered to be ideally mixed. Likewise, for NO_2 the PDE is defined as a mole balance for segment *j*:

$$\frac{dn_{NO_2;j}}{dt} = 0 = Q\frac{\rho_{air}}{M_{NO_2}}\left(\gamma_{NO_2;x} - \gamma_{NO_2;x+1}\right) + r_{NO_2;j} A_c D_{TiO_2} \tag{5-6}$$

Where n_{NO} [mol] is the amount of NO_2; and M_{NO_2} [kg mol^{-1}] is the molar mass of NO_2 (≈ 0.046 kg mol^{-1}); and $\gamma_{NO_2;x}$ and $\gamma_{NO_2;x+1}$ [-] are the mass fractions of NO_2 at respectively the position x and x+1. Lastly, the PDE for the mass fraction conservation is defined as:

$$\frac{d\gamma_{air;j}}{dt} = 0 = 1 - \gamma_{NO;x+1} - \gamma_{NO_2;x+1} - \gamma_{H_2O;x+1} - \gamma_{O_2;x+1} - \gamma_{N_2;x+1} \tag{5-7}$$

Where $\gamma_{H_2O;x+1}$, $\gamma_{O_{2;x+1}}$ and $\gamma_{N_{2;x+1}}$[-] are the mass fractions of respectively H_2O, O_2 and N_2 in segment *j*.

The variables $\gamma_{NO;x+1}$, $\gamma_{NO_2;x+1}$ and $\gamma_{N_2;x+1}$ are solved by the ODE113 solver in Matlab Simulink. In turn, the kinetic model of NO_x is applied for the definition of $r_{no;j}$ and $r_{no2;j}$ in segment j [1]:

$$r_{no;j} = -k_{NO}\beta K_{NO} C_{NO;x+1} K_{H_2O} C_{H_2O;x+1} T_j D_{TiO_2} \tag{5-8}$$

$$r_{no2;j} = \beta\left(k_{NO} K_{NO} C_{NO;x+1} - k_{NO_2} K_{NO_2} C_{NO_2;x+1}\right) K_{H_2O} C_{H_2O;x+1} T_j D_{TiO_2} \tag{5-9}$$

$$T_j = \frac{\sqrt{1 + \frac{4\alpha E_s\left(1 + K_{NO} C_{NO;x+1} + K_{NO_2} C_{NO_2;x+1} + K_{H_2O} C_{H_2O;x+1}\right)}{\beta K_{H_2O} C_{H_2O;x+1}}} - 1}{\left(4k_{NO} K_{NO} C_{NO;x+1} + 2k_{NO_2} K_{NO_2} C_{NO_2;x+1}\right)\left(1 + K_{NO} C_{NO;x+1} + K_{NO_2} C_{NO_2;x+1} + K_{H_2O} C_{H_2O;x+1}\right)} \tag{5-10}$$

Where $C_{NO;x+1}$, $C_{NO_2;x+1}$ and $C_{H_2O;x+1}$ [mol m^{-3}] are the concentration of respectively NO, NO_2 and H_2O in segment j; and D_{TiO_2}[-] is the photocatalyst dosage.

Since a mass fraction notation is used for the expression of the compound quantities, the concentration parameters in the kinetic model, $C_{NO;x+1}$, $C_{NO_2 x+1}$ and $C_{H_2O;x+1}$, require circumscription to the mass fraction notation. Therefore, for compound p, the mass fraction is related with concentration by the following relation:

$$C_P = \gamma_P \rho_{air} / M_P \tag{5-11}$$

Equation (5-11) is substituted in the kinetic model, defined by equations (5-8)-(5-10), to obtain the surface reaction rates from the mass fraction parameters, including Y_{NO}, Y_{NO_2} and Y_{H_2O}, for respectively NO, NO_2 and H_2O. Furthermore, in [1, 3] the concentrations were expressed in [ppm] rather than [mol m^{-3}]. Likewise, given that the average molar density of air (n_{air} at 293.15 K, 101325 Pa) is 41.59 mol m^{-3} [88] ($n_{air} = \rho_{air}/M_{air}$). The concentration of compound p can be expressed in [ppb] by:

$$C_P[ppb] = C_P / n_{air} \cdot 10^9 \tag{5-12}$$

It should be noted that while [1] applied a [ppm] as default unit, in this report the default expression of concentration is [mol m^{-3}] is, except if reported otherwise. Now, a conversion factor is derived by substituting equation (5-11) into equation (5-12), with which the concentration of compound p [ppb] is expressed into mass fraction by:

$$\gamma_P = C_P[ppb] \frac{M_P n_{air}}{\rho_{air} 10^9} \tag{5-13}$$

With equation (5-13), the data from [1, 3] can be converted and applied in the model and vice versa. In Appendix 3, both an overview of the complete Simulink model and the code of the ideal flow model for NO_x, can be found. The model is constructed with equations (5-5)-(5-13). Additionally, the performance indicator, $NO_{x_{con}}$, which represents the conversion ratio of NO_x, to compute the final results, with is defined as [3]:

$$NO_{x_{con}} = \frac{\left(\gamma_{NO\_in} - \gamma_{NO}\right)/M_{NO} + \left(\gamma_{NO_2\_in} - \gamma_{NO_2}\right)/M_{NO_2}}{\gamma_{NO\_in}/M_{NO} + \gamma_{NO_2\_in}/M_{NO_2}} \tag{5-14}$$

Next, the boundary conditions and rate constants need to be defined for simulation of the ideally mixed room and the reactor setup.

First of all, for the modeling of the reactor setup of [3], the rate constants and the boundary conditions are respectively reported in Table 11 and Table 12. Sequentially, the rate constants and the boundary conditions for the ideally mixed room model are respectively reported in Table 13 and Table 14.

Table 11: The rate constants for the experimental setup [3], adapted from [1].

Rate constant	Value	Unit
α	$7.200 \cdot 10^{-6}$	mol W^{-1} s^{-1}
β	$1.03 \cdot 10^{-7}$	mol m^{-2} s^{-1}
K_{NO}	20.9	m^3 s^{-1}
K_{NO_2}	5.38	m^3 s^{-1}
K_{H_2O}	$2.39 \cdot 10^{-3}$	m^3 s^{-1}
k_{NO}	$5.35 \cdot 10^{-13}$	m^2 mol^{-1} s^{-1}
k_{NO_2}	$1.98 \cdot 10^{-13}$	m^2 mol^{-1} s^{-1}

Table 12: The standard / varying parameters and constant values of the experimental setup [3], based on [3].

Parameters				Constant values		
Variable	Standard conditions	Varying conditions	Unit	Variable	Value	Unit
Q	$5 \cdot 10^{-5}$	$1.667 \cdot 10^{-5}$ - $8.333 \cdot 10^{-5}$	$m^3 s^{-1}$	ρ_{air}	1.204	kg m^{-3}
C_{NO_in}	500	100 - 1000	ppb	M_{NO}	$30.0062 \cdot 10^{-3}$	kg mol^{-1}
$C_{NO_2\_in}$	0	0	ppb	M_{NO_2}	$46.0058 \cdot 10^{-3}$	kg mol^{-1}
γ_{H_2O}	$7.3 \cdot 10^{-3}$ *	$1.46 \cdot 10^{-3}$ - $14.6 \cdot 10^{-3}$	-	M_{H_2O}	$18.0153 \cdot 10^{-3}$	kg mol^{-1}
E_s	10	1 - 13	Wm^{-2}	γ_{O_2}	0.189581	-
A_c	0.016704 **	-	m^2	-	-	-

*** For 50% RH at 293.15 K; ** A_c= 0.087·0.192 m^2 [3].**

Table 13: The corrected rate constant, adapted from Chapter 4.

Rate constant	Value	Unit
α_c	$7.30 \cdot 10^{-6}$	mol W^{-1} s^{-1}

Table 14: The standard parameters and constant values of the ideally mixed room model, based on [3].

Parameters				Constant values		
Variable	Standard conditions	Varying conditions	Unit	Variable	Value	Unit
Q	$1.17 \cdot 10^{-2}$	$7 \cdot 10^{-3}$ - $4.3 \cdot 10^{-2}$	$m^3 s^{-1}$	ρ_{air}	1.204	kg m^{-3}
C_{NO_in}	500	125 - 1000	ppb	M_{NO}	$30.00615 \cdot 10^{-3}$	kg mol^{-1}
$C_{NO_2\_in}$	0	0	ppb	M_{NO_2}	$46.00580 \cdot 10^{-3}$	kg mol^{-1}
γ_{H_2O}	$7.3 \cdot 10^{-3}$ *	$1.46 \cdot 10^{-3}$ - $14.6 \cdot 10^{-3}$	-	M_{H_2O}	$18.01532 \cdot 10^{-3}$	kg mol^{-1}
E_s	2	0 - 5	Wm^{-2}	γ_{O_2}	0.189581	-
A_c	23.352	0 - 46.70	m^2	-	-	-
D_{TiO_2}	0.50	0.02 - 0.50	-	-	-	-

*** For 50% RH at 293.15 K**

The volumetric flow rate or the air change rate per hour (ACH) in the ideally mixed room is defined by applying the Dutch standards. Generally, the ACH of the ideally mixed room model is calculated from the volumetric rate flow according to:

$$ACH = \frac{3600 \cdot u_{in} 0.168}{V} \tag{5-15}$$

Where V [m^3] the volume of the benchmark room (27 m^3); and u_{in} is the inlet velocity perpendicular to the inlet surface which is 0.168 m^2. Since an office function is assumed for the ideally mixed room, the Dutch regulations indicate that $1.3 \cdot 10^{-3}$ m^3 s^{-1} per m^2 occupiable area is required. Therefore, when assuming that the room is 1 m deep, an occupiable area of 9 m^2 (1·9) is obtained which gives a volumetric flow rate of $1.17 \cdot 10^{-2}$ $m^3 s^{-1}$ or an ACH of 1.56 h^{-1}. Additionally, a minimum volumetric flow rate for a room of $7 \cdot 10^{-3}$ $m^3 s^{-1}$ is demanded [89], which relates to an ACH of 0.93 h^{-1}. Both ACH values were tested.

Furthermore, the radiance amount used in [2] and [3] of 10 Wm^{-2} was found to be somewhat excessive, as will be concluded in Chapter 6 later on. Therefore, a lower amount of irradiance, between the 0-5 Wm^{-2}, is applied. The quantities are in the same order of magnitude as the irradiance for general office activities as will be reported in Section 6.2.6. For the remaining boundary settings of the ideally mixed room, the values of [3] were adopted.

5.2.4. **The discretization error estimation**

A method is proposed for the discretization error estimation of the ideal plug flow. For the definition of this method, the approach of the grid independence index (normally used for CFD model verification) is adapted [90, 91] as starting point. The numerical model of the ideal plug flow should be calculated for multiple variants in which a different quantity of segment is applied according to the theory of Section 2.6. Based on [91], the discretization error, $\varepsilon_{d;m}$ [%], is estimated for any compound p according to:

$$\varepsilon_{d;m} = 100F \frac{\left|C_{p;out;m} - C_{p;out;mr}\right|}{C_{p;out;m}(r^p - 1)} \tag{5-16}$$

Where $C_{p;out;rm}$ and $C_{p;out;m}$ [mol m^{-3}] are the concentration of compound p at the outlet of respectively the variants with rm segments and m segments; F [-] is the safety factor; r [-] is the refinement factor; and p [-] is the order of convergence. In turn, the order of convergence is required, calculated by [91]:

$$p = \frac{ln\left(\epsilon_{mr,m} / \epsilon_{mr^2;mr}\right)}{ln(r)} \tag{5-17}$$

For which three variants with varying segments (i.e. m, mr, mr^2) of the model are needed, and where:

$$\epsilon_{mr,m} = C_{p;out;mr} - C_{p;out;m} \tag{5-18}$$

$$\epsilon_{mr^2;mr} = C_{p;out;mr^2} - C_{p;out;mr} \tag{5-19}$$

The estimation method of the discretization method is verified in Section 5.3.1.

5.3. Verification and validation

5.3.1. Verification with the analytical calculations

In this section, the ideal mixed flow model for compound *p*, as was outlined in Section 5.2.1, and the analytical calculations, presented by equation (5-3) and equation (5-4) are compared for verification of the method. For the first order rate constant (k_{1st}) a value of 0.01 $m^{-1}s^{-1}$ is applied as standard value. For the remaining parameters, the standard values of Table 14 are adapted. Furthermore, an absolute tolerance, of 10^{-15} is applied in Simulink, implying that data is calculated up to 15 decimal places. The error between the analytical and numerical approach is calculated according to the following definition:

$$\varepsilon_{model} = 100\frac{\left|C_{p;out;analytical} - C_{p;out;numerical}\right|}{C_{p;out;analytical}} \quad (5\text{-}20)$$

Where ε_{model} [%] is the error of numerical approach, $C_{p;out;analytical}$ and $C_{p;out;numerical}$ [mol m^{-3}] are the outlet concentrations of compound p for respectively the analytical calculation and numerical approach.

Now, analytical calculation for a steady state expression in an ideal mixed reactor, denoted in equation (5-3), is compared with the numerical method using a discretization amount (m) of 1. As a result, the concentration of compound *p* at position x+1 is equal to the outgoing concentration. As is evident from Table 15 and Table 16, where correspondingly the parameters $C_{p;in}$ (Table 15) and k (Table 16) for both methods are compared, the data of the numerical model is nearly identical to the results from the analytical approach.

Table 15: The error of the numerical approach, using equation (5-3) for various $C_{p;in}$.

$C_{p;in}$ [mol m^{-3}]	$5.19875\cdot10^{-06}$	$1.03975\cdot10^{-05}$	$2.0795\cdot10^{-05}$	$4.1590\cdot10^{-05}$
ε_{model} [%]	0.029	0.012	0.009	0.002

Table 16: The error of the numerical approach, using equation (5-3) for various $C_{p;in}$.

k [m^{-1} s^{-1}]	0.0005	0.001	0.01	0.03	0.05	0.1	0.4	1
ε_{model} [%]	0.008	0.016	0.009	0.021	0.035	0.006	0.027	0.0003

Consequently, the numerical approach is also verified for an ideal plug flow in which a first-order reaction rate of compound *p* is calculated (Section 5.2.1), by applying the analytical calculation from equation (5-4). In line with the previous verification, again the standard conditions from Table 14 and a k_{1st} of 0.01 $m^{-1}s^{-1}$ are applied. Also, an absolute tolerance, of 10^{-15} was applied for the numerical approach. While for the ideal mixed flow a m of 1 was applied, or for the ideal plug flow with higher m for minimization of the discretization error. As a result, a m of 256 was selected. Generally, when m was doubled, ε_{model} halved. Additionally, the conversion of the compound p was calculated, according to:

$$p_{con} = 100\frac{\gamma_{p\_in} - \gamma_{p\_out}}{\gamma_{p\_in}} \quad (5\text{-}21)$$

Where p_{con} [%],γ_{p_in} [-] and γ_{p_in} [-] are respectively the conversion, mass fraction at the inlet and outlet of compound p.

In turn, both the conversion and the absolute error are calculated for various k and A_c, which are reported in Figure 34. At high conversions, higher errors were found, as illustrated in Figure 34. For example, above a k of 0.15 $m^{-1}s^{-1}$, an ε_{model} of > 4.97% was found (p_{con} = 99.3%,). However, for p_{con} > 99.3%, both the analytical calculation and numerical model both still yielded comparable values for p_{con}. Likewise, above A_c of 0.25 m^2, an ε_{model} of > 4.95% was found, for which an p_{con} of approximately 99.3% was computed, for both the analytical calculation and numerical model. Based on this data, it is concluded that the absolute error in the numerical model below $C_{p;out} < 2.94 \cdot 10^{-07}$ mol m^{-3} is $\varepsilon_{model} <$ 5% and only occur at p_{con} > 99%, due to the declining outlet concentration. However, the difference in p_{con}, for both the numerical model and analytical calculation, remains negligible for the whole conversion range between 0-100%. Therefore, it is concluded that the numerical model is accurate in approximating of the outlet concentration below 99.3% conversion and the conversion of p for 0-100% conversion.

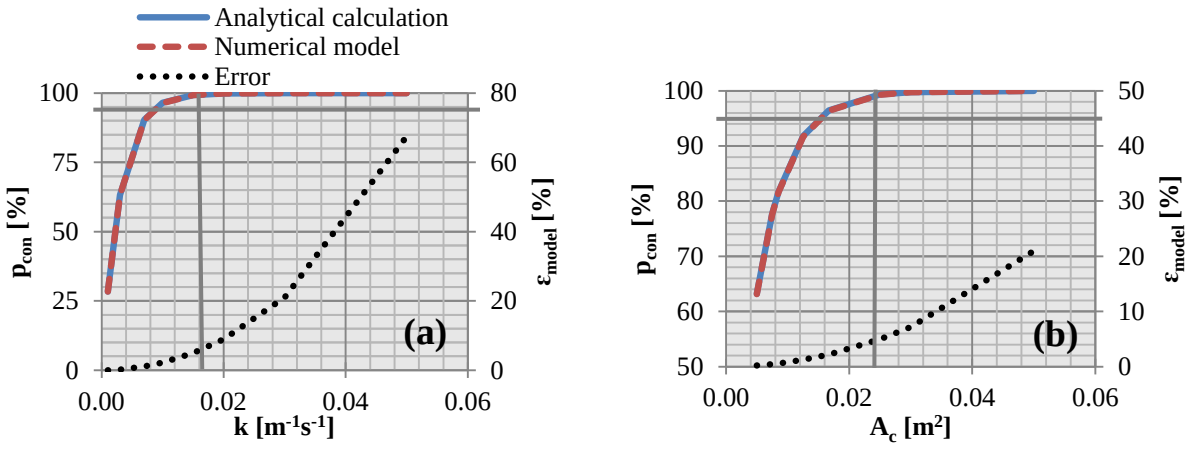

Figure 34: The conversion, p_{con}, and absolute error, ε_{model}, of the numerical model for the parameters: (a) k and (b) A_c.

5.3.1. Verification of the discretization error estimation method

For the verification of the discretization error estimation method (Section 5.2.4), both ε_{model} and $\varepsilon_{d;m}$ are compared. For the comparison of the two error definitions, equation (5-4) is applied, using the standard conditions from Table 14 a k of 0.01 $m^{-1}s^{-1}$ and an absolute tolerance of 10^{-15}. In turn, $\varepsilon_{d;m}$ is calculated by applying a refinement factor of 2 and a F of 1.2. As is evident for Figure 35, the results for both ε_d and ε_{model} are similar. Therefore, it can be concluded that the discretization error estimation method is satisfactory. Successively, the discretization error of the ideal plug flow model can be estimated in the next section.

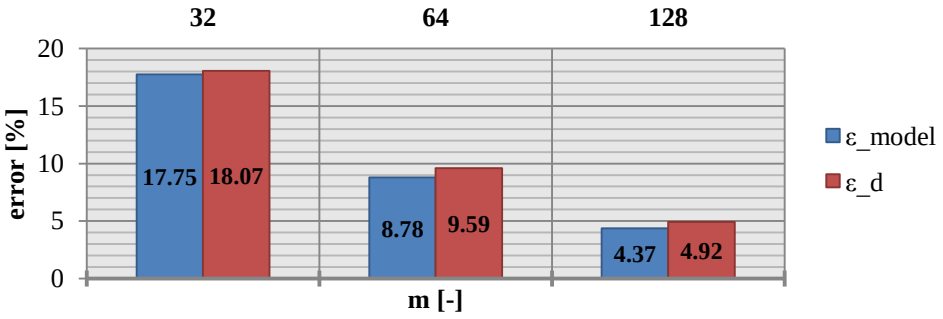

Figure 35: Comparison between ε_d and ε_{model} for different amount of segment (m[-]), using the ideal plug flow.

5.3.2. Validation with experimental results

The discretization error of the numerical model of the reactor setup [3] is estimated, based on the suggested method from Section 5.2.4. The standard conditions from Table 12 were applied to estimate the discretization error of the model. In turn, the $C_{NO2;out}$ [ppb] is used to derive the discretization error, according to the equations (5-16)-(5-19). The discretization error, $\varepsilon_{d;m}$ [%], is illustrated in Figure 36.

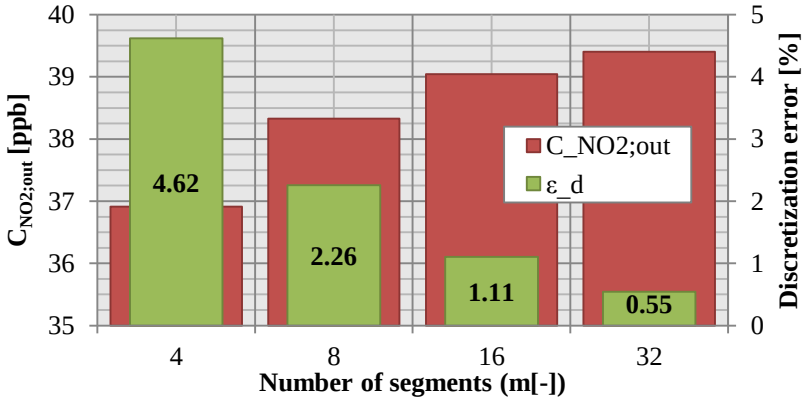

Figure 36: The discretization error, $\varepsilon_{d;m}$ [%], and $C_{NO2;out}$ [ppb] calculated using different number of segments.

Based on the findings of Figure 36, a m of 32 is adopted to minimize the discretization error. Subsequently, the reactor model is compared with the experimental results [3]. In [3], 23 samples were taken during the experiment in which different experimental conditions were applied. The comparison between simulation and the experimental data for both C_{NO} and C_{NO2} in Figure 37 suggest that the numerical model is able to approximation the experimental data with only a small degree of error. The numerical values of the comparison can be found in Appendix 4.

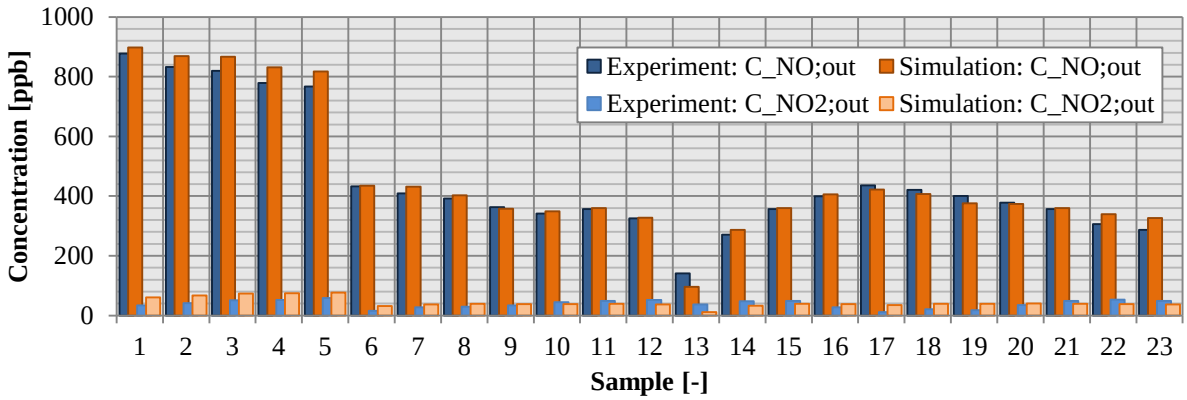

Figure 37: The outlet concentration for NO_x: Comparison between experimental results of [3] and the reactor model using the kinetic model of NO_x [1] for the different samples.

Since the reactor model could be successfully applied to estimate the experimental results, the same model is applied for the simulation of the reactor, using only a single segment ($m = 1$). The results of the ideally mixed room are reported in the next section.

5.4. Results

As can be seen from Figure 38, the effects of the ideal mixed flow conditions on the conversion of NO_x in the benchmark room, according to the standard condition of Table 14, for several varied parameters is observed. For a number of conditions, 100% conversion of NO_x is achieved.

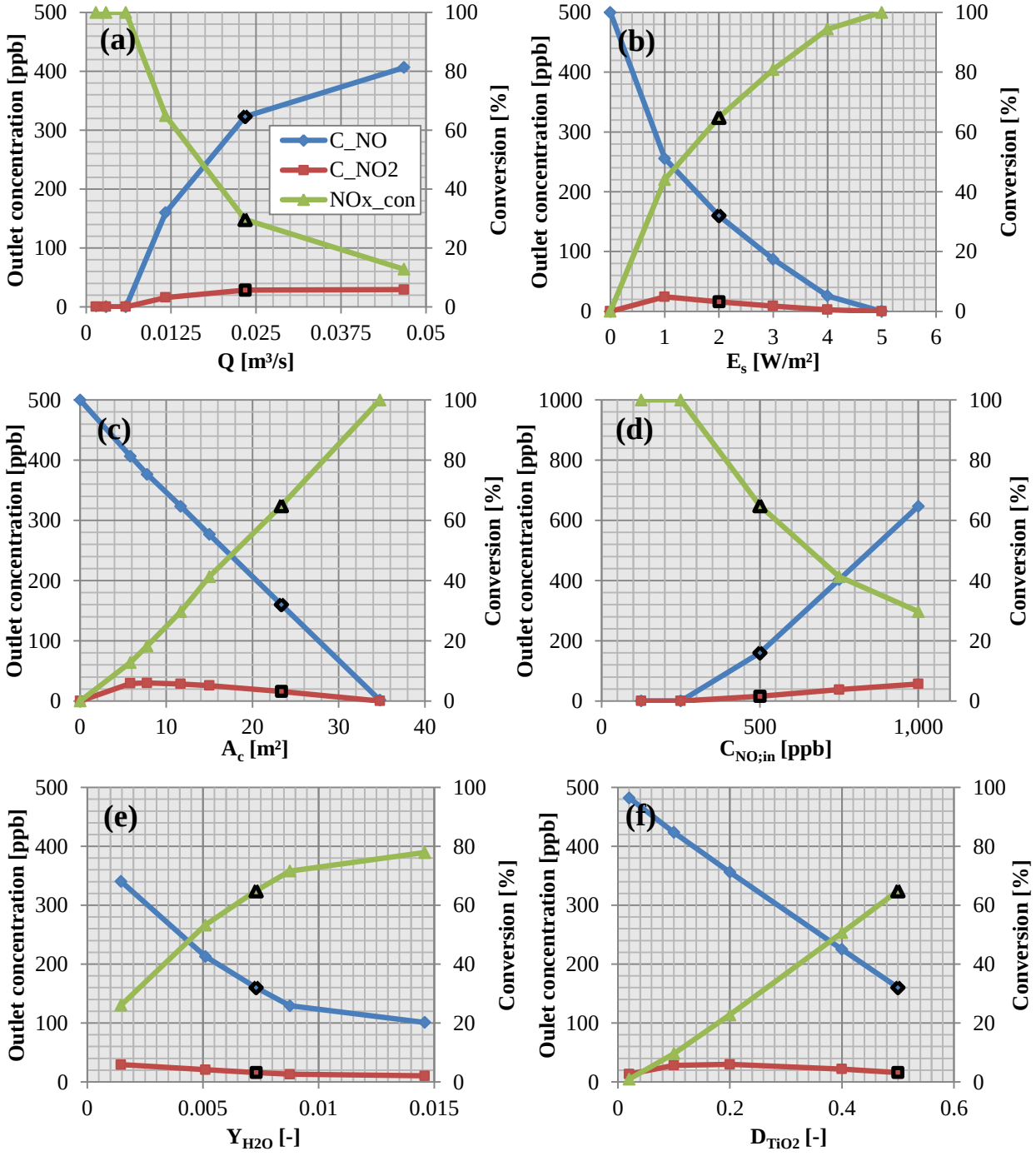

Figure 38: The effects on the conversion and outlet concentrations of NO_x in an ideally mixed room as function of (a) the volumetric flow rate, (b) the irradiance, (c) the photocatalyst-coated surface, (d) NO inlet concentration, (e) mass fraction of water and (f) catalyst dosage. Note that the marked black-lined dots represent the standard conditions.

5.5. Discussion

In nearly ideal mixed systems, the amount of energy needed to mix the air is excessive. In fact, in the ideally mixed room, the air velocity is instantaneous, implying that the energy in the system is infinite. However, it is improbable that a nearly ideal mixed state can be achieved in real room, since the mixing options are limited in contrast to stirred tank reactors. For example, an agitator is typically used to promote mixing in these reactor types, but cannot be applied in the room. Furthermore, the local flow velocities in the room are restricted to avoid the experience of discomfort by occupants, as high velocities subject the occupants to draught. The experience of draught is a temperature-dependent statistical concept that is mainly experienced around the neck and face area and is induced by air velocities between 0.1-0.4 m s^{-1} corresponding with 18-21 °C [92]. As a result, at an ACH of 0.224 (Q = $1.68 \cdot 10^{-4}$ $m^3 s^{-1}$), the local air velocities at the inlet of the ideally mixed room exceed 0.1 m s^{-1}, allowing the experience of draught. Still, these air velocities occur above 2.5 meters are outside the occupied area. A wide-ranging range of factors may affect the experience of comfort and need to be considered during optimization-strategy development for the PCO technology in the built environment, since they may restrict the effectiveness.

In addition, even though the experimental results were successfully approximated by the numerical method, a serious limitation of the model was discovered. During simulation, within the majority of the experimental boundary conditions, the model could easily converge to a correct solution. Moreover, the current method allows dynamic adjustment of the input within this margin without interrupting the simulation process. This allowed multiple results to be obtained within a single simulation run. However, while keeping the other parameters constant, for low initial conditions ($Y_{NO}, Y_{NO2} << 10^{-6}$) and for boundary conditions with which 100% NO_x conversion could be obtained, the model converged to negatively physical-incorrect values ($Y_{NO}, Y_{NO2} < 0$). This implied that the square root term within the exponential expression of the kinetic model in equation (5-10) becomes negative and obviously cannot be computed. As a result, during dynamically adjustment of the input, the model could not converge back to previously obtained results, but acquired new values. This posed a numerical limitation which has implications for numerical modeling. In fact, several CFD models were unsolvable as reported in Section 6.4.6. Therefore, possible solutions will be recommended later in Section 7.2.

5.6. Conclusion

During this second modeling study, a validated numerical model of the reactor setup for NO_x [3] was developed in MATLAB Simulink, using forward discretization. The discretization error in the model was assessed by a verified method so that the reactor setup model could be used as a starting point for the simulation of an ideal mixed flow in the benchmark room. Under standard conditions in the ideally mixed room (Q = $1.17 \cdot 10^{-2}$ $m^3 s^{-1}$ or ACH = 1.56 h^{-1}; C_{NO_in} = 500 ppb; $C_{NO_2\_in}$ = 0 ppb; RH = 50% or γ_{H_2O} = 0.0073; E = 2 Wm^{-2}; A_c = 23.352 m^2; D_{TiO_2} = 0.5) was found that, 65% of NO_x could be converted. However, for low NO_x concentrations (C_{NOx} < 250 ppb), low volumetric flow rates (Q < $5.85 \cdot 10^{-3}$ $m^3 s^{-1}$), high catalyst-coated area (A_c > 35 m^{-2}) and high irradiance values (E > 5 Wm^{-2}), negative values for Y_{NO} and/or Y_{NO2} were obtained, suggesting that 100% conversion of NO_x was acquired. As was discussed, for these conditions the kinetic model posed a limitation to numerical simulation. Furthermore, the found NO_x conversion rates were substantial higher than previously found results in [2] and suggested that mixing of flow significantly enchants the effectiveness of PCO technology. However, since a new implementation approach is suggested (Section 2.7), a new comparison with additional CFD models is performed in the following chapter to verify this suggestion.

Chapter 6. Third modeling study: the room model

6.1. Introduction

In [2], an analysis of the influence of the indoor parameters on PCO performance in a 2-dimensional real-scale CFD benchmark room model was performed, based on [4]. In the present study, the following effects, including a typical office irradiance distribution related to human activity, different inlet locations, turbulence at the inlet, and different catalyst dosage both under normal and ideal mixed flow conditions are studied. These parameters can play a key role in the application of PCO technology in the built environment. In addition, two indicators for assessment of flow characteristics and identification of flow stagnation are explored. Finally, the new CFD models were extended by incorporating a typical office irradiance distribution, employing the improved kinetic model from Chapter 4 and the newly suggested implementation method, discussed in Section 2.7.

The radiance model and a conversion factor (to relate the photometric and radiometric variables) are used to estimate the irradiance quantity and distribution, based on the general activities of the occupants. The relation between required irradiance and illuminance values was computed by a derived conversion factor from the emission measurement (Section 3.5). The conversion factor allows the required illuminance values for a general activity (Section 2.5.2) to be related with the amount of available irradiance for the induction of photocatalytic activity.

Additionally, three indicators are explored for the assessment of flow characteristics and identification of flow stagnation within the CFD models. First of all, concept of the age of air is introduced to numerically determine the stagnation of flow in the room. In addition, two additional parameters are calculated from the age of air, including the air change efficiency and the degree of uniformity. These two indicators can provide additional insight into the flow characteristics of the in the room and may be related to photocatalytic performance.

Also, the effects of dosage of the photocatalyst are studied by the CFD model and compared with the ideally mixed room model, which was developed in the previous modeling study (see Chapter 5). This comparison provides insight into the maximum optimization potential of PCO technology by increasing the mixing in a flow. As will be reported in Section 6.2.3 and was discussed in Section 5.5, a complication was encountered in models with high catalyst dosage values that resulted in high NO_x conversion and generated complex numbers. A low catalyst dosage was set as standard value, to promote solvability.

Consistent with [2], the CFD models were meshed with Gambit v.2.4.6 and simulated in FLUENT v.6.3. In turn, the kinetic model is defined by an User Defined Functions (UDF) using volume-based approach adapted from [2], while the implementation method of Section 2.7 is applied. In the following sections, the methods of the CFD and radiance model setup are explained.

6.2. Methodology

6.2.1. The benchmark model

The previous CFD model from [2], representing an office room, is the starting point for the construction of the CFD models in this last modeling study. The dimensions of the room model, based on a validated two-dimensional benchmark model from [4], as exemplified in Figure 39a. As can be seen from Figure 39a, the four wall sections of the room are named and printed in green, whereas the ducts and the room are respectively highlighted in blue and orange. During the modeling, these wall sections were individually or collectively coated with the photocatalyst to study the degradation behavior of NO_x. In agreement with [2], the kinetic model of [1] is applied per wall section in a volume-based reaction in the adjacent cells near the corresponding wall section, as illustrated in Figure 39b. Additional details are discussed in the next section, where the variant definition is explained. Furthermore, in contrast to [2], in this study the outlet of the room is extended by 0.6 m to a total of 0.9 m, in order to promote full flow development downstream at the outlet boundary for all variants with alternative inlet positions. This prevents recirculation of air at the outlet.

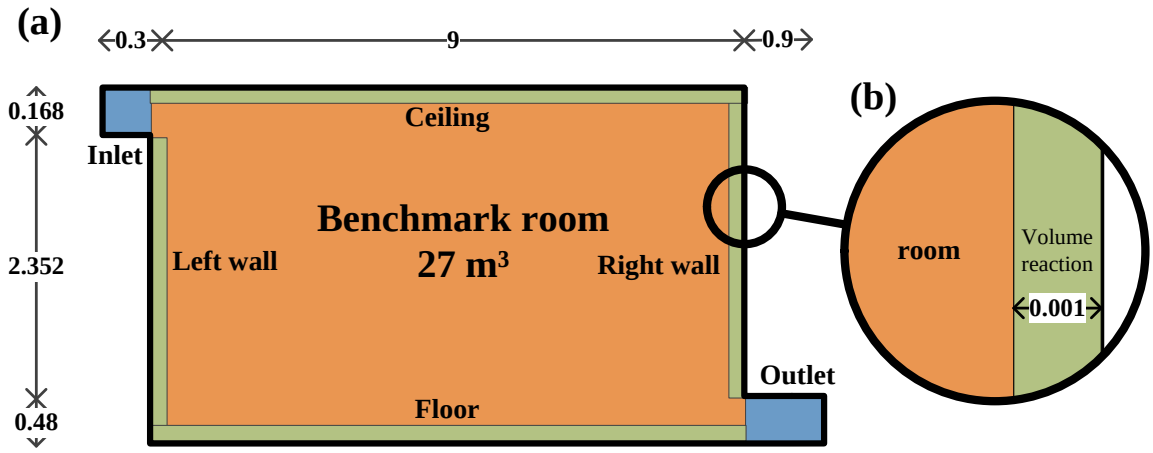

Figure 39: The benchmark room and named boundaries (not on scale), adapted from [2]. The red zone is the main room, while the green areas are the ventilation duct for the inlet and outlet respectively. Furthermore, the blue areas are the volumes in which the kinetic model is applied as source term.

6.2.2. Variant definition

As demonstrated in Figure 40, in total five geometries or cases for the CFD modeling are constructed to analyze the influence of the parameters previously named in the introduction. The first case, which will be the standard case, is constructed from the benchmark model geometry [4]. Meanwhile the inlets in the other cases (2, 3, 4, and 5) are either displaced and/or rotated. Even so, each case has an identical volume of 27.4824 m^3 (including ducts), and an equal amount of photocatalyst surface area: 23.352 m^2.

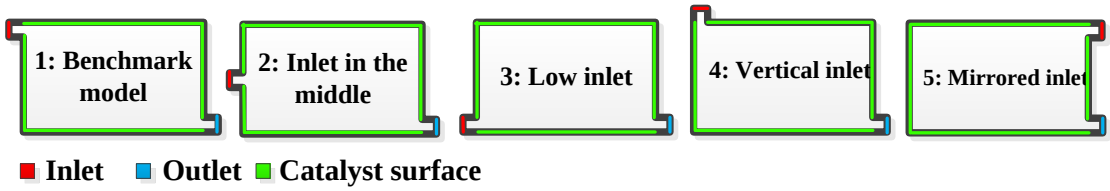

Figure 40: The different cases in used during this modeling study.

As stated previously in the introduction, the effect of several considered parameters, include varying in the Air Change rate per Hour (ACH) and the inlet pollutant concentration based on two pollution types (viz. NO and NO_2), the irradiance quantity based on an activity and a typical office irradiance distribution, the turbulence intensity at the inlet and the catalyst dosage in both an ideal mixed and default flow. The parameters and their standard and varying conditions will be briefly explained in the following sections.

First of all, the ACH and pollutant concentration at the inlet are explained. As was demonstrated in [2], higher ACH values lower the conversion of NO_x by the photocatalyst. In this report, the effects on NO_x degradation by different two pollution types are analyzed by alternating the ACH.

Initially the ACH values of 0.5 h^{-1}, 1 h^{-1}, 2 h^{-1} and 4 h^{-1} are selected as varying values, while an ACH of 0.5 h^{-1} is set as default value. In all cases, the ACH is associated with the inlet velocity (v_{in}[m s^{-1}]) by:

$$ACH = \frac{3600 \cdot Q}{V} = \frac{3600 \cdot v_{in} 0.168}{V} \tag{6-1}$$

Where Q [$m^3 s^{-1}$] is the volumetric flow rate; V [m^3] the volume of the room; and v_{in} is the inlet velocity (perpendicular to the inlet surface).

Equation (6-1) will later on be applied to calculate the NO_x mass fractions at the inlet for the pollution types (Table 17). First, however, the pollution types need to be identified. By default, an outdoor source is assumed to generate NO_x pollution, in accordance with [2]. However, the characteristics of the outdoor source are compared with an external indoor source in an adjacent room, as classified in Figure 41.

Figure 41: The pollution types which are considered during this study: Type a is located indoors while type b originates from outdoors and is the default pollution type used in this study. Note that both sources are external sources.

For type A, a local indoor pollution source inside an adjacent room is considered from which the air is being ventilated into the room. Meanwhile, for type B, an ambient outdoor pollution levels is considered. The two sources seem the identical, although their emissions diverge when the ACH is changed. For example, when the ACH is increased, the mass flow of a pollutant for type B will increase, whereas the mass flow for type A remains unchanged. Observably, for outdoor pollution, the mass flow is assumed to be infinite, since the outdoor air is observed as bulk. In contrast, the mass flow in the adjacent room is limited to the mass flow generated by the local source.

Numerically, for both pollution types in the room, the inlet mass fraction (Y_{p_in} [-]), inlet velocity (v_{in} [m s^{-1}]) and mass flow at the inlet for arbitrary compound p ($\dot{m}_{p\_in}$ [kg s^{-1}]) are related by:

$$\dot{m}_{p\_in} = Q \rho_{air} Y_{p;in} = v_{in} 0.168 \rho_{air} Y_{p;in} \tag{6-2}$$

Where ρ_{air} is the air density (1.18775 kg m^{-3} at 293.15 K and 101325 Pa, according to FLUENT[1]).

[1] *Note that the actual air density is 1.204 kg m^{-3} at 293.15 K and 101325 Pa*

To facilitate the interpretation of equation (6-2), it is rewritten to:

$$Y_{p\_in} = \frac{\dot{m}_{p\_in}}{v_{in} 0.168 \rho_{air}} \tag{6-3}$$

For further quantification, the correct mass fractions for NO_x need to be identified from literature. Generally, the formation of NO_x in ambient air is formed by several combinations of oxygen and nitrogen at high temperatures during the combustion process, where, on the average, 90 – 95% of the NO_x is emitted as NO and 5 – 10% as NO_2 [37]. However, the formation of NO_x near buildings is dependent on local conditions and originates from a wider range of both human activities, including primarily the combustion of fossil fuel, and natural processes, such as lighting biomass burning and microbiological emissions from soil [38]. Frequently, NO concentrations between 1-366 µg m^{-3} are found outdoors, whereas indoors a range of 1-264 µg m^{-3} is regularly present [39]. Furthermore, it is estimated that a typical household on the average emits 1 µg s^{-1} NO_x [36].

With the foregoing data, a numerical definition of the types of pollution is obtained by applying equations (6-1) and (6-2). Since, the current kinetic model of NO_x is valid for concentrations between 0.1-1 ppm NO [3], which is 0.13-1.30 mg m^{-3} [1] or Y_{no}0.1-1.095·10^{-6}, a value higher than the typical household emission is selected. Still, these values are within a similar magnitude with the data found in literature. Consequently, the NO_x mass flow is enlarged to 5 µg s^{-1}, composed of 90% NO and 10% NO_2. Therefore, a mass flow for NO and NO_2 of respectively $\dot{m}_{NO;in}$ = 4.5·10^{-9} kg s^{-1} and $\dot{m}_{NO_2;in}$ = 0.5·10^{-9} kg s^{-1} at 0.5 h^{-1} ACH are selected. While these mass flows will be fixed for pollutant type A, the values for pollutant type B will differ per ACH. According to equation (6-3), this implies that the NO_x mass fractions change per ACH for type B, while the NO_x mass fractions change per ACH remain the same for type A, as reported in Table 17.

Table 17: The ventilation rates and the corresponding mass fraction of NO_x for the pollution types. The dark grey row is only adapted for pollutant type B, while for type A all values are adapted, dependent on the ACH.

ACH [h^{-1}]	u_{in} [m s^{-1}]	Y_{NO_in} [-]	C_{NO_in} [kg m^{-3}]	C_{NO_in} [ppb]	$Y_{NO_2\_in}$ [-]	C_{NO2_in} [kg m^{-3}]	C_{NO2_in} [ppb]
0.5	2.27202·10^{-2}	9.92580·10^{-7}	1.18·10^{-6}	955	1.10287·10^{-7}	1.31·10^{-7}	69
1	4.54405·10^{-2}	4.96290·10^{-7}	5.89·10^{-7}	478	5.51433·10^{-8}	6.55·10^{-8}	35
2	9.09910·10^{-2}	2.48145·10^{-7}	2.95·10^{-7}	239	2.75717·10^{-8}	3.27·10^{-8}	17
4	1.81762·10^{-1}	1.24072·10^{-7}	1.47·10^{-7}	119	1.37858·10^{-8}	1.64·10^{-8}	9

Additionally, the values for the irradiance are defined. Since the radiation distribution and conversion function are not yet explained (see Section 6.2.5), only the activities for which a certain range of illuminance are required are appointed. Based on the theory of Section 2.5.2, three illuminance categories are selected, including category D, F and G. These category D, F and G categorize respectively the performance of visual tasks of high contrast or large size, of low contrast or very small size and of low contrast or very small size over a prolonged period, according to [69]. In turn, category D is set as a default reassembling general office activities. In the radiance model, the required illuminance values will be observed on the working plane, which is imaginary horizontal plane at 0.8 m height from the floor, as will be further explained in Section 6.2.4 later on. While For the default illuminance category, the illuminance value of 500 lx maintained, for the other categories a value of respectively of 1000 lx and 2000 lx is selected.

In the previous chapter, Chapter 5, ideal mixing seem to increase photocatalytic activity significantly. Therefore, it is plausible that turbulence may also promote the conversion of NO_x though mixing at the inlet. The internal turbulence in the inlet is dependent on the upstream history of the flow and defined by the properties of the inlet duct and is defined by both duct and grill design. In Fluent, turbulence is defined by the turbulence intensity. Generally, the turbulent intensity (I_{in} [%]) is explained as the ratio of the root-mean-square of the velocity fluctuations to the mean flow velocity and is defined as [93, 94]:

$$I_{in} = \frac{v'}{v_{in}} \tag{6-4}$$

Where v_{in} [m s^{-1}] is the (mean) velocity; v′ [m s^{-1}] is the root-mean-square of the turbulent velocity fluctuations. During modeling, a default turbulence intensity of 4% is applied [4]. However, the turbulent intensity of the inlet is varied by 2%, 8% and 16%. A turbulence intensity of < 1% may be considered low, while values of > 10% can be considered high [94].

As was shortly explained in the introduction and in Chapter 5, the current kinetic model for NO_x limits numerical modeling possibilities, since complex numbers can be generated during simulation. Consequently, as will be pointed out in Section 6.4.6, several CFD models were unsolvable due to the generation of complex numbers in specific cells. To promote solvability, a D_{TiO2} of 0.02 is applied as default condition which is lower than the standard conditions given in [3]. However, for commercial coatings, addition additives need to be added to the mixture of the coating to promote its mechanical performance. Furthermore, in related literature, lower dosage were found: 0.05 [95] or 0.1-0.2 [96].

6.2.3. The CFD models: Grid and model definitions

For each case, a 2D grid was developed, created on the dimensions of benchmark model by using the pre-processing software Gambit. During the grid construction, the starting principles from [2] were adapted to create non-uniform structured quadrilateral-based grids. The grids were refined near the boundaries and outlet to promote solvability of the turbulence model in the models and decrease the parameter gradients between individual cells. The enlargement ratio between cells was retained below 1.2 to promote accuracy. Per model, three zones are defined, including the ducts, the room and the photocatalyst-coated boundary. Both an overview of the zones and grids are illustrated in Figure 42.

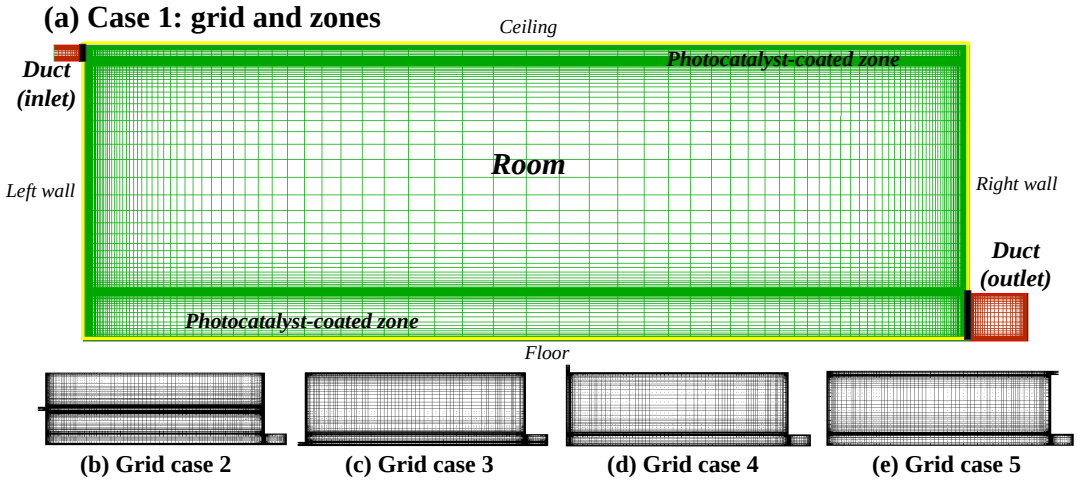

Figure 42: The grids, associated zones and wall sections. The grids of the other cases are based on the first case.

Consecutively, in Table 18, the foremost grids parameters of the models are reported. In addition, a grid independence test (GCI) was performed to determine the grid qualities, found in Section 6.3.2.

Table 18: The foremost grid parameters of the cases.

Case	Number of cells	Faces	Nodes
1	23962	48302	24341
2	32288	64997	32710
3	24899	50162	25264
4	22197	44752	22556
5	23497	47357	23861

As was described in Section 6.2.1, the kinetic model of NO_x [1], was implemented as a volume-based reaction rather than a surface reaction. The kinetic model was implemented over in a zone adjacent to a photocatalyst-coated wall in a cell layer of 1 mm width, using a User Defined Function (UDF). According to [2], this volume-based approach can be implemented without significant error in the model (≈ 0.1%). However, the alternative implementation method for the volume-based approach, previously described in Section 2.7, was applied in order to prevent modeling the errors. A validation of the method is reported in Section 6.3.4. Furthermore, the description of the UDF can be found in Appendix 6.

The governing equations, which define the physical properties in the CFD models, were adapted from [2]. In short, a compressible Newtonian fluid was assumed in which the buoyancy forces were neglected. Since, a turbulent flow regime was identified due to the high Reynolds numbers [2], the standard k-ε model was applied for the computation of the turbulence. An in-depth description of the governing equations can be found in [2] or in [94]. In the model, the continuity equation is defined:

$$\nabla \cdot \vec{v} = 0 \tag{6-5}$$

Where ∇ [m^{-1}] is the gradient operator (nabla) and $\vec{v}$ [m s^{-1}] is the velocity vector. Next, the momentum conservation or Navier-Stokes equation is defined as:

$$\frac{\delta \vec{v}}{\delta t} + \vec{v}(\nabla \cdot \vec{v}) = \frac{\mu}{\rho_{air}} \nabla^2 \vec{v} + \frac{2\mu}{3\rho_{air}} (\nabla \cdot \vec{v}) - \nabla p \frac{1}{\rho_{air}} \tag{6-6}$$

Where ρ_{air} [kg m^{-3}] is the density of air; t [s] is time, the terms represent (in sequential order): accumulation of momentum; the change in momentum due to velocity; linear deformation stress; volumetric deformation stress (when compressible); pressure differences. For a 2-D model, the Navier-Stokes equation describes a coupled non-linear second-order partial differential equations [97]. Further definition of the standard k-epsilon model can be found in [2] or in [98]. For the near-wall treatments, the near-wall modeling approach is applied [2]. As a result, the near-wall region is completely solved, but requires additional cells near the boundaries. The species in the system are modeled with the species transport equations (based on mass conservation). For any arbitrary compound p, a species transport equation is defined per cell as:

$$\rho_{air} \frac{dY_P}{dt} = -\nabla \cdot (\rho_{air} Y_p \vec{v}) - \nabla \cdot \left(D_{p,air} \rho_{air} \nabla Y_p\right) + S_p \tag{6-7}$$

Where Y_p [-] is the mass fraction of pollutant p; $D_{p,air}$ [m^2 s^{-1}] is the diffusion coefficient of pollutant P in air ($2.88 \cdot 10^{-05}$ in FLUENT); and S_p [kg s^{-1}] is a source term for pollutant p. The terms represent (in sequential order): accumulation of mass; advection; diffusion; and a source term.

In the models, five compounds are defined: oxygen, nitrogen, water, nitric oxide, nitric dioxide. Sequentially, the mass fraction of nitrogen is calculated from the other mass fractions, using the mass fraction conservation, defined by [2]:

$$\gamma_{N_2} = 1 - \gamma_{NO} - \gamma_{NO_2} - \gamma_{H_2O} - \gamma_{O_2} \tag{6-8}$$

Finally, the temperature must be defined per cell to define the density of the air and vice versa a temperature is specified to define the density (ρ_{air}) per cell. While 300 K is the default value, 293.15 K is adopted, since the experiments [3] were conducted under similar condition. Accordingly, FLUENT calculated a ρ_{air} of 1.18775 kg m^{-3} at 293.15 K and 101324 Pa. An energy conservation equation is defined for the definition of the temperature [99]:

$$\delta T/\delta t + \vec{v}\nabla T = a\nabla^2 T \tag{6-9}$$

Where T [K] is temperature; and a [m^2 s^{-1}] is the thermal diffusivity. For the definition of the boundaries, first, the solid boundaries of the models are defined as *wall*, which implicate that the flux of any calculated variable is constrained to zero ($\nabla = 0$). Consecutively, the inlet is defined as *velocity inlet* for which the variables are defined in Table 19. As described in Table 19, the remaining boundary conditions are also reported. The average illuminance amount on the working plane expressed by $\bar{E}_{p\_workingplane}$ [lx] will be further explained in Section 6.2.6.

Table 19: Default inlet conditions of the CFD model and UDF, based on [2]. Where I_{in} [%] is the turbulent intensity at the inlet; and ℓ_{in} [m] is the characteristic length scale at the inlet.

Parameters				Constant values		
Variable	**Standard value**	**Varying value**	**Unit**	**Variable**	**Value**	**Unit**
u_{in}	$2.27202\cdot10^{-2}$	$2.27202\cdot10^{-2}$ - $1.81762\cdot10^{-1}$	m^3s^{-1}	ℓ_{in}	0.0168	m
I_{in}	4	2 - 16	%	γ_{H_2O}*	0.0073	-
$\bar{E}_{p\_workingplane}$	500	500 - 6501	lx	γ_{O_2}	0.1896	-
Y_{NO_in}	$9.92580\cdot10^{-7}$	$1.24072\cdot10^{-7}$ - $9.92580\cdot10^{-7}$	-	T	293.15	K
$Y_{NO_2\_in}$	$1.10287\cdot10^{-7}$	$1.37858\cdot10^{-8}$ - $1.10287\cdot10^{-7}$	-	-	-	-
D_{TiO_2}	0.02	0.02 - 0.5	-	-	-	-

*** ≈ 50% RH at 293.15 K and 101324 Pa**

The outlet boundary in the model is defined as *outflow*. As outlined in Figures 39 and 42 (see Section 6.2.1 or Section 6.2.3), the outlet was extended to create a full developed flow downstream so that there is no backflow conditions created at the outlet (e.g. recirculation). Also, the local mesh is refined, to avoid a coarse mesh and stretched cells which may influence the interpolation routine at the *outlet* boundary [100]. The initial conditions for the models are not specified within this report, since when a model is completely converged the initial conditions do not influence the final results.

To decrease simulation times, the flow variables were resolved first before the species equations and energy equation were solved. The flow parameters in the system were barely influenced NO_x dispersion. After two simulation runs where in which first the flow and then species and energy parameters were solved, a collective run was performed to compute the final results. The convergence of the models was observed with a monitoring point in the middle of the model from which the velocity magnitude and pollutant concentrations were monitored. When the values in this point and the scaled residuals stabilized to a horizontal line, it was assumed that the model was converged appropriately.

6.2.4. The radiance model setup

In this section, the construction of the radiance model of the room is explained. The primary objective of this radiance model is to predict the irradiance dispersion in a typical office room setting. In line with previous radiance modeling (Chapter 4), a three-dimensional monochromatic radiance model was created to estimate the irradiation on the photocatalyst-coated walls using a typical office lighting plan. The model was built and simulated with RADIANCE v.4.1. Because the CFD models are two-dimensional, the irradiance dispersion was approximated by an (nearly) infinitely stretched corridor, so that the depth would not affect the results significantly. The main dimensions and principles of the model are illustrated in Figure 43. The room is stretched by applying mirrors which create virtual projections.

Note that a different coordinate system was used for the radiance model. As a result, the coordinates used in the current section, Section 6.2.4 and Appendix 5 do not relate with the other coordinates used in this chapter.

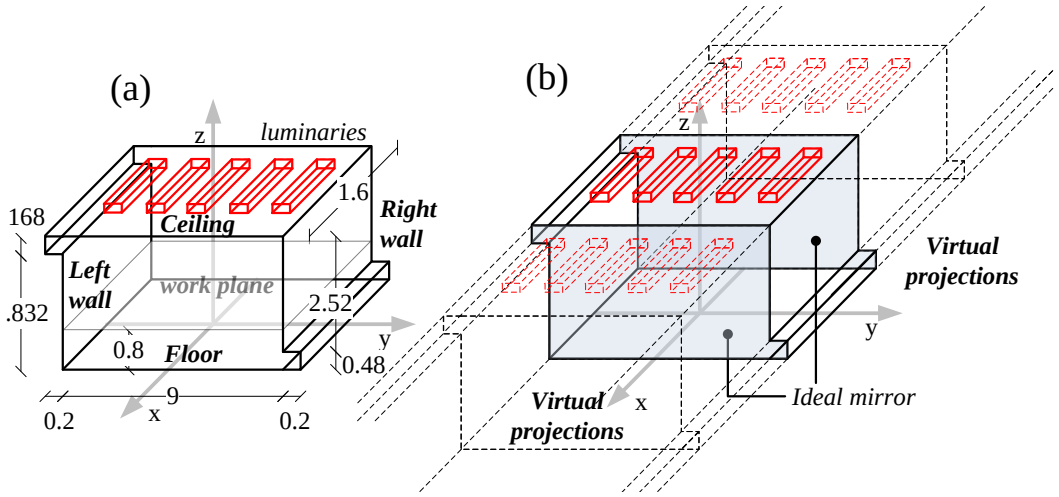

Figure 43: (a) The main dimensions and boundaries of the radiance model of the room; (b) The effect of ideal mirror material type: creating virtual projections.

The lighting plan is designed based on the illuminance required by the activities performed within each room (see Table 2). In turn, the average illuminance value recommended for general office activities of 500 lx [101] was applied as default setting. As was stated earlier in the introduction, a conversion factor was determined to convert the photometric units to radiometric units and vice versa, as discussed later on (Section 6.2.5). As can be seen in Figure 44a, the luminaires were centered over the y-axis to create a uniform distribution on the working plane. In order to guarantee a level of uniformity, the illuminance on the working plane was checked by an uniformity criterion, defined as:

$$E_{r\_average}/E_{r\_min} > 0.7 \qquad (6\text{-}10)$$

Where $E_{r\_average}$ and E_{r_min} [Wm^{-2}] are the average and minimum irradiance values found on the grid on the work plane. The uniformity criterion was passed, since an $E_{r\_average}/E_{r\_min} \approx 0.8 - 0.89$ was found through simulation.

Numerical data from the model was obtained using *rtrace* command for a number several of points plotted on various grids. These grids allowed the irradiance data on the working plane, floor, ceiling and walls to be converted to an irradiance distribution function, later discussed in Section 6.2.6.

The data points were distributed per section over three cross-sections, as illustrated in Figure 44b. The three cross-sections 1, 2 and 3 were located over respectively $x = 0$, $x = 0.4$ and $x = 0.8$. The data points on the work plane were located on $z = 0.8$ from $y = -4$ to $y = 4$ with an interval of 1 generating 9 data points for the grid on the working plane. In turn, both the data points on the floor and the ceiling were located from $y = -4.5$ to $y = 4.5$ with an interval of 0.25 giving 19 data points in total to the grids on $z = 0$ and on $z = 3$ respectively. Lastly, the data points on the back and front wall are located from $z = 0$ to $z = 3$ with an interval of 0.125 m, giving 25 data points for a grid per wall. A total of 291 data points were generated during the simulation. In order to prevent placement of data points into a boundary and, all data points adjacent to a boundary were moved away from the boundary with 0.01 mm.

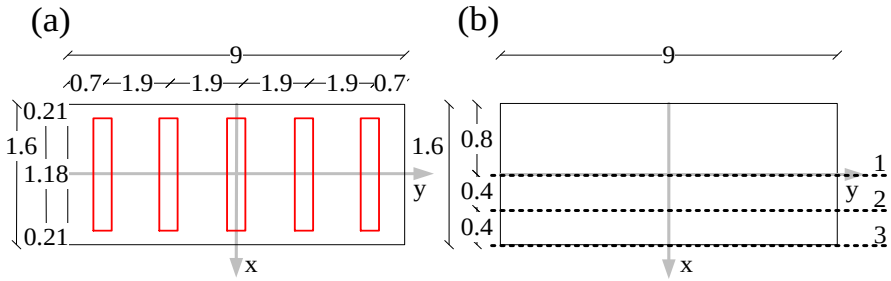

Figure 44: (a) The position of the luminaires; (b) The three cross-sections in which the grids are applied. (All dimensions are given in m)

In turn, the specifications of the luminaires and light source model in the radiance model are based on the luminaire and light source model design from Chapter 4. While the main dimensions were maintained, the length of the luminares and light source was doubled to fit the specifications of a typical fluorescent light source, as illustrated in the cross-sections of Figure 45. Furthermore, the applied materials in the luminaire are adapted from the previous modeling (Section 4.2.3).

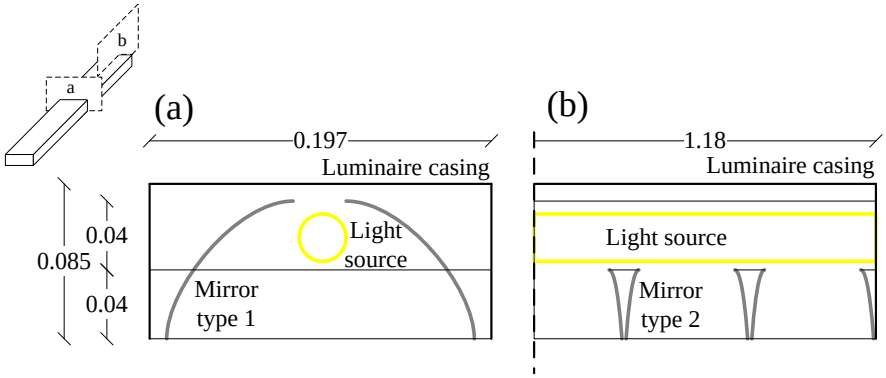

Figure 45: The dimensions of the luminaires which are in the radiance model of the benchmark room model. (All dimensions are given in m)

In turn, the ideal mirror material in the room model was defined in RADIANCE by:

```
# ideal mirror
void mirror idealmirror_mat
0
0
3 σR σG σB
```

Where σ_R, σ_G and σ_B [-] are the reflection coefficient for the components red, green and blue.

Consecutively, the remaining opaque materials in the room model are defined in RADIANCE by:

```
# General template for opaque materials
void metal [name]_mat
0
0
5 σR σG σB S R
```

Where S [-] is the specular component; and R [-] is the roughness coefficient. In line with the previous simulation (Chapter 4), both the reflection coefficient and specular component (S) were assumed to be equal for all wavelengths between 400-570 nm and are therefore calculated as an arithmetic average over this interval ($\sigma_R = \sigma_G = \sigma_B = \sigma_{400-570}$). In Figure 46, a simplified overview of the room and primary materials is illustrated, for which in Table 20, along with the other materials, the input parameters are listed.

Table 20: The input parameters of the opaque materials.

Material	Reflection coefficient ($\sigma_{400-570}$ [-])	Specular component (S [-])
Black paper	0.044	0.01
Luminaire casing	0.713	0.03
Mirror	0.845	0.85
Floor	0.2	0.00
Photocatalyst -coated wall	0.883	0.01

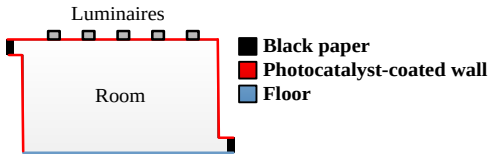

Figure 46: Simplified cross-section of the room and its primary materials.

All numerical data was obtained via the settings listed in Table 21, which were adapted from the first modeling study (Section 4.2.5). However, the direct relay parameter was obtained via a sensitivity analysis, reported in Section 6.3.1. Additionally, for the remaining rendering parameters, the default values of RADIANCE were adapted.

Table 21: The standard settings of the rendering parameters of the radiance model employed in the third modeling study.

-ab	-dj	-ds	-dr	-aa	-ar	-ad	-as
5	1.0	0.05	4	0.1	256	1024	64

6.2.5. Conversion between radiometric and photometric units

In this section, the conversion factor is explained. The conversion factor is required to convert photometric data to radiometric data and vice versa. While the photometric measure of light is the perceived brightness by the human eye, the radiometric measure expresses the radiant energy. Since radiance model is monochromatic, the required photometric values are linear related with radiometric values by the factor β [lmW^{-1}]. Along the lines of [1], it is assumed that emitted spectrum of the light source remains stable when dimmed. Nevertheless, the emitted spectrum can be influenced by e.g. aging, power output, and temperature. This, however, remained outside the scope of this work.

Based on equation (2-35) and equation (2-36), defined in Section 2.5, the conversion factor for the total radiant flux ($\Phi_{r;400-570}$ [W]) is converted to the total luminous flux (Φ_p [lm]) by:

$$\Phi_p = K\vartheta_l \frac{\Phi_{r;400-570}}{\varepsilon_l} = \beta\Phi_{r;400-570} \tag{6-11}$$

Where K [683 lmW^{-1}] the constant for photopic region; ϑ_l [%] is the luminous efficiency of the light source; and ε_l [%] is the percentage flux of the light source which is emitted between the 400-570 nm. Both ϑ_l and ε_l were obtained from emission experiment on the PHILIPS Master TL-D 18 W/854 light source, reported in Section 3.5. Consequently, a ϑ_l 34.5% and a ε_l of 63.2% were obtained for the light sources. In turn, a conversion factor (β [lmW^{-1}]) of 149.11 lmW^{-1} is computed.

6.2.6. **Irradiance data integration into FLUENT**

Unfortunately, RADIANCE operates on a Unix-based OS, while FLUENT runs on Windows. Therefore, a direct integration of the two programs is difficult. Therefore, the irradiance date was calculated first, before the CFD models were simulated. As a result, the irradiance data from RADIANCE has to be imported manually into the UDF's, used by FLUENT.

In order to integrate the irradiance data into a CFD model, a continuous function needed to be formulated, generally defined as $f_E(x,y)$[Wm^{-2}] as function of spatial coordinates x and y. Because the CFD models are two-dimensional, the irradiance data from RADIANCE could directly be converted to a function. However, during the function development in the UDF file, two methods were considered, using the C-scripting language. First of all, an interpolation function was considered in order to estimate intermediate irradiance data points. However, this would pose a substantial amount of programming work. Alternatively, a curve fitting routine was employed to convert the data points per section to a continuous function using either Matlab or Excel. The sections were divided into the working plane, floor, ceiling, left and right wall.

While Excel can derive 6th degree polynomial fit, Matlab can fit a function up to a 10th degree polynomial. It was observed that the optimization method between the programs differed. During the curve fitting routine, Excel minimized the Coefficient of Determination, whereas Matlab minimizes the Norm of Residuals (r^2 [-]). Apparently both indicators can be used as a fitting a function to a set of data points. However, there is a qualitative difference, but this relationship was further studied. Eventually, Matlab was used, because a 10th degree polynomial fit was required to ensure sufficient accuracy. The equation of the 10th degree polynomial is defined as:

$$f_{E;s}(p) = c_1p^{10} + c_2p^9 + c_3p^8 + c_4p^7 + c_5p^6 + c_6p^5 + c_7p^4 + c_8p^3 + c_9p^2 + c_{10}p + c_{11} \tag{6-12}$$

Where $f_{E;s}(p)$ [Wm^{-2}] is the irradiance profile function for position p [m] for wall section s, either defined by the x ($p = x$) or the y ($p = y$) coordinate; and c_i [$Wm^{-(13-i)}$] are the empirical constants corresponding to the wall section.

Consecutively, the empirical constants are defined. For the position p, the ceiling and floor are defined by the x-position, while the left wall and right wall are defined by the y-position. The constants for each section are defined in Table 22, together with the goodness of fit indicators, using both the Coefficient of Determination and Norm of Residuals.

Table 22: The constants for the polynomial; defined up to four decimal places.

Constants	Floor	Ceiling	Left wall	Right wall
c_1[Wm^{-12}]	0	0	-0.4210	-0.5811
c_2 [Wm^{-11}]	0	10^{-4}	6.2174	8.6068
c_3 [Wm^{-10}]	-0.0014	-0.0022	-38.4597	-53.6239
c_4 [Wm^{-9}]	0.0118	0.02459	129.4396	182.9030
c_5 [Wm^{-8}]	-0.0481	-0.1716	-257.4859	-372.3908
c_6 [Wm^{-7}]	0.0360	0.7754	307.0265	462.7509
c_7 [Wm^{-6}]	0.4664	-2.2763	-210.4259	-343.7242
c_8 [Wm^{-5}]	-1.8779	4.2372	71.5702	141.7707
c_9 [Wm^{-4}]	2.8778	-4.6918	-5.4345	-26.6434
c_{10} [Wm^{-3}]	-1.4830	2.6153	-2.2292	0.8492
c_{11} [Wm^{-2}]	2.9822	0.3841	1.7202	1.5811
Norm of residuals	0.1174	0.0103	0.4547	0.4295
r^2	0.9949	0.9996	0.9513	0.9555

Based on equation (6-12) and Table 22, the irradiance distribution for the default illuminance value (500 lx) is illustrated in Figure 47.

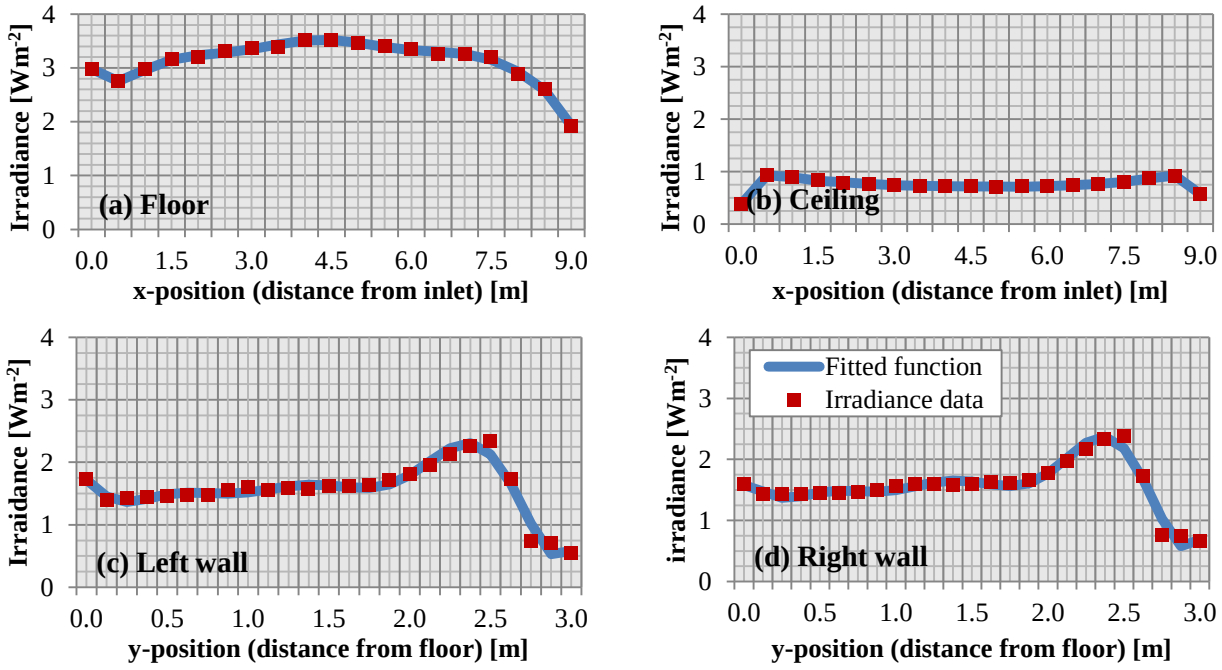

Figure 47: The irradiance distribution data for general office activities ($E_{p\_workplane}$ =500 lx) given by RADIANCE fitted by a continuous function using Matlab, per wall section.

Since the four continuous functions are provided, the script for the UDF file is defined. The predefined macro (*DEFINE_SOURCE*), used in [2], is adapted as the starting point for the UDF. The variable *E* defined in the UDF, is substituted by irradiance profile function or $f_E(x,y)$, written in a C-script to defined the four irradiance profiles along the four boundary sections, defined by:

```
/* E-profile function */
real x[ND_ND]; /* the position vector [x,y] */
real E; /* the continuous function for E */
C_CENTROID(x,c,t);

if (x[1] >= 2.999 || E <= 0)                    /* ceiling */
E = f_E_ceiling(x) · (Ē_p_workplane / 500)
else if (x[1] <= 0.001 || E <= 0)               /* floor */
E = f_E_floor(x) · (Ē_p_workplane / 500)                              (6-13)
else if ((x[0]) <= 0.001|| E <= 0)              /* left wall */
E = f_E_left_wall(y) · (Ē_p_workplane / 500)
else if ((x[0]) >= 8.999 || E <= 0)             /* right wall */
E = f_E_right_wall(y) · (Ē_p_workplane / 500)

else
E = 0;                                          /* other */
```

Where, printed in red, $f_{E\_ceiling}(x)$, $f_{E\_floor}(x)$, $f_{E\_left\_wall}(y)$ and $f_{E\_right\_wall}(y)$ [Wm^{-2}] are the continuous functions for the four sections with the corresponding coordinate defined by equation (6-12) and Table 22; and $\bar{E}_{p\_workplane}$ [lx] is average illuminance on the working plane in the model (default = 500 lx). Note that, in order to facilitate explanation, the notation in the appendix can differ somewhat from methodology used in this section. In Appendix 6, the complete UDF file can be found.

6.2.7. **Definition of performance indicator**

To quantify the effectiveness of PCO, a performance indicator is applied to quantify the contaminant removal efficiency. The performance indicator is adapted from [2] and defines the NO_x conversion rate with:

$$NO_{x;con} = \frac{C_{NO_x;in} - C_{NO_x;out}}{C_{NO_x;in}} \cdot 100 \qquad (6\text{-}14)$$

Where $NO_{x;con}$ [%] is the removal rate index of NO_x; $C_{NO_x;in}$ and $C_{NO_x;out}$ [mol m^{-3}] are the average ingoing and outgoing concentrations of NO_x in and out of the model respectively.

6.2.8. **Definition of age of air**

In this section, the implementation of the concept of the age of air and two alternative methods for flow characterization are explained. In a steady state calculation, the implementation method of the age of air parameter expresses the local residence time of the local air in the model. This allows the numerical quantification of the stagnation of air in the model. Furthermore, two additional indicators, including the air change efficiency and the degree of uniformity may be calculated from the age of air which may be used as a characterization parameter for the flow in the room.

In FLUENT, the age of air is calculated by an UDF that is incorporated into an User Defined Scalar (UDS) transport (species) equation, generally defined as [102]:

$$\rho_{air}\frac{\delta\phi_k}{\delta t}+\frac{\delta}{\delta x_i}\left(v_i\rho_{air}\phi_k-D_{UDS}\frac{\delta\phi_k}{\delta x_i}\right)=S_{\phi_k}, k=1,2,\dots,n_{scalar} \quad (6\text{-}15)$$

Were ϕ_k [-] is the UDS for k of the n_{scalar} User Defined Scalar (UDS) transport equations; v_i [m s^{-2}] is the local velocity; D_{UDS} [kg $m^{-1}s^{-1}$] is the UDS diffusion coefficient; and S_{ϕ_k} [kg $m^{-3}s^{-1}$] is the source term. Furthermore, the terms in equation (6-15) are defined in listed order: accumulation + convection - diffusion = source. The source term (S_{ϕ_1}) is set to 1, for all volumes (cells) containing fluid, in the model. Additionally, the boundaries, except for the inlet, have a specified flux ($\rho_{air}\frac{\delta\phi_k}{\delta t}$) of 0 kg $m^{-3}s^{-1}$, except for the inlet which has a boundary condition of ϕ_k= 0. In addition, D_k is defined by the UDF, defined as:

$$D_{UDS}=\rho_{air}D_m+\nu/Sc \quad (6\text{-}16)$$

Where D_m ($2.88\cdot10^{-5}$ [m^2s^{-1}]) is the mass diffusivity of air through air; ν ([$m^{-2}s^{-1}$]) kinematic viscosity of air ($=\mu/\rho_{air}$); and Sc (0.7 [-]) is the Schmidt number, defined as the ratio of momentum diffusivity (viscosity) and mass diffusivity. The UDF is enclosed in Appendix 6. After processing (simulation), during the post-processing of the model, a Custom Field Function (CFF) is applied to calculate the age of air (τ_a[s]), according to:

$$\tau_a=Density*uds\_0\_scalar/SOURCE \quad (6\text{-}17)$$

Where $Density$ is an Operand Field Function, predefined by FLUENT, which return the density [kg m^{-3}] of the fluid per cell; uds_0_scalar returns the local ϕ_k [-] per cell; and $SOURCE$ is the value given to S_{ϕ_1} [kg $m^{-3}s^{-1}$]. Now, first indicator, named as the air change efficiency (ε_a [%]), the ratio between the shorted air change time and the actual air change time, can be calculated with [103]:

$$\varepsilon_a=\frac{\tau_n}{\tau_r}\cdot100=\frac{\tau_n}{2\bar{\tau}}\cdot100 \quad (6\text{-}18)$$

Where τ_n, τ_r and $\bar{\tau}$ [s] are the nominal (alias the residence time: $\tau_n=V/Q$), actual and average age of air respectively. The τ_n can be calculate in FLUENT by taking the vertex average value of τ_a over the outlet boundary and $\bar{\tau}$ is computed by taking the average of τ_a over the cells of the whole (fluid) volume. τ_n is related with the air change rate per hour (ACH), by:

$$ACH=\frac{3600}{\tau_n} \quad (6\text{-}19)$$

In turn, the second indicator, the degree of uniformity, defines the amount of uniformity in a model. In reactor chemistry, quantization of mixing is investigated for the design of chemical reactors, for instance in continuous flow stirred tank reactors, using the age of air concept [104]. In short, the degree of uniformity (M_u [-]) for a selected volume (V [m^3]) can be obtained by the normalized standard deviation of the age of air, defined as [65]:

$$M_u=\frac{\sqrt{\int_V(\tau_a-\bar{\tau})^2\frac{1}{V}dV}}{\bar{\tau}} \quad (6\text{-}20)$$

Where τ_a [s] is the local age of air. When the two indicators are calculated for ideal flows, an air change efficiency of 100% is obtained for an ideal plug flow, whereas an ideal mixed flow yields a degree of uniformity of 0.

6.3. Verification and validation

6.3.1. Rendering parameter sensitivity and modeling errors in the radiance model

Before the radiance model was built, the sensitivity analysis of the direct relay parameter (explained in Section A-1.1) was conducted, as illustrated in Figure 48. Eventually, a $-dr$ value of 4 was selected for simulation. Furthermore, while the model is an approximation of an infinite long hallway, the actual model was not infinite long which left a part of the space un-modeled. As a result, an error was introduced which had to be estimated. Therefore, four hemispherical fisheye views were rendered, to assess a quantity of the un-modeled surfaces with respect to the modeled surfaces, as viewed in Figure 49. In view A and C, 3.80% of the un-modeled space viewable while view B and D perceive 1.58% of the viewable space as un-modeled. In total, 2.7% is not perceived, meaning that obtained irradiance is 0.97% lower as that of an infinite room which is acceptable error.

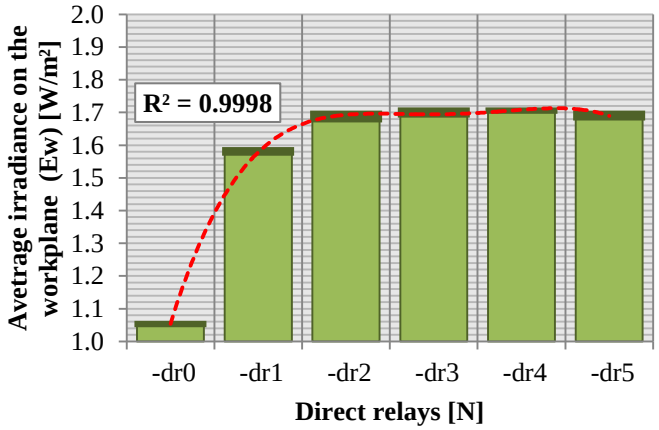

Figure 48: The average irradiance and uncertainty interval on the sampling grid on the working plane per 6 simulations for different settings for the direct relays rendering parameter, using L_i of 52 $Wm^{-2}sr^{-1}$.

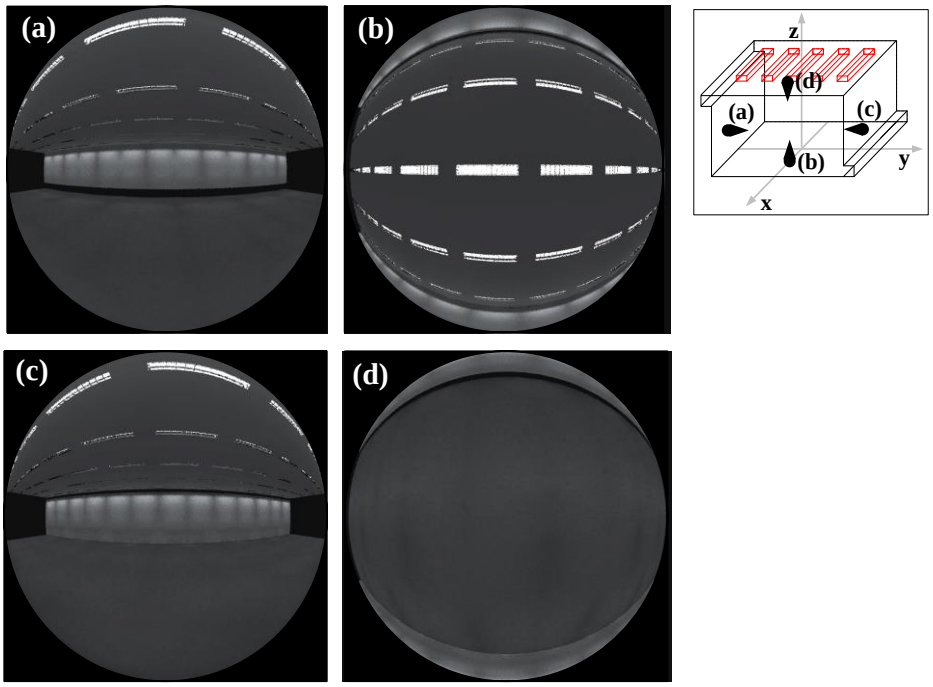

Figure 49: The four hemispherical fisheye renders on the at the coordinates: a:(-0.4; -4.5; 1.5); b (-0.4; 0; 0); c (-0.4; 4.5; 1.5); d (-0.4; 0;3)

6.3.2. The CFD models: Discretization error estimation

Before the final results were obtained, the discretization error was estimated by performing a grid independence test (GCI), similar to [2]. The GCI is based upon a grid refinement error estimator derived from the theory of generalized Richardson Extrapolation and can be defined for a finer or coarser grid and multiple grids simultaneously. The GCI is a general parameter which can be applied to any solution variable [105]. For comparison with a finer grid, the GCI is defined as [90, 106]:

$$GCI_{i;i+1} = F_s \frac{|f_i - f_{i+1}|}{f_i(r^p - 1)} \tag{6-21}$$

Where $GCI(u)$ [-] is the relative error of the grid independence test; f_i and f_{i+1} [-] are the extrapolated variables for the default and finer grid respectively; r [-] is the refinement factor or the ratio between amount of cells in the fine and coarse grid respectively; F_s [-] is a safety factor which is 1.25, when applying three grids per model; and p [-] is the order of convergence, for which a theoretical value of 2 should be adapted [90], similar to [2]. However, [63] reported on certain circumstances in which p can be lower than the theoretical value, thus increasing GCI. For instance, the order of convergence can vary because of grid stretching, grid quality, non-linearity's in the solution, turbulence modeling and so on [90]. According to [91], the order of convergence can be calculated when three grids (*n=3*) are constructed for a model, by:

$$p = \frac{ln(\epsilon_{21}/\epsilon_{32})}{ln(r)} \tag{6-22}$$

Where:

$$\epsilon_{i+i;i} = f_{i+1} - f_i \tag{6-23}$$

Additionally, the refinement factor, r, is defined as:

$$r = \left(\frac{c_{i+1}}{c_i}\right)^{0.5} \tag{6-24}$$

Where c_{i+1} and c_i [-] are the amount of cells in the fine and default grid respectively. To evaluate the extrapolated variables, the convergence conditions of the model need to be determined [106]. The convergence conditions are: monotonic convergence ($0 < R < 1$), oscillatory convergence ($R < 0$) or divergence ($R > 1$), for which R is the convergence ration and is determined by [106]:

$$R = \epsilon_{32}/\epsilon_{21} \tag{6-25}$$

Per model (case), three grids were constructed with a refinement factor of 2 between grids. The grids were refined from 1 to 3 respectively, corresponding to i.

The GCI is calculated using the velocity magnitude integral over the total volume, as reported in Table 23. It is observed that for cases 1 and 5, the grids are converged oscillating, while grids for the other cases converged monotonic with a small GCI, below outlying the frequently acceptable GCI error margin of 5% [107]. The degree of oscillatory convergence can be estimated by increasing the amount of grids generated to n > 3 [108]. However, this option was not checked. As an alternative it was assumed, since cases 1 and 5 are comparable with the other cases, for which minimal GCI were round, the GCI of cases 1 and 5 are expected to be well within range of 5%. Still, if the grids of a case would divergence, then the GCI cannot be estimated, as a result a new mesh is required [108].

Table 23: The grid comparison between cases and GCI, using the velocity magnitude integral, calculated using the standard conditions and a v_x of 0.455 m s^{-1}.

Case	1	2	3	4	5
Default grid (i = 1) [m s^{-1} m^3]	2.483636	2.396824	2.345499	2.524724	2.778193
Fine grid (i = 2) [m s^{-1} m^3]	2.486673	2.391469	2.347609	2.526779	2.778559
Finer grid (i = 3) [m s^{-1} m^3]	2.485996	2.390895	2.348497	2.526993	2.778533
r	1.414889	1.414283	1.41424129	1.414413	1.414274
e_{21}	0.003037	-0.00536	0.00211	0.002055	0.000366
e_{32}	-0.00068	-0.00057	0.000888	0.000214	-0.000026
R [-]	-0.22292	0.10719	0.42085308	0.104136	-0.07104
p [-]	-	6.44261	2.49708155	6.524257	-
F_s [-]	1.25	1.25	1.25	1.25	1.25
GCI_{21} [%]	-	0.034%	0.082%	0.012%	-
GCI_{32} [%]	-	0.004%	0.034%	0.001%	-

6.3.3. Validation of the CFD benchmark model with experimental data

Similar to [2], the case 1, the benchmark model is compared with the measured data from [4]. For comparison, the standard conditions are adapted (Table 19). However, in line with [2], the default velocity magnitude of 0.455 m s^{-1} (≈ 10 ACH) is applied. The x-velocity magnitude is compared over 4 lines, as illustrated in Figure 50. Both measurement and simulation are in agreement.

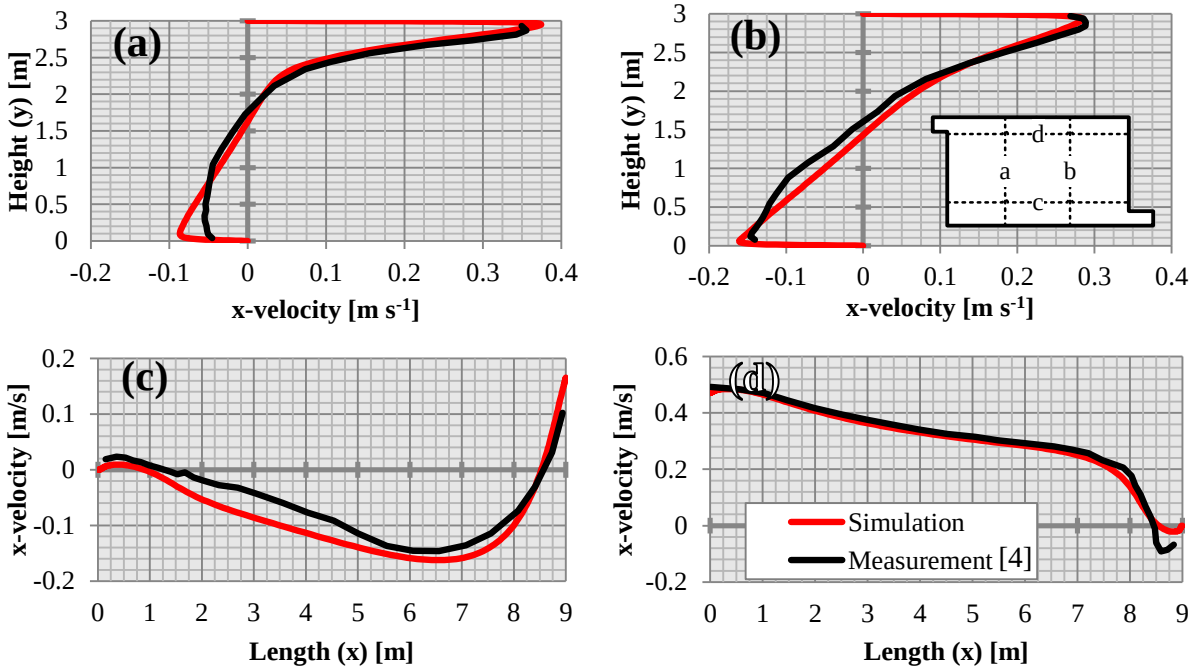

Figure 50: Both measurement [4] and simulation are compared for validation of the benchmark model. The x-velocity profiles over 4 lines are taken: (a) on x = 3 m; (b) on x = 6 m; (c) on y = 0.084 m; (d) on y = 2.916 m.

6.3.4. Verification of the kinetic model implementation approach for CFD

In this section, the newly suggested implementation method, previously discussed in Section 2.7, is verified. This is done by performing several simulations of case 1 using standard conditions, with only the floor section activated while changing the section height, as illustrated in Figure 51. For the different section heights, additional zoning was required. Therefore a marginal re-distribution of the cells near the floor was implemented and the total number of cells changed minimally (23497 cells). Additionally, to accommodate the iteration speed of the simulations, an uniform irradiance distribution of 10 Wm^{-2} and a D_{TiO2} of 0.01 is applied. Sequentially, for several of the simulations, the UDF function, found in Appendix 6, is adapted to match the section height according to the theory described in Section 2.7. However, for the remaining simulations, UDF remains unchanged. The section height corresponds to the Δy in equation (2-54) that expresses the new implementation method.

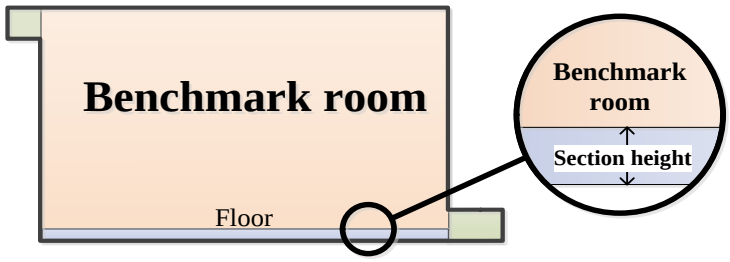

Figure 51: The principle of the verification of the kinetic model implementation approach by using the first case.

As can be seen in Figures 52a and 52b, the mass flow due to photocatalytic reaction for respectively NO and NO_2 remain unchanged when then the height of the cells is increased and the UDF is adapted. However, when the UDF function remains unchanged, the total mass flow does change when the section height is altered. Because of this, it is concluded that section height should be included in the UDF to counter the effect of varying section heights. Clearly, if the section height is made excessively high in a model, this will introduce a physical modeling error [63] during simulation.

However, the observed difference in NO mass flow between the models with the adapted UDF applied is insignificant, as between respectively 1 mm and 2 mm and between 2 mm and 3 mm section height a relative difference of $4.6 \cdot 10^{-4}$% and $5.1 \cdot 10^{-5}$% was observed.

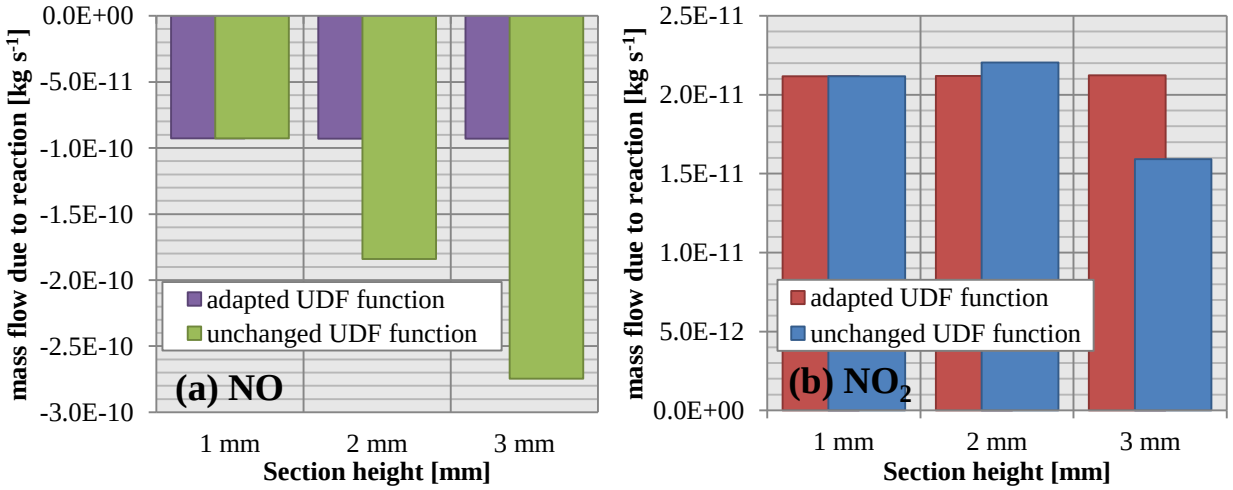

Figure 52: The mass flow due to photocatalytic reaction for respectively (a) NO and (b) NO_2, for case 1, while the floor section is activated.

6.4. Results

In this section, the simulation results are reported. In Section 6.4.1, the standard benchmark room is recalculated to provide a starting point, based on the new implementation method of the NO_x kinetic model discussed previously in Section 2.7. Then, in Section 6.4.2, the effects of the different activities on the irradiance amount and on conversion of NO_x are demonstrated using the benchmark model. Following by Section 6.4.3, in which the effects of different inlet locations and different phototocatalytic active walls sections on the conversion of of NO_x are reported. The age of air used to illustrate the stagnation of air, and calculate the air change efficiency and the degree of uniformity indicators. Following by Section 6.4.4, in which the effect of the different pollution types is studied for several ACH using the $NO_{x_{con}}$ performance indicator. Consequently, an alternative approach for the photocatalyst performance assessment is suggested. In Section 6.4.5, the effect of additional turbulence at the inlet is analyzed, using the benchmark model. In addition, in Section 6.4.6, the photocatalytic activity in both the CFD benchmark room and the ideal mixed flow model from the previous modeling study (Chapter 5) are simulated and compared for different catalyst dosage. Finally, in Section 6.4.7 the effect of various NO_x mass flow compositions is considered.

6.4.1. The benchmark room

As a starting point, the base case of [2] is recalculated using the standard conditions (Table 19) and the uniform irradiance of 10 Wm^{-2}, while applying the new implementing method for the kinetic model (Section 2.7). Consequently, a $NO_{x_{con}}$ of 6.6% was observed which was higher as reported in [2]. Furthermore, as demonstrated in Figure 53b by the age of air parameter, the flow stagnates in both the lower left and upper rights corner in the similar regions were high photocatalytic reaction occur. Parallel to the stagnation, high photocatalytic activity occurs in the regions, as concluded from Figure 53c and Figure 53d. Similar observations were made by [2], which suggested that the stagnation of air promoted the local conversion of NO_x. Later, in Section 6.4.3, it will be demonstrated that the effect of stagnation is complex. Additionally, in Figure 53d it is suggested that the generations of the potential dangerous intermediate NO_2 only increased local concentrations near the photocatalyst-coated walls, while the concentrations in the remaining room are lower. This seems to be a beneficial effect, since most of the occupants reside primarily in the central space of the room. The first simulation of the benchmark room provides a first understanding of the PCO mechanisms. Furthermore, additional insights are reported in the following sections.

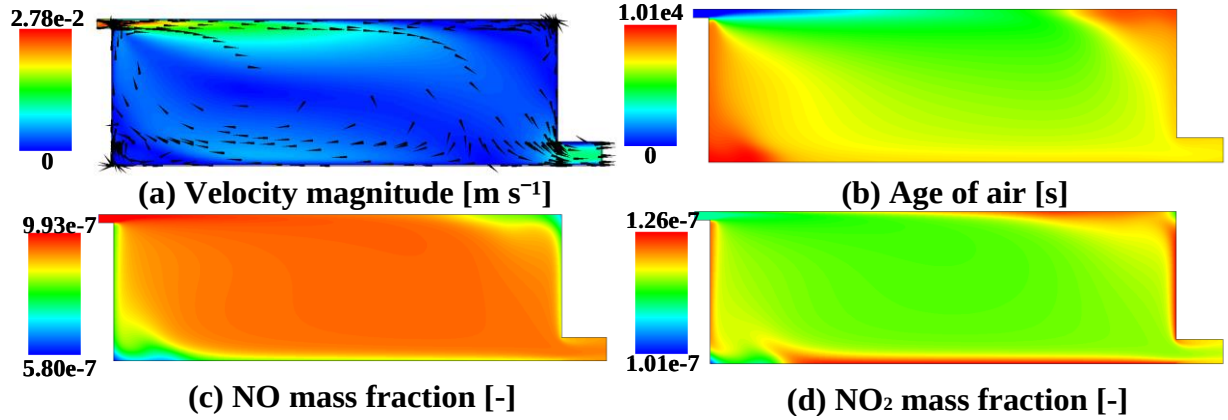

Figure 53: The (a) velocity magnitude and direction, (b) Age of air, (c) NO mass fraction and (D) NO_2 mass fraction in the benchmark room with standard conditions and an uniform irradiance dispersion of 10 Wm^{-2}.

6.4.2. The effect of required illuminance for human activity

Following on the previous simulation, the benchmark model is extended by introducing the irradiance distribution functions (Section 6.2.6) into the CFD model and adjusting the irradiance amount based on the general indoor activities (Section 2.5.2). In Table 24, the required (average) illuminance on the working plan, $\bar{E}_{p\_workplane}$, is reported corresponding IES illuminance category for generic indoor activities. In turn, the average irradiance per wall section (i.e. the floor; $\bar{E}_{r\_floor}$, ceiling; $\bar{E}_{r\_ceiling}$, walls; $\bar{E}_{r\_walls}$) is computed. Subsequently, three simulations performed per one of the categories illuminance values. From the simulations, the NO_x conversion is calculated, as demonstrated in Figure 54. The relation between average illuminance on the working plane and the conversion of NO_x, $NO_{x_{con}}$, is plotted. A logarithmic relationship is found between the conversion of NO_x and the average illuminance. This implies that an increase in the illuminance values at lower levels has a more significant impact on the NO_x conversion as increase at higher levels.

Table 24: The average irradiance of 10 Wm^{-2} for a boundary linked with an IES illuminance category and radiance of the light sources, based on Table 2.

Variable	Unit	IES Illuminance Category - For Generic Indoor Activities		
		D	F	G
$\bar{E}_{p\_workplane}$	**lx**	**500**	**1000**	**2000**
L_l	W m^{-2} sr^{-1}	103.15	206.31	412.62
$\bar{E}_{r\_floor}$	W m^{-2}	3.13	6.26	12.53
$\bar{E}_{r\_ceiling}$	W m^{-2}	0.75	1.51	3.01
$\bar{E}_{r\_walls}$	W m^{-2}	1.56	3.12	6.25

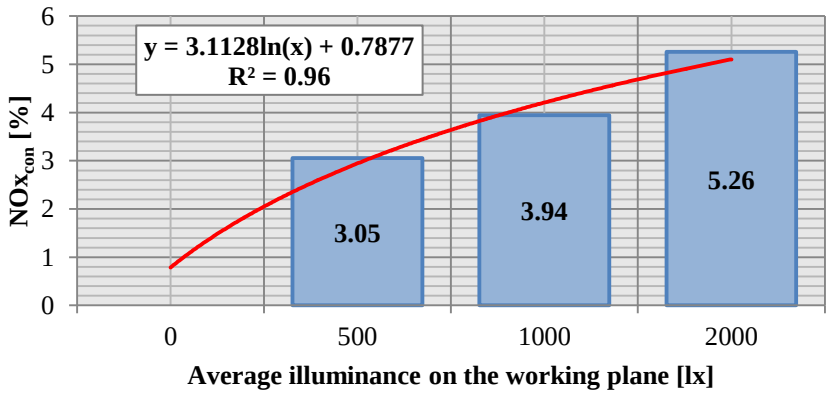

Figure 54: The NOx_{con} in case 1 as function of average illuminance on the working plane.

6.4.3. The effect of different inlet locations and active walls sections

While the previous results involved only the effect of irradiance, in this section the effect of flow is also included. This is done by alternating the inlet locations and the activation of the photocatalyst-coated wall sections per simulation. First, the results of all the five cases with different inlet locations are compared using the irradiance distribution with the default illumination (500 lx) and the standard conditions (Table 19), as reported in Figure 55. Both performance indicators NO_{con} and $NO_{x_{con}}$ are calculated per case. It is observed that case 1 yields a significant higher conversion in comparison with the other cases.

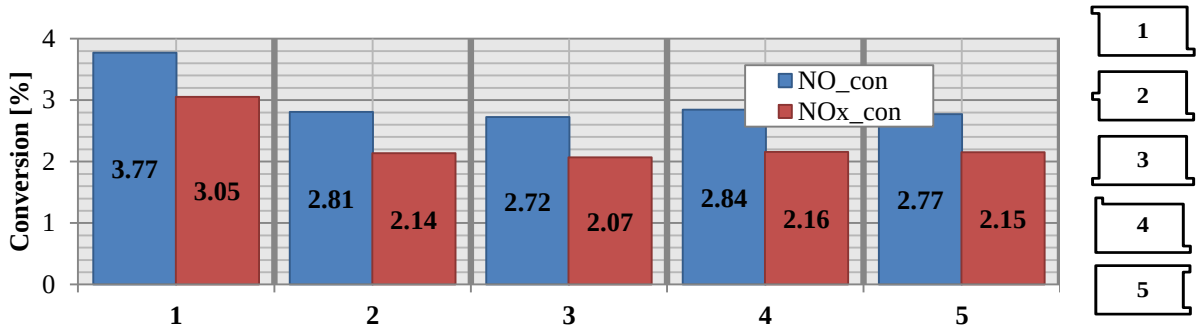

Figure 55: The NO_{con} and $NO_{x;con}$ calculated for the standard conditions per case with all wall sections activated.

Subsequently, the individual wall sections are photocatalytically-activated, as demonstrated in Figure 56. Furthermore, the degree of uniformity and air change efficiency indicators are calculated and reported in Table 25.

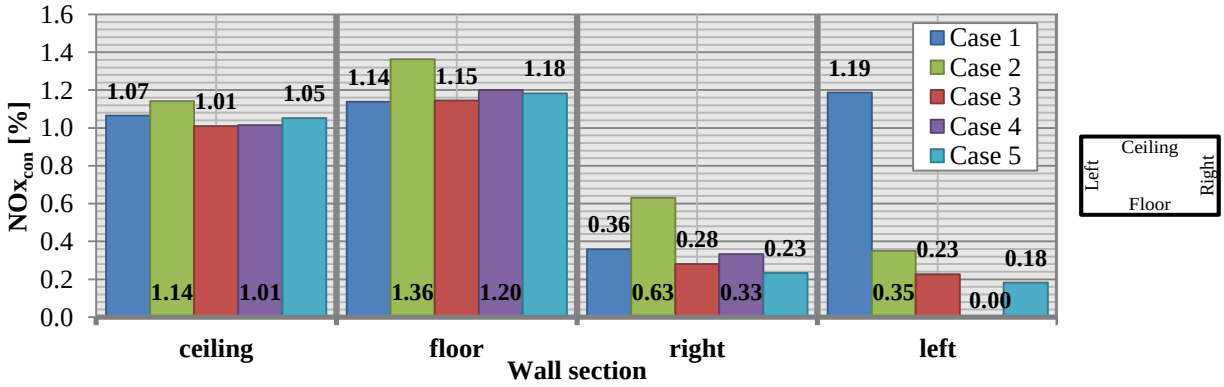

Figure 56: The NO_{con} [%] calculated for the standard conditions per case broken down per activated single wall section.

Table 25: The air change efficiency and the degree of uniformity reported per case using standard conditions. See Section 6.2.8 for explanation of these indicators.

Case	1	2	3	4	5
Air change efficiency (ε_a[-])	56%	83%	49%	57%	39%
Degree of uniformity (M_u [-])	0.195	0.526	0.209	0.252	0.248

Both the data from Figures 55 and 56 suggest that the flow may affect the photocatalytic degradation of NO_x extensively. However, characterization of the flow in Table 25 does not provide sufficient explanation. Therefore, several variants need to be studied individually by analyzing the mass fractions, age of air and the velocity magnitude.

First of all, the left and right walls of case 1 are plotted in Figure 57. Figure 57 indicates that the role of stagnation can differ considerably per wall section, as the conversion between the walls diverges substantial with respectively 0.12% and 0.4% for the left and right wall. Furthermore, the irradiance distribution function (Section 6.2.6) appears to influence the degree in which the stagnation increases local photocatalytic activity. The stagnation at the left wall in case 1 seems to be the primary reason for the overall raise the NO_x conversion in Figure 55. In Figure 55, the NO_x conversion in case 1 is roughly 0.9% higher than the remaining cases.

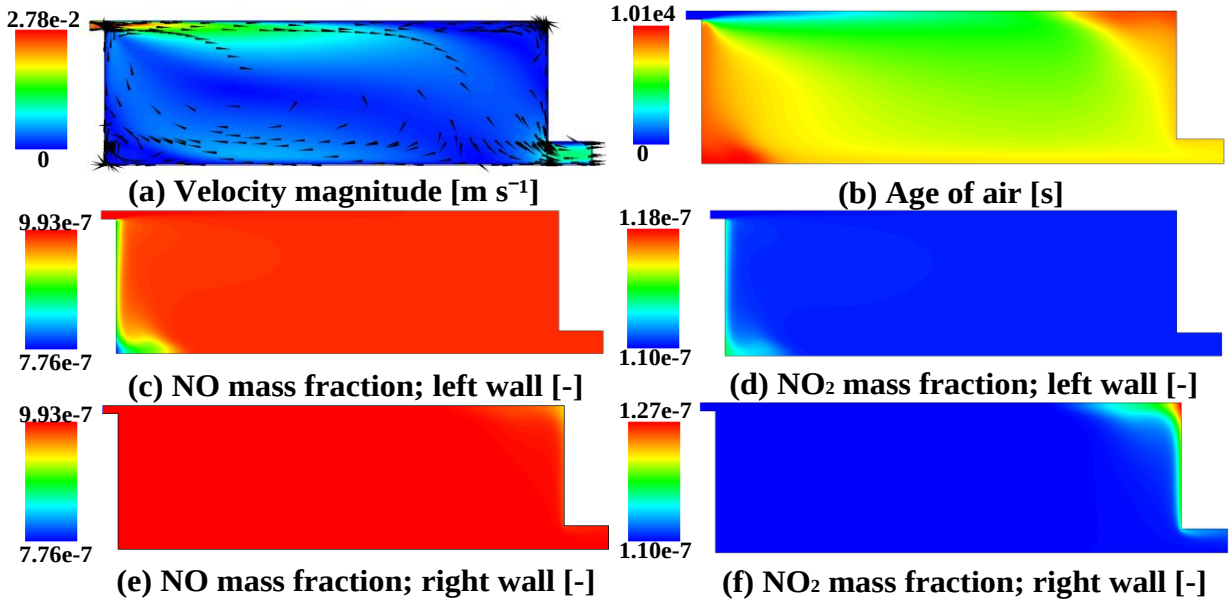

Figure 57: The NOx mass fractions, velocity magnitude (a) and age of air (b) for case 1 while only the left (c) (d) or right wall section (e) (f) is activated for photocatalytic activity.

The second case is also studied in more detail, since a high air change efficiency was found (Table 25). Controversially, the right wall provides a larger NO_x conversion as the left wall (left wall: 0.35%, right wall: 0.63%). This may be clarified by higher velocity magnitudes near the left with respect to the right wall; while the right wall is located near the inlet jet, the left wall is located near the stagnation zone as is illustrated in Figure 58a and Figure 58b. Furthermore, it is observed from Figure 58, the flow near the floor is not subjected to major stagnation but still provides the highest conversion compared to the floors in the other cases.

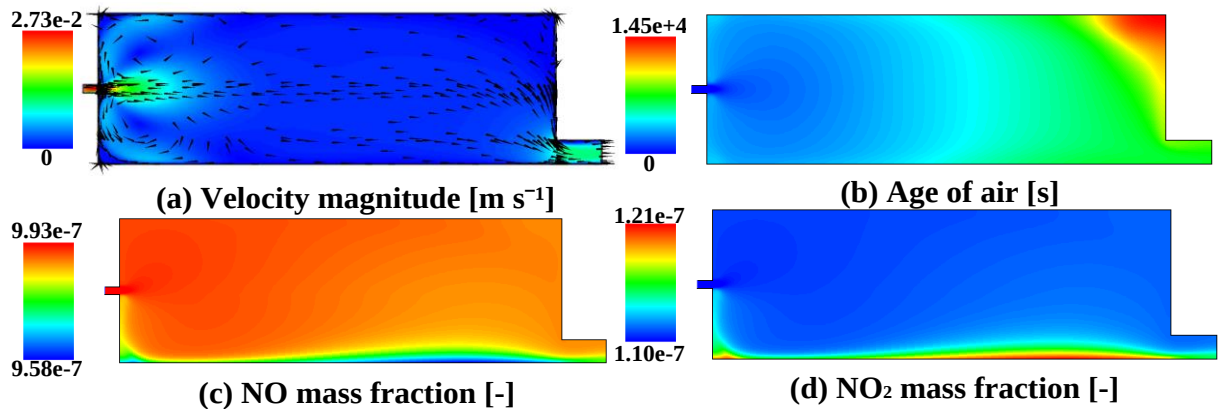

Figure 58: The NOx mass fractions, age of air & velocity magnitude for case 2 while only the floor section is activated.

Lastly, the variant of case 4 is plotted in Figure 59, in which only the left wall section is photocatalytically active. As was concluded from Figure 56, the NO_x conversion by the photocatalytic material on the left wall is negligible (≈ 0%). In fact, it is pointed out by Figure 59a, that the extremely low NO_x conversion by the left wall is caused due to high velocities in its proximity.

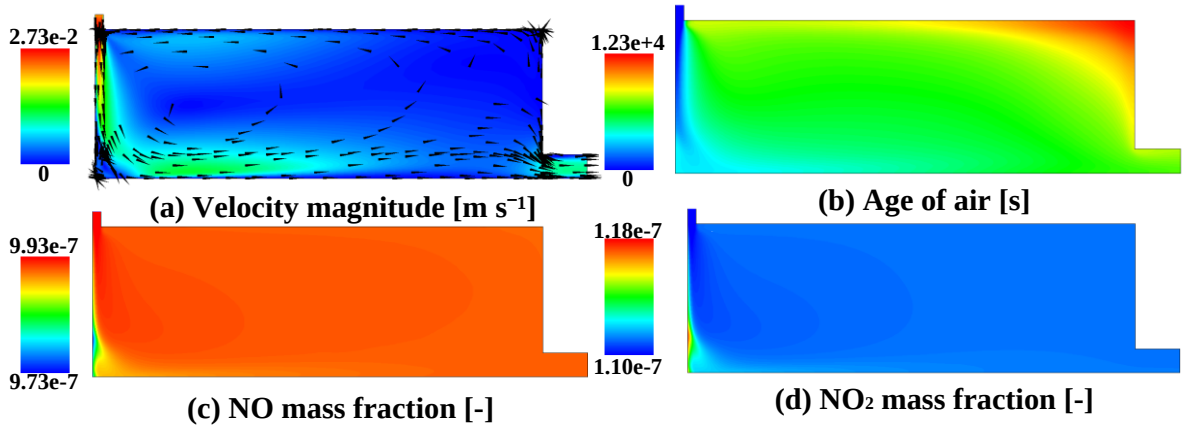

Figure 59: The (a) velocity magnitude and direction, (b) age of air and (c) (d) NO_x mass fractions for case 4 while only the left wall section is activated.

6.4.4. The effect of different ACH values on $NO_{x;con}$ while using different pollution types

The next parameters that are analyzed are the effect of different ACH values on $NO_{x_{con}}$, while using different pollution types. While in [2] and in this report, the performance indicator $NO_{x_{con}}$ is primarily applied for the assessment of the photocatalyst effectiveness of the photocatalyst to convert NO_x, in particular cases in which different pollution types are applied undesired values for $NO_{x_{con}}$ can be obtained. During the simulations, the different pollution types are employed in the benchmark case (case 1) starting from with the standard conditions, while increasing the ACH. As is evident from Figure 60, the trends of $NO_{x_{con}}$ for both pollution types in Figure 60b, does not match the trends of the NO_x mass flow created by photocatalytic reaction ($\dot{m}_{NOx;r}$ [kg s^{-1}]) in Figure 60b. Extensive explanation of the pollution types can be found in the previous Section 6.2.2.

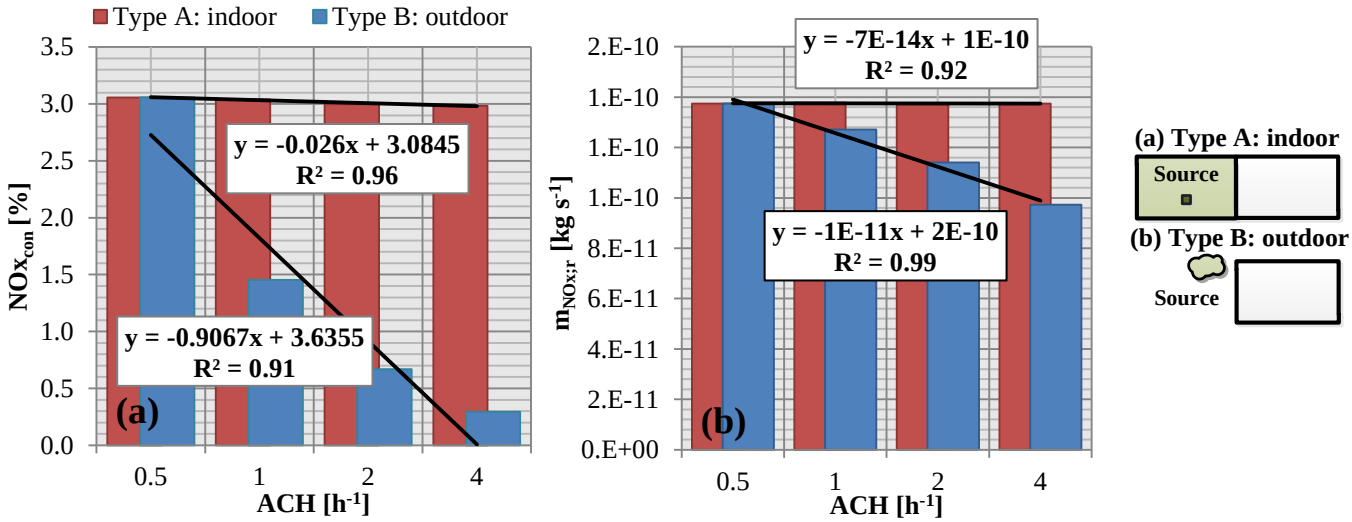

Figure 60: The conversion of NOx, (a) $NO_{x_{con}}$ [%], and the mass flow due to reactions, (b) m_r [kg s-1], in the room for different ACH's for the indoor and outdoor source using standard conditions.

Since, for outdoor pollution (type B), the NO_{xcon} declines when ACH increases, the ingoing mass flow is increased, in contrast to the indoor pollution (Type A), as illustrated in Figure 61a. This has additional implications for the average NO_x concentration in the room, as demonstrated in Figure 61b. These findings confirm that both pollution types differ greatly, as was pointed out in Section 6.2.2. However, more importantly the trend of $NO_{x_{con}}$ for both pollution types does not match the trend of the NO_x mass flow (Figure 60), and so it is concluded that $NO_{x_{con}}$ can evaluate the NO_x conversion rate incorrectly.

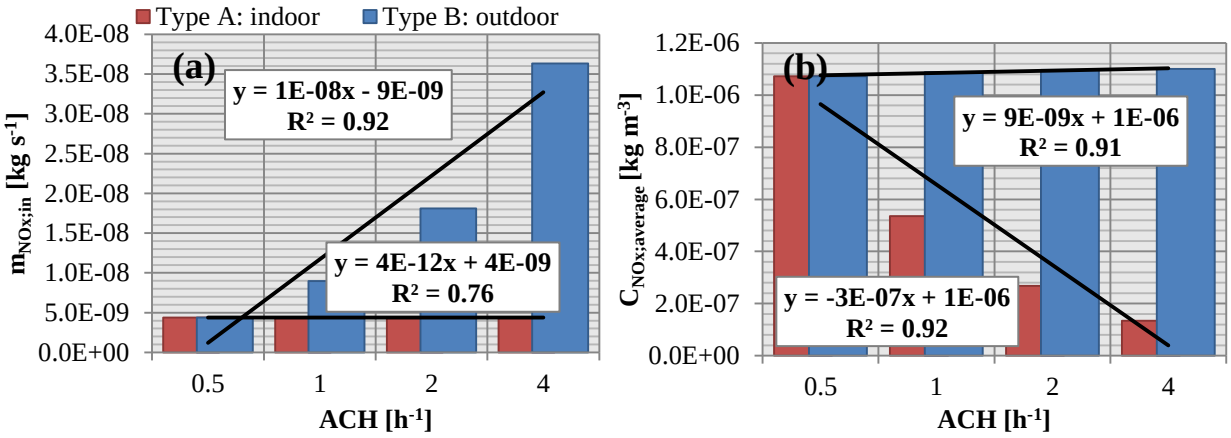

Figure 61: The ingoing mass flow NOx, (a) $\dot{m}_{NOx;in}$ [kg s^{-1}], and the average NOx concentration, (b) $C_{NOx;average}$, in the room for different ACH's for the indoor and outdoor source using standard conditions.

6.4.5. The effect of turbulent intensity

Now, the effect of the turbulence intensity on the conversion of NO_x is analyzed. In Section 6.1, it was suggested that increasing the turbulence in the flow at the inlet would increase the mixing in the room and thereby increase the degradation of NO_x. Consequently, in Figure 62, the $NO_{x_{con}}$ is plotted per turbulence length at the inlet for case 1, using the standard conditions. As can be seen, the total increase of $NO_{x_{con}}$ is insignificantly small (≈ 0.003%). When the turbulence length is plotted for case 1 using the standard conditions, it is revealed that the main turbulence is generated by the flow after departure of the inlet due to collision with the recirculating air. This implies that additional generation of turbulence at the inlet is not a great optimization strategy; instead it seems that a great amount of turbulence is generated by the collision of flow after the flow has left the inlet.

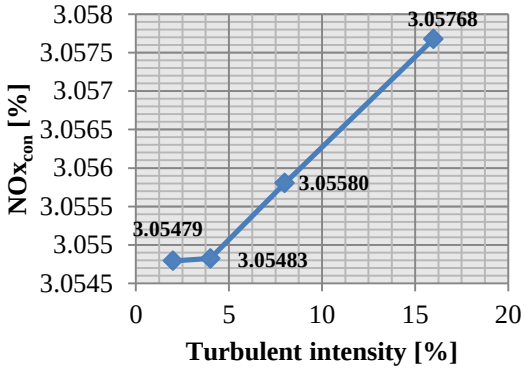

Figure 62: The conversion of NO_x, $NO_{x_{con}}$[%], as function of different turbulence lengths at the inlet of case 1, using standard conditions.

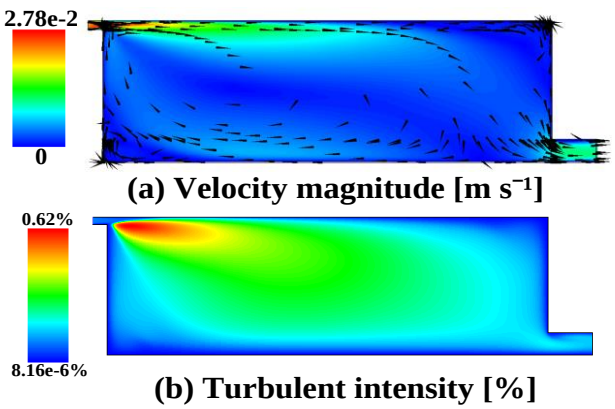

Figure 63: The velocity magnitude and the turbulence intensity the benchmark model.

6.4.6. The effect of catalyst dosage values in default and ideal mixed flow conditions

In this section, the effect of the different dosage values on the conversion in case 1, in an ideal mixed flow and a regular flow is reported. To predict the regular flow, the CFD model of the benchmark room is applied, while the ideal mixed flow is simulated with the model from Chapter 5. Afterwards, the differences between the models were observed to estimate the maximal available increase of NO_x degradation due to mixing. The models were resolved for different catalyst dosage values ranging between 0 and 0.11. Models with a catalyst dosage above 0.11 could not be solved due to the generation of complex numbers. FLUENT notified this by generating the error message "*Floating point error-invalid number*". During the simulations, a Q = 0.0038 m^3s^{-1} (= 0.5 ACH) was applied, while a uniform irradiance field of E = 2 Wm^{-2} was assumed. For the other boundary conditions, the standard conditions from Table 19 were adapted. Figure 64 shows the performance indicator $NO_{x_{con}}$, for both models as function of different catalyst dosage values. As can be seen, the ideal mixed flow clearly provides higher conversion rates.

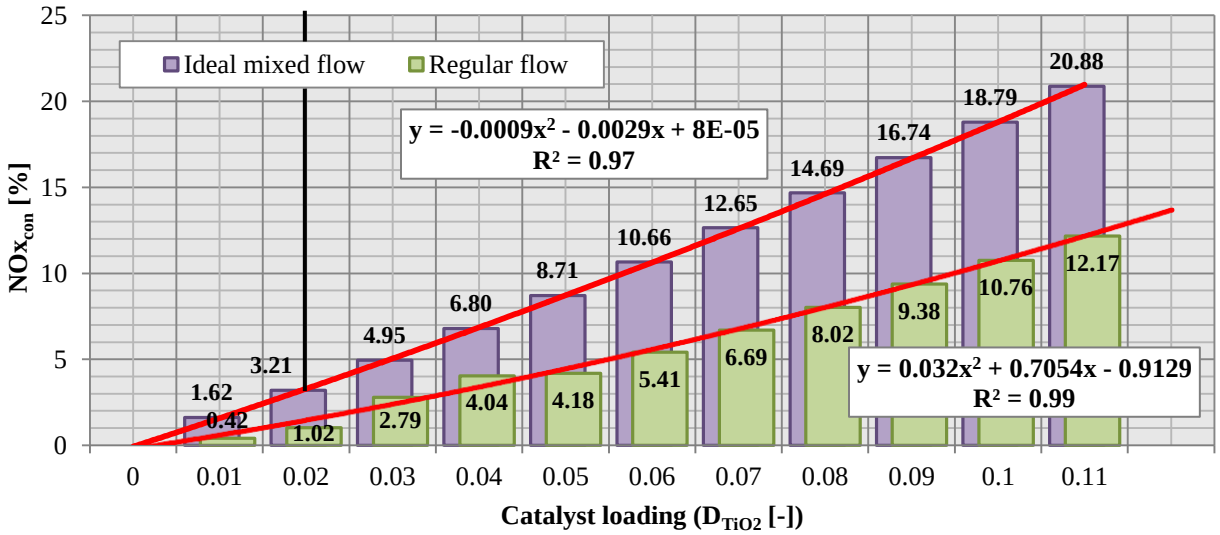

Figure 64: The $NO_{x;con}$ for different catalyst dosage values for both numerical models. The black line represents the minimum dosage that was used in [3].

Extrapolating the trend lines in Figure 64, it is estimated that 100% conversion is achieved in regular flow at D_{TiO2} = 0.525, while the ideal flow achieves complete conversion of NO_x at D_{TiO2} = 0.317.

Subsequently, the relative difference (d_r [%]) between the models is analyzed by applying the following equation:

$$d_r = 100\frac{NO_{x;con;regular}}{NO_{x;con;ideal\_mixed}} \tag{6-26}$$

Where $NO_{x;con;regular}$ and $NO_{x;con;ideal\_mixed}$ [%] are the $NO_{x;con}$ for respectively the regular flow and the ideal mixed flow. On the average, a relative difference of 49% ($d_{r;average}$[%]) is found, implying that the ideal mixed flow provides a 49% higher conversion rate than regular flow.

Furthermore, the results point out that NO_x conversion increases when the amount of dosage increases. However, for increased photocatalytic activity more NO_2 can be generated, which causes a possible harmful health situation for the occupants in the room. Therefore, the findings on the generation of NO_2 are analyzed next.

First or all, the outgoing NO_x concentrations for both flows are shown in Figure 65. It appears from Figure 65b, that in both flows, the increasing NO_2 generation reverses above a D_{TiO2} of 0.05.

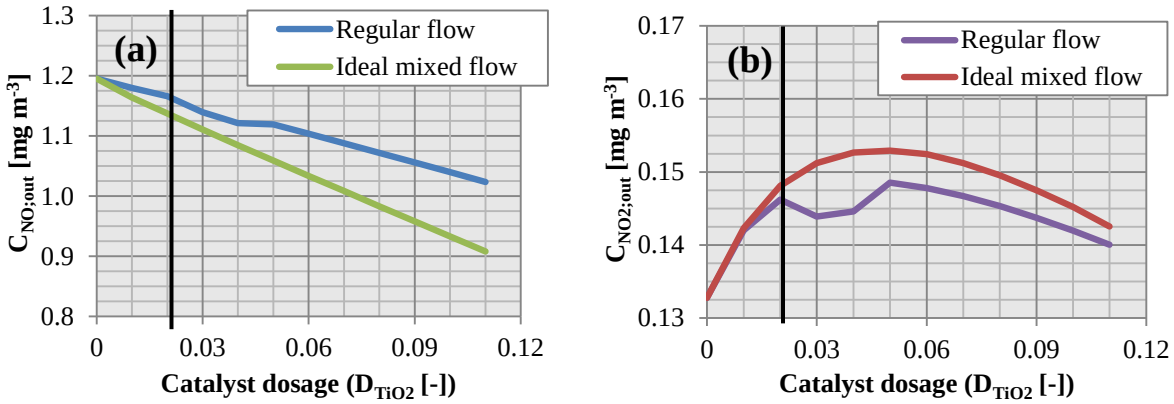

Figure 65: The outgoing (a) NO and (b) NO_2 concentrations for both models per catalyst dosage. Note that both $C_{NO;in}$ and $C_{NO2;in}$ are equal to $C_{NO;out}$ and $C_{NO2;out}$ at 0 dosage. The black line represents the minimum dosage that was used in [3].

Additionally, the NO_x concentration of the CFD simulations is plotted to provide understanding of the concentration development as function of the catalyst dosage, as illustrated in Figure 66. It appears that NO_2 concentrations did not increase further beyond 0.152 mg m^{-3} (= $1.65 \cdot 10^{-7} \rho_{air}$). Also, the plots suggest that the highest NO_2 concentrations only occur near the photocatalytic-active walls, while the concentrations in the remaining room remain lower. Furthermore, it is concluded that the most photocatalytic activity occurs at the left wall section as was also found in Section 6.4.3. The black circles in the lower-left corner indicate the cells in which the complex numbers were generated for models with a photocatalyst dosage of ≤ 0.12. Models with higher dosage values could not be solved.

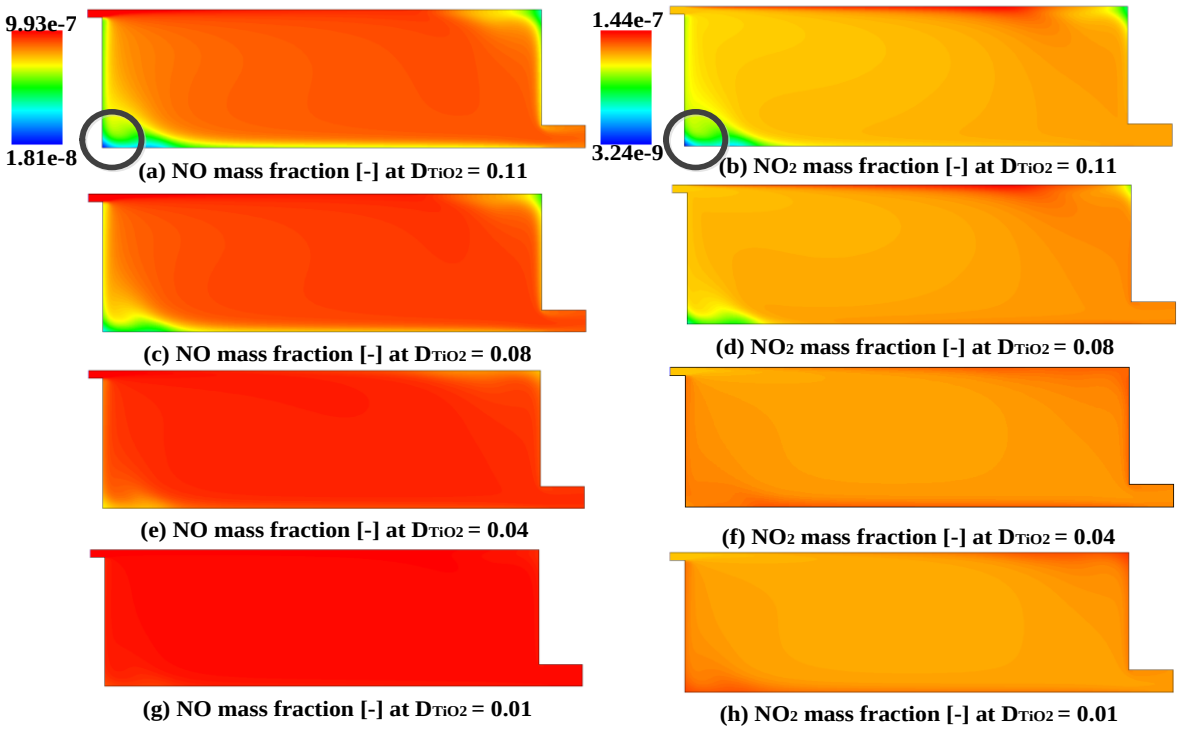

Figure 66: The mass fraction of NOx in case 1 for different photocatalyst dosage values. Within the cells indicated by the black circles, photocatalyst dosage values higher than 0.12 cannot be resolved, since complex numbers are generated.

6.4.7. The effect of different NO / NO_2 ratios at different catalyst dosage values

Finally, the default NO / NO_2 ratio of 90% / 10% is varied to study this turning point and analyze the effect varying NO_x mixture composition on the NO_x conversion. In the previous section, it was found that, when in a simulation the catalyst dosage increased, first, the generation of NO_2 increased followed by a decline beyond a dosage of 0.05. While in the previous simulations a NO_x mass flow of $5 \cdot 10^{-9}$ kg s^{-1} and a NO / NO_2 ratio of 90% / 10% were maintained, in this section the simulations from the previous section are repeated with different ratio according to Table 26. Sequentially, a series of simulation are performed, based on the standard conditions from Table 19 with exception of a Q = 0.0038 m^3 s^{-1} (= 0.5 ACH) and an uniform irradiance field of E = 2 Wm^{-2}. The results of these simulations are presented in Figure 67.

Table 26: Various NO_x compositions, mass fractions and concentrations for a NO_x mass flow of $5 \cdot 10^{-9}$ kg s^{-1}

NO_x composition [NO% / NO_2%]	Y_{NO_in} [-]	C_{NO_in} [kg m^{-3}]	C_{NO_in} [ppb]	$Y_{NO_2\_in}$ [-]	C_{NO2_in} [kg m^{-3}]	C_{NO2_in} [kg m^{-3}]
90 / 10 (default)	$9.92580 \cdot 10^{-7}$	$1.18 \cdot 10^{-6}$	955	$1.10287 \cdot 10^{-7}$	$1.31 \cdot 10^{-7}$	69
80 / 20	$8.82293 \cdot 10^{-7}$	$1.05 \cdot 10^{-6}$	849	$2.20573 \cdot 10^{-7}$	$2.62 \cdot 10^{-7}$	138
70 / 30	$7.72006 \cdot 10^{-7}$	$9.17 \cdot 10^{-7}$	743	$3.30860 \cdot 10^{-7}$	$3.93 \cdot 10^{-7}$	207

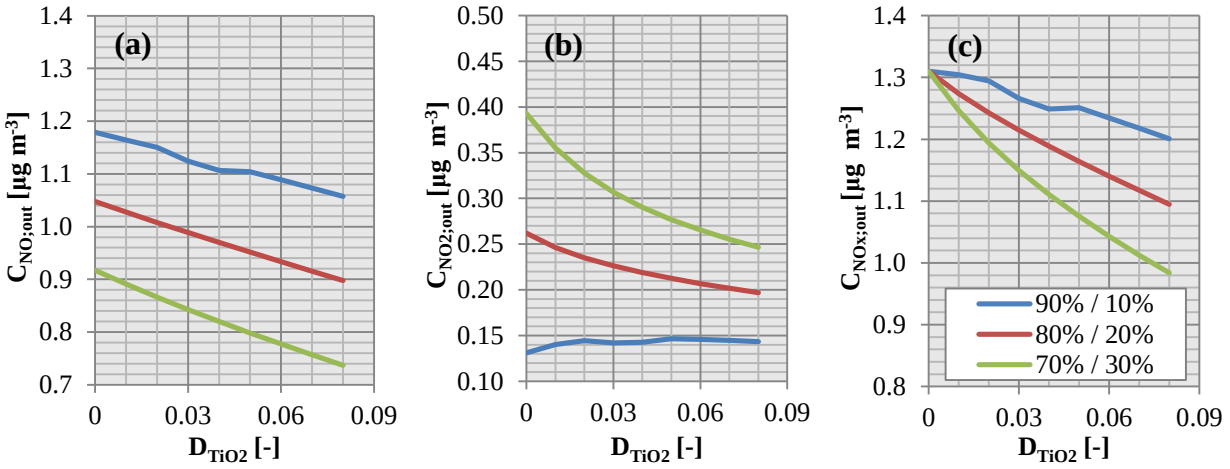

Figure 67: The outgoing NO_x concentration per different catalyst dosage values for three NO_x compositions. Subdivided into (a) $C_{NO;out}$, (b) $C_{NO2;out}$ and (c) $C_{NOx;out}$. It should be noted that both $C_{NO;in}$ and $C_{NO2;in}$ are equal to $C_{NO;out}$ and $C_{NO2;out}$ at a dosage of 0.

Is it found that the NO_x concentration at the outlet decreases when the NO_2 portion in the NO_x mixture increased, as can be seen in Figure 67. This low NO_x concentration obviously implies high NO_x conversion by the photocatalyst in the model. This behavior is explained by studying the chemical reactions proposed in Section 2.2. The reactions in Section 2.2 show that the amount of electrons needed to degrade NO are higher than the amount of electron needed to degrade NO_2. Furthermore, by degrading NO, NO2 is created as intermediate substance. Therefore, if a larger percentage of the NO_x mass flow is composed out of NO_2 higher conversion rates are obtained. These results also show that the increase of NO_2 at the outlet while using low catalyst dosage values at NO_x composed out of 90% NO / 10% NO_2 is no longer present when NO_2 portion increases in the NO_x mixture. Therefore, the increased concentration of NO_2 at the outlet in the room due to photocatalytic activities is limited and is prevented by raising the NO_2 amount in the mixture.

6.5. Discussion

Prior work documented the basic principles for PCO modeling in CFD. However, in previous studies, several assumptions with regard to the irradiance dispersion and quality were made. The present study, however, presents a more comprehensive approach to study the PCO application using numerical modeling, according to the framework presented in Chapter 1. Nevertheless, several aspects of the applied modeling procedures may be further improved in future work and are therefore discussed here.

First of all, during the approximation of the irradiance field, a number of assumptions were made. For example, in line with [1], it was assumed that the emitted spectrum of the fluorescent lamp remained constant for any radiance output level. Also, it was assumed that the reflection and transmission of the materials was equal for wavelengths between 400-570 nm, allowing the development of a monochromatic model. Presumably, for particular conditions, these assumptions may introduce significant modeling errors, yet were not explored in this study. Nevertheless, in Section 4.3.3, an initial approach for an estimation method of the spectral error was suggested.

Secondly, in previous research [2], an air density of 1.158 kg m^{-3} was applied, since a default temperature of 300K was adapted. Therefore, additional errors were introduced in the computation of the mass fraction of NO_x and the computation of the relative humidity. For example, at 300 K, a RH of 50% yields 0.011 mass fraction is water vapor, while at 293.15 K (the temperature in which the experiments were conducted [3]) only 0.0073 mass fraction is water vapor. Furthermore, it is estimated that the applied air density in [2] was 3.8% lower as the air density in the experiments [3], assuming that the density of synthetic air is identical that of ambient air (1.204 kg m^{-3} [88]). Therefore, during this modeling study, the air density was corrected to 1.188 kg m^{-3}, by setting the temperature to 293.15 K. As a result, the error in the weight-estimation was reduced to 1.35% and the error in the estimation of mass faction for water was corrected by 34% downwards. Still, the ambient air surrounding a building is composed from more gasses [109]. For instance, the presence of argon increases the air density quantifiably (≈ 0.03%). However, the effects of other trace gasses are probably negligible, but can affect the kinetics of NO_x.

For the current CFD models, additional options could have dropped calculation requirements without lowering accuracy, but were not exploited. In the kinetic model of NO_x, the generation and consumption of both H_2O and O_2 concentrations were not incorporated, although the concentrations of both gasses are affected by the stoichiometric description [1]. Since the mass of these compounds is not changed by the kinetics, iteration speed for the current models could be increased by substituting nitrogen, oxygen and water by a single gas, using the molecular density of air. For example, uniform water concentration in the room could be incorporated in the UDF of the kinetic model, and thereby making the species conservation equation for water no longer required.

During this study, the GCI was computed from the velocity magnitude integral over the fluid volume in the model. However, it is believed that in future models the CGI should be calculated from the volume integral of a compound concentration, since the concentrations were subjected to large gradients than the velocity. Consequently, additional refinement may be required at the grid near photocatalytic-active walls.

Finally, the generation of the complex numbers in the current CFD model yields a serious limitation to the current modeling method. The complex numbers were the result of the negative term within the exponential expression of the kinetic model in equation (5-10) and cannot be solved by the current solver in FLUENT. Similar limitations were also observed during the second modeling study. Several solutions for future modeling efforts are recommended in the final chapter of this thesis.

6.6. Conclusion

First, the absence of irradiance dispersion in the room was addressed by deriving an irradiance dispersion function and integrating it into the CFD models. The effects of required illuminance for general indoor activities on NO_x degradation in the benchmark case (Figure 40: case 1) were studied, using a typical office irradiance distribution. It was observed that for required illuminance values for general office activities (500 lx), an average of 1.7 W m^{-2} was available, while 10 W m^{-2} was assumed [2]. However, no uniform irradiance field was found, as an irradiance ratio of 1:0.26:0.48 for respectively the floor, ceiling and walls was computed. The increase in NO_x conversion was not proportional to the illumination quantity, but fits a logarithmic relationship. This relationship is caused by the application of the constant emission spectrum of the light source and the monochromatic properties of the model, which produced a linear correlation between the illumination and the irradiation. As a result, an illuminance increase at low illuminane levels increase in photocatalytic activities further as an increase at high illuminance levels.

The analysis of the irradiance dispersion within the benchmark room was expanded with the study of the effects of flow, by using different inlet locations and activating the various wall sections individually or collectively. The initial results confirmed the findings on stagnation of [2] by plotting the age of air. Indeed, stagnating air can amplify the NO_x conversion locally near a photocatalyst-coated wall. In the models, stagnation was produced by the recirculation of air at low velocities in corners. However, the degree in which stagnation locally increased NO_x conversion appeared to be highly reliant on the air velocity and irradiance quantity. Stagnation is not a requirement for high NO_x conversion though. In fact, various models with high air change efficiencies (and thus having less stagnation) yielded comparable conversion rates with regard to the models with higher stagnation. Meanwhile, the conversion by a photocatalyst-coated wall can be reduced greatly when high velocity magnitudes parallel to the wall segment near the air jet at the inlet occur. It was also found that during the individual activation of the wall sections, the ceiling received 76% less irradiance than the floor, whereas the average NO_x conversion by the celling was only 12% lower as by the floor section. Therefore, the ceiling may be a creditable alternative for PCO application when the floor cannot be coated by a photocatalyst.

During analysis of the two pollution types, the trend lines for the $NO_{x_{con}}$ and the mass flow due to photocatalytic reactions did not match. Therefore, the air purification capabilities of the photocatalyst may be assessed incorrectly when the performance indicator $NO_{x_{con}}$ is used. If possible, the mass flow should be used as indicator for assessing the air purification capability of a photocatalyst.

The effect of varying turbulence intensities at the inlet of the room model was studied. An increase in the turbulent intensity increases NO_x conversion insignificantly, as the $NO_{x_{con}}$ is increased by 0.001% at most. In fact, a plot of the turbulence intensity in the room points out that most of the turbulence intensity is created due to collision with other air after the jet of air has left the inlet. Therefore, additional generation of turbulence at the inlet does not provide an effective strategy to increase PCO performance.

The penultimate results provided understanding into the consequences of different catalyst dosage quantities on the conversion in both a regular flow and ideal mixed flow applied in the benchmark room. Clearly, ideal mixing increases the NO_x conversion up to circa 49%. However, for both flows, the local increase of the NO_2 intermediate, due to raised catalyst dosage levels, diminishes above a certain photocatalytic activity level. While the highest NO_2 concentrations occur near the photocatalytic-coated walls, the remaining concentrations in the room are significant lower. Meanwhile, the last findings show that the increase of NO_2 intermediate at the outlet is eliminated by increasing the NO_2 portion in the NO_x mixture, while the NO_x mass flow remains constant. These findings can be considered in future work.

Chapter 7. **General closure**

7.1. **Conclusion**

During the last years, IAQ has gained attention as one of the foremost environmental concerns. Many global organizations work towards improving identification of hazards. In turn, various alternative air purification technologies are evaluated. Photocatalytic oxidation technology provides the possibility of degrading a broad range of pollutants into harmless compounds using visible light which can support healthy indoor environments. The present work provides a series of improvements to previous research that contribute to an improved modeling approach for PCO application in the built environment by using NO_x as target pollutant. Furthermore, additional insight on the mechanisms of photocatalytic degradation of NO_x within the built environment was obtained by using numerical simulations.

While in the previous work [1, 3], the optical effects of the photocatalytic reactor setup were not considered, in this work through numerical study, the rate constant in the kinetic model was corrected for these effects. Various required experiments were performed in Chapter 3 with which the first modeling study was built. During the numerical study in Chapter 4, it was demonstrated through ray-tracing modeling that the actual irradiance on the photocatalytically active sample could be estimated. It was found that the optical characteristics of both the glass cover and photocatalyst influenced the behavior of irradiance received by photocatalyst surface in the photocatalytic reactor setup. Consequently, the obtained data could not be obtained through experimental endeavor. As it turned out, the irradiance was 1.4% lower than initially assumed [1, 3], resulting in a negligible error. However, when darker substrates are to be used in the experimental setup, the actual irradiance could be overestimated up to 9.8% and introducing a significant error. Based on the numerical results, the rate constant α, calculated in [1], was redefined by α_c, which led to correction of respectively $7.30 \cdot 10^{-6}$ molW^{-1}s^{-1} from $7.20 \cdot 10^{-6}$ mol W^{-1}s^{-1}.

In Chapter 5, a computational model was constructed in Matlab Simulink v.R2012a. This model successfully predicted the experiment results from [3], by applying the kinetic model of NO_x. Consequently, based on the benchmark room [4], an ideally mixed room model (V = 27 m^3; A_{floor} = 9 m^2) was simulated using the principles of the reactor model. Consequently, under standard conditions (Q= $1.17 \cdot 10^{-2}$ m^{3}s^{-1} or AHC 1.56 h^{-1}; C_{NO_in} =500 ppb; $C_{NO_2\_in}$ = 0 ppb; RH = 50% or γ_{H_2O} = 0.0073; E= 2 Wm^{-2}; A_c = 23.352 m^2; D_{TiO_2} = 0.5), an ideal mixed flow in the benchmark room could convert 65% of NO_x. However, while keeping the other parameters constant, for low NO concentrations (C_{NO} < 250 ppb), low volumetric flow rates (Q < $5.85 \cdot 10^{-3}$ m^{3}s^{-1}), and high irradiance values (E > 5 Wm^{-2}), 100% NO_x conversion was obtained. Despite these high conversion rates, it was discussed that optimization strategies for PCO application are restricted greatly by the comfort demands of the occupant. High mixed conditions may therefore not be attainable indoors.

In the third study, as reported in Chapter 6, the CFD benchmark model of [2] was adapted for the CFD modeling and improved with an alternative implementation approach of the kinetic model and incorporation of irradiance dispersion data for a typical office setting. However, the FLUENT solver could not solve the complex numbers which were generated by the negative term within the exponential expression of the kinetic model under specific conditions. As a result, the CFD models could not be solved when negative NO_x mass fractions emerged in specific cells. To promote solvability of the models, a low catalyst dosage 0.02 was applied as standard condition. The low catalyst dosage prevented the generation of negative NO_x mass fractions, since the local NO_x conversion rates remained low through the model.

During the analysis in Chapter 6, the effects of different illumination levels of the room model were analyzed, using the standard conditions (Q = $3.817 \cdot 10^{-3}$ m^3s^{-1} or AHC 0.5 h^{-1}; C_{NO_in} = 500 ppb; $C_{NO_2\_in}$ = 0 ppb; RH = 50% or γ_{H_2O} = 0.0073; $L_{workingplane}$ = 500 lx; A_c = 23.352 m^2; D_{TiO_2} = 0.02). It was primarily found that that at low local velocities and high local irradiance levels, stagnation may considerably increase photocatalytic activity. The stagnation of air was identified by the age of air parameter. Also, with respect to a regular flow, ideal mixing can increase the NO_x conversion significantly up to circa 49%. Furthermore, it was found that the local concentrations of generated intermediate NO_2 were primarily raised near the photocatalyst-coated wall, while the remaining concentration in the residual space was substantially lower. Evermore, it appeared that the increase of NO_2 declined rapidly and eventually decreased above a certain photocatalytic activity level, causing the local concentrations near a photocatalyst-coated wall to be limited to a specific concentration level. The results from this study provided new insights into PCO application and can be used to refine PCO modeling.

7.2. **Recommendations**

Obviously, PCO technology provides an alternative for the conservation of IAQ, although several issues still need to be resolved before this new technology can be practically employed in the indoor environment. Numerical models may provide extra understanding of the PCO performance in complex indoor environments, for which no simple analytical solutions are readily available. In this report, several steps have been undertaken to extend PCO modeling capabilities, improve the accuracy of previous studies and provide additional insight into the workings of PCO. Despite the promising results, it is clear that additional work is required to further optimize and refine PCO modeling. Unfortunately, a tangible method to account for the current limitations has not yet been formulated and should be a starting point for future investigations on PCO modeling. To encourage future work, however, recommendations for modeling improvements and starting points for research are summarized.

To begin with, in the kinetic model of NO_x, only six rate constants were needed, while kinetic models for more complex molecules, such as phenol (C_6H_5OH) [43], require more. As a result, various significant assumptions need to be applied in the kinetic model to avoid over-parametization [43]. Furthermore, for each newly-studied photocatalyst, the rate constants of the kinetic model need to be re-derived. While over-parameterization may pose a problem, the developed numerical plug flow model may resolve some of the implications of over-parameterization. After a new kinetic model is developed and corresponding experimental data is obtained. A numerical model of the used photocatalytic reactor may be applied to fit the kinetic parameters automatically through an automated fitting routine. For example, the Matlab platform offers a wide range of possible solvers, including the recommended genetic solver algorithm (ga) for automated fitting. The experimental data can be entered in Matlab, using matrix notations, as input for the model. Eventually, automation of a fitting routine for obtaining the rate constants may save time and prevent oversimplification which may make the kinetic models more accurate.

Still, during development of the kinetic models, several expressions should be avoided as it provides limitations to the numerical modeling as was found during this work in the NO_x kinetic model. Generally, expressions yielding terms including $1/0$ or $\sqrt{-1}$, should be avoided, since they cannot be solved by the conventional solvers. To evade these expressions, several suggestions are proposed. For example, the kinetic model may be implemented into numerical simulations as set of equations rather than a kinetic model. This may prevent problematic expressions which cause insolvable models.

Secondly, if particular definitions cannot be avoided, substitution of these terms by a Taylor series may be an alternative option. Under certain conditions, the Taylor series can represent a continuous function by an infinite sum of terms and can approximate a potential problematic term (e.g. $\sqrt{(1+x)}$ is approximated by $\sum_{i=1}^{n}(x^i/n!)$ for $|x|<1$). However, the restriction of x determines whether the Taylor series can be adopted. Finally, a programmed restriction can be introduced into the code, through which particular boundary conditions in cells are avoided so that no problematic expression can be generated. Still, this option should be evaded if possible, because it creates a discontinuous function that may not be solved by conventional continuous solvers. Nonetheless, it is clear that additional work is required to solve these issues, as a structural solution will promote PCO modeling capabilities greatly.

While the degree of uniformity and the air change efficiency were used in the last modeling study, they can also be applied for new reactor design. The behavior of reactors is often approximated analytically by ideal reactors for observation and computational purposes. Since the fluids in these ideal reactors are either ideal mixed or have an air change efficiency of 100%, a newly built reactor can be assessed by these indicators establish the degree of approximation of an ideal reactor. Both indicators rely on the age of air parameter, for which several measurement and simulation methods [103] are known.

In future work on optimization strategies, PCO application near or on the ceiling outside of the main occupational zone of a room should be considered primarily. Current results suggest that a photocatalyst applied on the ceiling yields relative high pollutant degradation rates, despite low irradiance level. Generally, the ceiling has a large surface area available for coverage by a photocatalyst, whereas most of the surfaces on the walls and floor in a real room are undoubtedly covered (e.g. furniture, etc.). Additionally, the area above the occupational zone is less restricted by the comfort demands of the occupants, making the local increase of intermediate concentration near the photocatalyst less severe. Therefore, a zones classification, such as a breathing zone [110], provides an extra margin for an acceptable IAQ. By subdividing the room into zones, different concentration threshold levels can be classified based on the exposure times per zone. This permits higher pollution concentrations in areas of the room where occupants reside less time without impairing the IAQ (e.g. outside the main occupational zone near the ceiling). The breathing zone is a local area in which is higher exposure time exists with respect to the rest of the room where occupants breathe as they stand, sit, or lie down [110]. The ASHRAE standards [111] define the dimensions of the breathing zone as the region between 75 and 1800 mm above the floor and more than 600 mm from the walls. Still, little evidence is yet available to support this optimization strategy and therefore should be investigated further. The current kinetic model for NO_x might be a starting point for analyzing additional effects of pollutant dispersion.

However, first, validation of the present PCO modeling approach in CFD should be extended more, since validation in the current work remained limited to the validation of the flow field. Additional numerical models may also be combined in a building performance simulation study to assess the air purifying capabilities of a photocatalyst over time and optimize it energetically. Likewise, the air purifying capabilities of a photocatalyst can be compared with conventional air purification systems to demonstrate potential energy savings. During the development of optimization strategies, the pollutant composition should be considered broadly, as it was found that different pollutant mixes heavily affect the photocatalytic conversion of the total pollutant mass flow (Section 6.4.7).

As a whole, future work is needed to promote development on PCO modeling which can increase the efficiency of photocatalytic technology indoors and thereby effectively create a healthy indoor environment though passive air purification. It is hoped that this work stimulates further research on PCO modeling.

Nomenclature

Variable (Latin)	Description	Standard unit
A	Area	m^2
ACH	Air Change rate per Hour	h^{-1}
C	Concentration	$mol\ m^{-3}$ or $kg\ m^{-3}$ or ppm
D	Dosage of the photocatalyst (D_{TiO2}) or diffusion	kg kg^{-1} or $m^2 s^{-1}$
E	Energy or irradiance	J or $W\ m^{-2}$
f	General notation for a function	-
i	General notation for an entity	-
I	Turbulent intensity	%
k	Rate constant	s^{-1} or $s^{-1}Pa^{-1}$ or $m^3 s^{-1} mol^{-1}$
K	(Equilibrium) constant	$m^3\ mol^{-1}$ or lmW^{-1}
L	Radiance	$W\ m^{-2} sr^{-1}$
m	Mass	kg
M	Molar mass	$mol\ kg^{-1}$
n	General notation for total amount, amount of molecules or refraction index	mol or -
p	Pressure	Pa
r	Reaction rate per surface catalyst	$mol\ m^{-2} s^{-1}$
R	Reflection	-
Re	Reynolds number	-
RH	Relative humidity	%
sd	Standard deviation	-
S_s	Source term	$kg\ m\ s^{-2}$
S	Specular component	-
t	Time	s
T	Temperature	$K\ or\ °C$
Q	Volumetric flow rate	$m^3 s^{-1}$
v	Velocity or Frequency	$m\ s^{-1}$ or m^{-1}
V	Volume or photopic response function	m^3 or -
x	Distance in the x direction or general variable	m or -
y	Distance in the y direction or general variable	m or -
Y	Mass fraction	-
z	Distance in the z direction	m
α	Rate constant, irradiance related	$mol\ W^{-1}\ s^{-1}$
β	Rate constant	$mol\ m^{-2}\ s^{-1}$
θ	Angle	- (degrees)
λ	Wavelength	m
μ	Dynamic viscosity	$Pa\ s$
ρ	Density	$kg\ m^{-3}$
σ	Reflectance coefficient	- or %
τ	Transmittance coefficient	- or %
ϕ	Total radiance flux	W
ψ	Viewing angle	- (degrees)
θ	Viewing angle	- (degrees)
Ω	Solid angle	Sr
∇ (nabla)	Gradient (operator)	m^{-1}

Constants	**Description**	**Value**
c	Light speed in vacuum	$2.99792458 \cdot 10^{8}\ m^2 s$ [87]
h	Planck constant	$6.62607 \cdot 10^{-34}\ Js$ [87]
k_b	Boltzmann constant	$1.3807 \cdot 10^{-23}\ J\ K^{-1}$ [87]
N_a	Avogadro constant	$6.02214 \cdot 10^{-23}\ mol^{-1}$ [87]
$P_{ambient}$	Ambient pressure	$101325\ Pa$ [112]
R_c	Universal gas constant	$8.3144\ J\ K^{-1}\ mol^{-1}$ [113]
$T_{ambient}$	Ambient temperature	$293.15\ K$ [112]

Subscripts	**Description**
ads	Adsorbed on the surface
air	Air
$average$	Average value
c	Catalyst
cb	Conduction Band
e	Emitted
$in\ or\ i$	Incoming/entering
l	Light source
mol	Per mol
o	Outgoing
p	Photopic region or photometric unit or arbitrary pollutant *p*
prf	Photopic Response Function
r	Radiometric unit or reaction
s	Surface
TiO_2	Titanium dioxide catalyst
vb	Valence band
α	Absorbed
λ	Spectral (wavelength dependent)
σ	Reflected

* 1 $ppmv = \frac{10^6 \cdot RT_{ambient}}{P_{ambient} V}\ \ mol/m^3$ (as the ideal gas law may be rewritten to: $\frac{n}{V} = \frac{P}{RT} = C$ and partial pressure is in relative proposition to the part-per-million notation)
** 1 Einstein = 1 mole photons

Works Cited

[1] Q. Yu, M. Ballari and H. Brouwers, "Indoor air purification using hetrogeneous photocatalytic oxidation. Part II: Kinetic Study," *Applied Catalysis B: Environmental (2010),* no. 99, pp. 58-65, 2010.

[2] H. Cubillos Sanabria, Heterogeneous Photocatalytic Oxidation of NOx Under Indoor Conditions: Experimental and Simulation Study, Eindhoven: [Master Thesis], Eindhoven University of Technology, 2011.

[3] Q. Yu and H. Brouwers, "Indoor air purification using hetrogeneous photocatalytic oxidation. Part I: Experimental study," *Applied Catalysis B,* no. 92, pp. 454-461, 2009.

[4] P. Nielsen, "Specification of a two-dimensional test case," *Energy Conservation in Buildings and Community systems, Annex 20: Air Flow Pattern Within Buildings,* pp. 26-29, 35-39, 1990.

[5] World Health Organization, "Global Health Risks - Mortality and burden of disease attributable to selected major risks," World Health Organization, 2009. [Online]. Available: http://www.who.int/healthinfo/global_burden_disease/GlobalHealthRisks_report_full.pdf. [Accessed 21 April 2013].

[6] N. Klepeis, W. Nelson, W. Ott, J. Robinson, A. Tsang, P. Switzer, J. Behar, S. Hern and W. Engelmann, "The National Human Activity Pattern Survey (NHAPS): a resource for assessing exposure to environmental pollutants," *Journal of Exposure Analysis and Environmental Epidemiology,* no. 11, pp. 231-252.

[7] Environmental Protection Agency, "Sick Building Syndrome," 30 September 2010. [Online]. Available: http://www.epa.gov/iaq/pubs/sbs.html. [Accessed 19 November 2011].

[8] S. Burge, A. Hedge, S. Wilson and J. Bass, "Sick Building Syndrome: A study of 4,373 office workers," *The Annals of Occupational Hygiene,* vol. 20, no. 1, 1989.

[9] C. Weschler, "Changes in indoor pollutants since the 1950s," *Atmospheric Environment,* no. 43, p. 153–169, 2009.

[10] K. Smith, "Indoor air pollution in developing countries: recommendation for research," *Indoor Air,* no. 12, pp. 198-207, 2002.

[11] World Health Organisation, "Indoor air pollution and health," September 2011. [Online]. Available: http://www.who.int/mediacentre/factsheets/fs292/en/. [Accessed 2 November 2011].

[12] J. Zhang and K. Smith, "Indoor air pollution: a global health concern," *British Medical Bulletin,* vol. 68, no. 1, pp. 209-225, 2003.

[13] U.S Environmental Protection Agency, "Volatile Organic Compounds," 22 March 2011. [Online]. Available: http://www.epa.gov/iaq/voc.html. [Accessed 2 November 2011].

[14] Building Ecology Research Group, "National Programs to Assess IEQ Effects of Building Materials and Products," 2010. [Online]. Available: http://www.epa.gov/iaq/pdfs/hal_levin_paper.pdf. [Accessed 13 November 2011].

[15] World Health Organisation, Air Quality Guidelines - Global Update 2005, Geneva: Druckpartner Moser, 2006, pp. 9-10, 24-25, 205-207.

[16] E. P. Agency, "By Topic | Laws and Regulations," 23 August 2012. [Online]. Available: http://www.epa.gov/lawsregs/topics/. [Accessed 1 September 2012].

[17] European Commission, "Scienctific Commitee on Health and Environmental Risks - Opinion on risk assessment on indoor air quality," 29 May 2007. [Online]. Available: http://ec.europa.eu/health/ph_risk/committees/04_scher/docs/scher_o_055.pdf. [Accessed 1 September 2012].

[18] P. Wolkoff and G. Nielsen, "Organic compounds in indoor air their relevance for perceived indoor air quality?," *Atmospheric Environment,* no. 35, p. 4407–4417, 2001.

[19] S. Wang, H. Ang and M. O. Tade, "Volatile organic compounds in indoor environment and photocatalytic oxidation: State of the art," *Environmental International,* no. 33, pp. 694-705, 2007.

[20] S. Roark, J. Carera-Fonseca, M. Milazzo, J. White and J. Wander, "Catalytic oxidation of volatile organic liquids," *Journal of Environmental Engineering,* no. 130, pp. 329-327, 2004.

[21] B. Guieysse, C. Hort, V. Platel, R. Munoz, M. Ondarts and S. Revah, "Biological treatment of indoor air for VOC removal: Potential and challenges - review," *Biotechnology Advances,* no. 26, pp. 398-410, 2008.

[22] US Environmental Protection Agency, "Residential Air Cleaners," 4 April 2012. [Online]. Available: http://www.epa.gov/iaq/pubs/residair.html#Photocatalytic_Oxidation_Cleaners. [Accessed 17 June 2012].

[23] Q. Yu, Design of environmentally friendly calcium sulfate-based building materials, [PhD thesis], Eindhoven University of Technology, 2012, p. 117.

[24] A. Cassano and O. Alfano, "Reaction engineering of suspended solid heterogeneous photocatalytic reactors," *Catalysis Today,* no. 58, pp. 167-197, 2000.

[25] A. Eltayeb, O. Khalil, S. Al-Hallaj and F. Teymour, "Design and modeling of optical modules for use in the 'Emerald Forest' algae photobioreactor," *Computers and Chemical Engineering,* no. 34, pp. 1323-1340, 2010.

[26] G. C.-R. G. Sgalari and F. Santarelli, "Discrete ordinate method in the analysis of radiative transfer in photocatalytically reacting media," *International Communications in Heat and Mass Transfer,* vol. 25, no. 5, pp. 651-660, 1998.

[27] H. C. R. A. Carp O, "Photoinduced reactivity of titanium dioxide," *Progress in Solid State Chemistry,* no. 32, pp. 33-177, 2004.

[28] A. Zaleska, "Doped-TiO2: A review," *Recents Patents on Engineering,* no. 2, pp. 157-164, 2008.

[29] Georgia State University, "Band theory of Solids," 2012. [Online]. Available: http://hyperphysics.phy-astr.gsu.edu/hbase/solids/band.html. [Accessed 17 June 2012].

[30] A. L. Linsebigler, G. Lu and J. Yates, "Photocatalysis on TiO2 Surfaces: Principles, Mechanisms, and Selected Results," *Chemical Review,* no. 95, pp. 735-758, 1995.

[31] M. Hoffman, S. Martin, W. Choi and D. Bahnermann, "Environmental Applications of Semiconductor Photocatalysis," *Chemical Reviews,* no. 95, pp. 69-96, 1995.

[32] CIEMAT, "Website Environmental Applications of Solar Energy," 2011. [Online]. Available: http://www.psa.es/webesp/areas/quimica/docs/solar_photocatalysis.pdf. [Accessed 7 December 2011].

[33] T. Guo, Z. Bai, C. Wu and T. Zhu, "Influence of relative humidity on photocatalytic oxidation (PCO) of toluene by TiO2 loaded on actived carbon fibers: PCO rate and intermediates accumulation," *Applied Catalysis B: Environmental,* no. 79, pp. 171-178, 2008.

[34] M. Sleiman, P. Conchon, C. Ferronato and J.-M. Chovelon, "Photocatalytic oxidation of toluene at indoor air levels (ppbv): Towards a better assessment of conversion, reaction intermediates and mineralization," *Applied Catalyst B: Environmental,* no. 86, pp. 159-165, 2009.

[35] J. Mo, Y. Zhang, Q. Xu, Y. Zhu, J. Lamson and R. Zhao, "Determination and risk assessment of by-products resulting from photocatalytic oxidation of toluene," *Applied Catalysis B: Environmental,* no. 89, pp. 570-576, 2009.

[36] L. Sun, G. Li, S. Wan and T. An, "Mechanistic study and mutagenicity assessment of intermediates in photocatalytic oxidation degredation of gaseous toluene," *Chemosphere,* no. 78, pp. 312-318, 2009.

[37] S. O. Baek, Y. S. Kim and R. Perry, "Indoor air quality in homes offices and restautants in korean urban areas - indoor/ outdoor relationships," *Atmospheric Environment,* vol. 31, no. 4, pp. 529-544, 1997.

[38] World Health Organisation, "WHO guidelines for indoor air quality: selected pollutants," 2010.

[39] D. Lee, J. Köhler, E. Grobler, F. Rohrer, R. Sauses, L. Gallardo-Klenner, J. Olivier, F. Dentener and A. Bouwman, "Estimation of Global NOx emissions and their uncertainties.," *Atmospheric Environment,* vol. 31, no. 12, pp. 1735-1749, 1997.

[40] S. Lee and M. Chang, "Indoor and outdoor air quality investigation at schools in Hong Kong," *Chemosphere,* no. 41, pp. 109-113, 2000.

[41] H. Lasa, B. Serrano and M. Salaices, Photocatalytic Reaction Engineering, 1st Edition ed., Springer, 2005, pp. 2-3.

[42] V. Augugliaroa, S. Colucciab, V. Loddoa and L. Marcheseb, "Photocatalytic oxidation of gaseous toluene on anatase TiO2 catalyst: mechanistic aspects and FT-IR investigation," *Applied Catalysis B: Environmental,* no. 20, pp. 15-27, 1998.

[43] A. Piscopo, D. Robert and J. Weber, "Comparison between the reactivity of commercial and synthetic TiO2 photocatalysts," *Journal of Photochemistry and Photobiology A:Chemistry,* no. 139, pp. 253-256, 2001.

[44] J. Moreina, B. Serrano, A. Ortiz and H. Lasa, "A unified kinetic model for phenol photocatalytic degredation over TiO2 Photocatalyst," *Chemical Engineering Science,* vol. 78, no. 20, pp. 186-203, 2012.

[45] T. Obee and R. Brown, "TiO2 photocatalysis for indoor air applications - effects of humidity and trace contaminant levels on the oxidation rates of formaldehyde, toluene, and 1,3-butadiene.," *Environmental Science & Technology,* no. 29, pp. 1223-1231, 1995.

[46] M. Blount and J. Falconer, "Steady-state surface species during toluene photocatalysis," *Applied Catalysis B: Environment,* no. 39, pp. 39-50, 2001.

[47] L. Yang, Y. L.E and M. Ray, "Photocatalytic oxidation of paracetamol: dominant reactants, intermediates, and reaction mechanisms," *Environmental Science Technology,* no. 43, pp. 460-465, 2009.

[48] K. Kolasinski, Surface Science: Foundation of catalysis and Nanoscience, 2nd ed., John Wiley & Sons, Inc., 2008, pp. 128,227-228, 232.

[49] COMSOL A.B., COMSOL Multiphysics Modeling Guide, [COMSOL 3.5. guidebook], COMSOL A.B., 2008, p. 78.

[50] Radiance, "Rendering Options vs. Physically Based Rendering," 1994. [Online]. Available: http://radsite.lbl.gov/radiance/refer/Notes/rpict_options.html. [Accessed 12 July 2012].

[51] Radiance, "Radiance WWW Sever," University of California, 2012. [Online]. Available: http://radsite.lbl.gov/radiance/. [Accessed 8 February 2012].

[52] A. Jacobs, "Radiance Tutorial," 23 January 2012. [Online]. Available: http://www.jaloxa.eu/resources/radiance/documentation/docs/radiance_tutorial.pdf. [Accessed 14 May 2012].

[53] G. Larson and S. R., Rendering with Radiance, The Art and Science of Lightning Visualization, 1st ed., Davis: Morgan Kaufmann Publishers, Inc., 2003, pp. 497, 495.

[54] A. Ruppertsberg and M. Bloj, "Rendering complex scenes for phychophysics using Radiance; How accurate can you get?," *Journal of the Optical Society of America A* , vol. 23, no. 4, pp. 759-768, 2005.

[55] M. Stomp, M. Oliveira and D. Patrício, "A Gently Introduction to Precomputed Radiance Transfer," *RITA*, vol. XIII, no. 2, 2006.

[56] C. Mobley, "The Lambertian BRDF," Ocean Optics, 17 August 2011. [Online]. Available: http://www.oceanopticsbook.info/view/radiative_transfer_theory/level_2/the_lambertian_brdf. [Accessed 3 August 2012].

[57] Ward, G., "Behavior of Materials in RADIANCE," Lawrence Berkeley Laboratory, 2004. [Online]. Available: http://radsite.lbl.gov/radiance/refer/materials.pdf. [Accessed 9 July 2012].

[58] G. Ward, "Measuring and Modeling Anisotropic Reflection," *Computer Graphics*, vol. 2, no. 26, pp. 265-272, 1992.

[59] B. Balling, "A comparative study of the Bidirectional reflectance distribution function of several surfaces as a mid-wave infrared diffuse reflectance standard," Ohio, 2009.

[60] K. Wandachowicz, "Calculation of Luminaires Using Radiance," Poznan University of Technology, Institute of Industrial Electrical Engineering, 2004. [Online]. Available: http://www.jaloxa.eu/mirrors/radiance_workshops/2004/Wandachowicz_paper.pdf. [Accessed 23 July 2012].

[61] G. Antonutto and A. McNeil, "Radiance Primer," [Online]. Available: http://www.radiance-online.org:82/learning/tutorials/radiance-primer.pdf. [Accessed 16 July 2012].

[62] Radiance, "Setting Rendering Options," [Online]. Available: http://radsite.lbl.gov/radiance/refer/Notes/rpict_options.html. [Accessed 12 July 2012].

[63] RADIANCE, "Setting Rendering Options," [Online]. Available: http://radsite.lbl.gov/radiance/refer/Notes/rpict_options.html. [Accessed 13 October 2012].

[64] B. Blocken, CFD in Building Engineering - Fundementals and application in urban physics and wind engineering, Eindhoven University of Technology , 2010.

[65] D. Geisler-Moroder and A. Dür, "Estimating Melatonin suppression and photosynthesis activity in Real-World Scenes from Computer Generated Images," in *5th European Conference on Colour in Graphics, Imaging, and Vision*, Austria, 2010.

[66] D. Montgomery and G. Runger, Applied Statistics and Probability for Engineers, 4th ed., John Wiley & Sons, Inc., 2007, pp. 117, 230-233.

[67] R. Fritz and A. Moneil, "About Radiance - Radsite," 8 August 2012. [Online]. Available: http://www.radiance-online.org/about. [Accessed 1 September 2012].

[68] J. Tombran-Tink and C. Barnstable, Visual Transduction and Non-Visual Light Perception, Humana Press, 2008, pp. 330-345.

[69] K. Sagawa and Y. Takahashi, "Spectral luminous efficiency as a function of age," *Journal of the Optical Society of America*, no. 11, pp. 2659-2067, 2001.

[70] J. Lindsey, Applied Illumination Engineering, 2nd ed., The Fairmont Press, Inc., 1997, p. 240.

[71] M. Ballari, M. Hunger and B. H. Hüsken, "Modelling and experimental study of the NOx photocatalytic degradation employing concrete pavement with titanium dioxide," *Catalyst Today*, no. 151, pp. 71-76, 2010.

[72] M. Hunger and B. H.J.H., "Self-cleaning surfaces as innovative potential for sustainable concrete," in *Proceedings International Conference Excellence in Concrete Construction-through Innovation 2008*, United Kingdom, 2009.

[73] ISO, Fine ceramics (advanced ceramics, advanced technical ceramics) - Test method for air purification performance of semiconducting photocatalytic materials - Part 1: Removal of nitric oxide, [ISO standard], Internationnal Organisation for Standardization, 2007.

[74] D. Dobkin and M. Zuraw, Principles of Chemical Vapot Deposition - What's Going on Inside the Reactor, Kluwer Academic Publishers, 2003, pp. 48-50.

[75] O. Levenspiel, Chemical Reaction Engineering, 3rd ed., John Wiley & Sons, 1999, pp. 14, 84, 121, 241.

[76] Ansys FLUENT, "Ansys FLUENT 12.0 Theory Guide," 23 January 2009. [Online]. Available: https://www.sharcnet.ca/Software/Fluent12/html/th/node128.htm. [Accessed 18 December 2012].

[77] SCOTT, "Scott Borofloat 33," 2011. [Online]. Available: http://www.schott.com/hometech/english/download/brochure_borofloat_e.pdf. [Accessed 19 January 2013].

[78] C. Nave, "Reflection Coefficient for Light," Georgia State University, Department of Physics and Astronomy, [Online]. Available: http://hyperphysics.phy-astr.gsu.edu/hbase/phyopt/reflco.html. [Accessed 10 July 2012].

[79] M. Bass, M. Casimer, J. Enoch, V. Lakshminarayanan, G. Li, C. MacDonald and V. Mahajan, Handbook of Optics, 3rd ed., vol. I, McGraw-Hill Companies, Inc., 2010, p. 12.8.

[80] Ocean Optics, "Sampling Accessories," 2012. [Online]. Available: http://www.oceanoptics.com/catalog/Ocean_Optics_Sampling_Accessories.pdf. [Accessed 24 March 2013].

[81] Ocean Optics, High-Resolution Fiber Optic Spectrometer HR4000l, [Installation and Operation Manual], 2008, pp. 21-22.

[82] Ocean Optics, PX-2 Pulsed Xenon Light Source, [Installation and Operation Instructions], 2012, p. 6.

[83] Konica Minolta, Spectrophotometer CM-2600d, Japan: [User Manual], 2001, p. 8.

[84] P. Apian-Bennewitz, "10th Radiance Workshop, Lawrence Berkeley National Laboratory," 24 August 2011. [Online]. Available: http://www.radiance-online.org/radiance-workshop10/presentations/day1/PAB1_FittingPlasticMetal.pdf. [Accessed 4 July 2012].

[85] G. Ward and R. Shakespeare, Rendering with radiance: The art and science of lighting visualization, Morgan Kaufmann, 1998, pp. 94, 307-308.

[86] Dr. Grobel UV-Elektronic GmbH, Radiometer Sensors UV-VIS Radiometer RM-12, [Technical Specifications], Dr. Grobel UV-Elektronic GmbH, 2007.

[87] Ocean Optics, Certificate of Calibration, [Calibration Document], Certificate #: 11419, 2011.

[88] G. Verkerk, J. Broens, P. Groot, W. Kraendonk, J. Sikkema, J. Westra and I. Wevers-Prijs, BINAS informatieboek vwo / havo voor het onderwijs in de natuurwtenschappen, Wolters-Noordhoff, 1998, p. 17.

[89] Wolfram Mathematica, "Wolfram|Alpha," 2012. [Online]. Available: http://www.wolframalpha.com/input/?i=air+composition. [Accessed 19 November 2012].

[90] A. Bone, T. Kemps, A. Peters and P. H., Bouwkunde tabellenboek, 2nd ed., Wolters-Noordhoff, 2009, p. 214.

[91] NASA, "Examining Spatial (Grid) Convergence," NASA, 17 July 2008. [Online]. Available: http://www.grc.nasa.gov/WWW/wind/valid/tutorial/spatconv.html. [Accessed 27 October 2012].

[92] F. Stern, R. Wilson, H. Coleman and E. Paterson, "Comprehensive approach to verication and validation of cfd simulations part1: Methodology and procedures," *Journal of Fluid Engineering*, vol. 4, no. 123, pp. 793-802, 2001.

[93] H. Awbi, Ventilation of buildings, 2nd ed., Spon Press, 2003, p. 35.

[94] Common Creations, "CFD online," 2012. [Online]. Available: http://www.cfd-online.com/Wiki/Turbulence_intensity. [Accessed 19 November 2012].

[95] Fluent Inc., Fluent 6.3 Tutorial Guide - 7.2.2 Determining Turbulence Parameters, [Fluent Guidebook], Fluent Inc., 2006.

[96] A. Vidal, A. Diaz, A. Hraiki, M. Romero, I. Muguruza, F. Senhaji and J. González, "Solar photocatalysis for detoxification and disinfection of contaminated water: pilot plant studies," *Catalysis Today*, no. 54, pp. 283-290, 1999.

[97] A. Aguia, "Study and development of paints for the photocatalyic oxidation of NOx," 2011. [Online]. Available: http://repositorio-aberto.up.pt/bitstream/10216/62101/1/000148647.pdf. [Accessed 11 December 2012].

[98] Heijst, G.J.G.; Vosse, F.N., Stroming en Diffusie: college aantekeningen, Eindhoven: [Textbook], Eindhoven University Technology, 2006, p. 33.

[99] Common Creations, "Standard k-epsilon model," 2007. [Online]. Available: http://www.cfd-online.com/Wiki/Standard_k-epsilon_model. [Accessed 30 November 2012].

[100] P. Nielsen, F. Allard, H. Awbi, L. Davidson and A. Schälin, Computerational Fluid Dynamics in Ventilation Design; Guidebook no. 10, Forssa: REHVA, 2007, p. 10.

[101] Ansys FLUENT, "7.10 Outflow Boundary Conditions," Fluent Inc., 20 September 2006. [Online]. Available: http://hpce.iitm.ac.in/website/Manuals/Fluent_6.3/fluent6.3/help/html/ug/node243.htm. [Accessed 1 December 2012].

[102] The Society of Light and Lighting (CIBSE), Code for Lighting, Butterworth-Heinermann, 2002, p. 57.

[103] Ansys FLUENT, "9.3.3 Setting Up UDS Equations in FLUENT," 20 09 2006. [Online]. Available: http://hpce.iitm.ac.in/website/Manuals/Fluent_6.3/fluent6.3/help/html/ug/node386.htm. [Accessed 15 10 2012].

[104] E. Mundt, H. Mathisen, N. P.V. and A. Moser, Ventilation Effectiveness, REHVA, 2004, pp. 1, 25-26.

[105] M. Liu, "Age distribution and th degree of mixing in continuous flow stirred tank reactors," *Chemical Engineering Science*, no. 69, pp. 282-393, 2012.

[106] P. W. Longest and S. Vinchurkar, "Effects of mesh style and grid convergence on particle deposition in bifurcating airway models with comparisons to experimental data," *Medical Engineering & Physics*, no. 29, pp. 350-367, 2007.

[107] M. Ali, C. Doolan and V. Wheatley, "Grid convergence study for a two-dimensional simulation of flow around a square cylinder at a low eynolds number," in *Seventh International Conference on CFD in the Minerals and Process Industries*, Melbourne, Australia, 2009.

[108] C. Chen and B. Zhao, "Some questions on dispersion of human exhaled droplets in ventilation room: answers from numerical investigation," *Indoor Air*, no. 20, pp. 95-111, 2010.

[109] F. Stern, R. Wilson, H. Coleman and E. G. Paterson, "Verification and validation of CFD simulations," Iowa Institute of Hydraulic Research, 1999. [Online]. Available: http://www.taoxing.net/web_documents/iihr_cfdvv.pdf. [Accessed 19 November 2012].

[110] The International Union of Pure and Applied Chemistry, Compendium of Chemical Terminology, 2nd ed., Oxford, 1997, p. 2172.

[111] E. P. Agency, "Terms & Arconyms - Search Results," 23 October 2012. [Online]. Available: http://ofmpub.epa.gov/sor_internet/registry/termreg/searchandretrieve/termsandacronyms/search.do?matchCriteria=Contains&checkedTerm=on&checkedAcronym=on&search=Search&term=breathing%20zone. [Accessed 23 October 2012].

[112] R. a. A.-C. E. American Society of Heating, Ventilation for Acceptable Indoor Air Quality, no. 62-2001, [ANSI/ASHRAE Standard], 2004, p. 4.

[113] US Environmental Protection Agency, "Compendium of Methods for the Determination of Inorganic Compounds in Ambient Air," 1 June 1999. [Online]. Available: http://www.epa.gov/ttnamti1/files/ambient/inorganic/mthd-2-4.pdf. [Accessed 29 January 2011].

[114] US Environmental Protection Agency, "EPA On-line Tools for Site Assessment Calculation," 5 January 2012. [Online]. Available: http://www.epa.gov/athens/learn2model/part-two/onsite/ia_unit_conversion_detail.html. [Accessed 3 February 2011].

[115] G. Ward, "The RADIANCE Lighting Simulation and Rendering System," [Online]. Available: http://www.cse.unsw.edu.au/~cs3421/hypergraph/raytrace/radiance/descrip.html. [Accessed 15 08 2012].

Appendix

Appendix 1. Elaboration of the RADIANCE solving algorithms

A-1.1. Direct solver calculation

The direct calculation involves the computation of direct contribution radiation arriving at a surface directly from a light source, with exception of secondary light sources (e.g. *glow*), or via one or multiple ideal specular transfers from additional surfaces [114] (the direct specular component), such as the *mirror*, *glass* and *dielectric* material types [52]. Optional solving algorithms may be applied, including the *Adaptive Source Subdivision* (ASS), *Virtual Light Source* (VLS) algorithm and *Selective Shadow Testing* (SST) algorithm.

Normally, when relative huge light sources are present in a scene, a significant error can arise during a default calculation. To avoid this, the Adaptive Source Subdivision (ASS) solving algorithm needs to be applied. The ASS algorithm divides light sources into rectangular-shaped *sub-samples* on which a certain amount of rays (*jittering*) is calculated, illustrated in Figure 68. The amount of rays will be disproportionally distributed over the sub-samples when applying this solving algorithm.

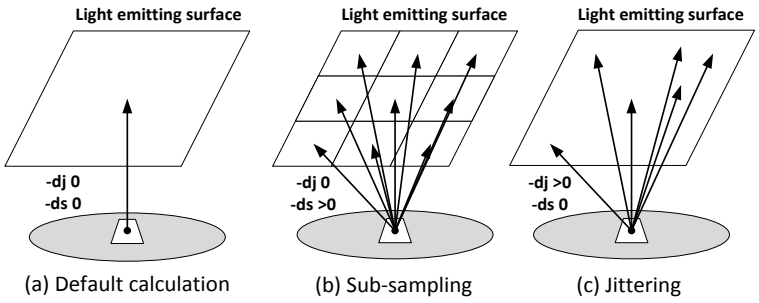

Figure 68: The effect of the direct Jitter ($-dj$) and direct sub-sampling ($-ds$) rendering parameters.

The ASS algorithm is customized with the *direct jitter* ($-dj$) and *direct sub-sampling* ($-ds$) rendering parameters. However, when the default settings ($-dj$ 0 and $-ds$ 0) are applied, this algorithm not applied. Alternatively, a light source can be given the material type *glow* rather than *light*, resulting in an indirectly calculation of the light source. While, a value for $-dj$ of more than 0 will turn on jittering; values below 0.65 are advised. In addition, values above 0 for $-ds$ will turn on sub-sampling of the light source area. Generally, the sub-sampling is performed by rectangular sampling. As a result, certain shapes such as curved, round and L-formed shapes require a higher sub-sampling in order to obtain the correct sub-division [52]; else rays can miss the surface of the light source and cause a potential error in the calculation. Normally, RADIANCE will notify the user when this happens, with exception of cylindrical shapes of which the radius than one fifth of their length. For these geometries a notification will be generated automatically [52].

In turn, the VLS algorithm is employed in scenes where *mirror*, *glass*, *dielectric*, *prism1* or *prism2* material types are employed [52]. By applying material types, virtual or virtual–virtual light sources (copies from other light sources) can be created, which allows the generation of other lights sources to be limited to the incoming angle involved, removing the redundant rays from the calculation and reducing simulation time, illustrated in Figure 69a. The main rendering parameter which configures this algorithm is the *direct relay* ($-dr$) (default value is 2), illustrated in Figure 69a. Before a virtual light source calculation is performed, the rays originating from the virtual sources are pretested for occlusion, saving simulation time. The density (resolution) of the pre-sampling is defined by *direct presampling* ($-dp$). In the predated version of RADIANCE, additional reflections on the material types are only supported for two redirections [52]. As a result, facing mirrors can only duplicate the actual reflective material in the model two folds per mirror, creating two mirror images, illustrated in Figure 69b. However, the recent simulations in RADIANCE v4.1 from this thesis revealed that up to six mirror images can be generated (see Figure 49 as reference).

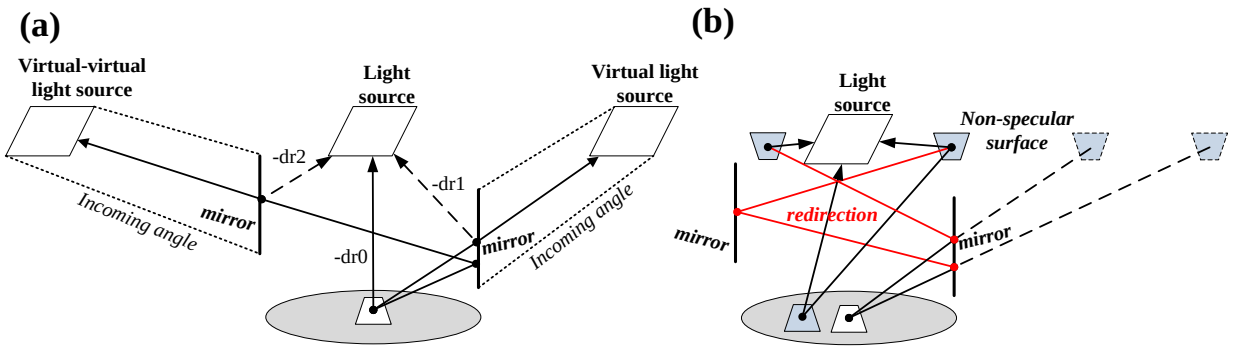

Figure 69: (a) The effect of direct relays ($-dr$) rendering parameter on the generation of virtual light sources. (b) The effect of redirections of reflections: more than two redirections are not supported by RADIANCE [52]. All dotted lines are not calculated in RADIANCE, but are replaced by an alternative ray.

The other solving algorithm, the SST, was not applied during the modeling. Nevertheless, an extended description and corresponding rendering parameters are found in [52]. In short, with the SST algorithm, linearly calculation growth in large scenes with multiple light sources can be avoided by establishing the importance of a light source relative to the whole scene. Through the use of this algorithm, light sources with a small influence on the light distribution in the scene may be discarded, resulting in lower calculation times.

A-1.2. Indirect solver calculation

The indirect calculation (or ambient calculation) includes all sources of irradiance which were not included in the direct calculation. These consist of all diffuse and indirect specular reflection, diffuse transmission (scattering by e.g. mist) and emitted light from the secondary light sources (e.g. the material type *glow*). The indirect calculation is stochastic and therefore causes different results when the model is re-rendered. Additionally, extra solving algorithms are employed during the indirect calculation to limit its calculation time, including the *Specular Sampling* (SS) and *Indirect Irradiance Caching* (IIC) solving algorithm. Several rendering parameters can be adjusted to modify the settings of the indirect calculation; the main rendering parameters are discussed below.

The *ambient bounces* ($-ab\ [N]$) rendering parameter defines the amount of reflections (or bounces) which are performed by a ray before the calculation is terminated. In turn, the *ambient divisions*

($-ad$ [N]) rendering parameters defines the amount of rays which are randomly reflected back in the half hemisphere as result of a diffuse reflection on a surface. The error in the indirect calculation of irradiation is inversely proportional to the square root of $-ad$ [49]. Additionally, when significant contrast differences occur within a model, accuracy in the model can be improved by additional *ambient super samples* ($-as$ [N]). In short, $-as$ allows the generation of an additional N rays when large differences in irradiance are occurring, as result the accuracy during simulation is improved. In Figure 70, a schematic concept both the $-ab$ and $-ad$ rendering parameters are illustrated.

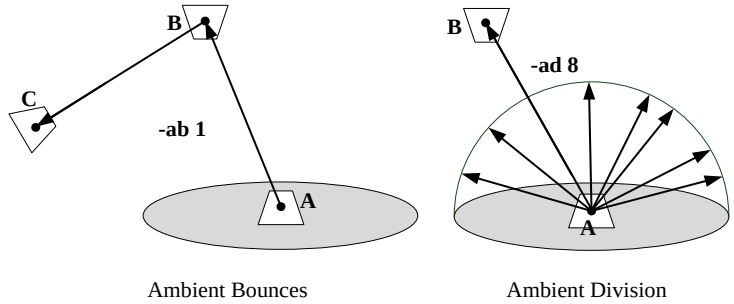

Figure 70: The concept of the ambient bounce and ambient division parameters for arbitrary points A, B and C.

Usually, the rays in the ambient calculation are not sampled in all points on a surface and are therefore interpolated to estimate the values in the remaining points. This is performed automatically in RADIANCE by the IIC solving algorithm. The ICC is constantly applied during simulation to conserve calculation time, especially when a large amount of reflections are calculated. By adjusting the *ambient accuracy* ($-aa$ [acc]) rendering parameter, the maximum error permitted in the indirect irradiance interpolation is specified. Normally, this value should be less than 0.3 (thereby allowing up to 30% error in the indirect calculation) [52]. In turn, the *ambient resolution* ($-ar$ [res]) rendering parameter defines the maximum density of the grid in which the ambient values are interpolated for all incoming rays on a surface [52]. Meanwhile, the solving algorithm ensures that when several incoming rays within an area on a surface have the similar values, the rays are substituted into a single reflection, which in turn conserves calculation time.

Furthermore, the SS solving algorithm allows the calculation of the specular components (non-Lambertian) of a reflection or transmission separately. By sampling the specular components separately, large sources of variance in the integral are removed and thereby promoting solvability. Furthermore, dividing reflectance into components permits the use of different solving (sampling) techniques more efficiently [52]. The related rendering parameter, $-st$ [N] or the *specular threshold* parameter defines the level for which the specular components of reflections are sampled by the SS solving algorithm. Specular components (S) equal to or less then value N will be calculated by the diffuse indirect component with a loss of directionality as result. The default setting is 0.15, whereby all specular components with a S of <0.15 are sampled. Furthermore, the *spectral jitter* parameter ($-\boldsymbol{sj}$ [N]), defines the degree with which the specular highlight is sampled. While with N=0, only the center of a highlight is sampled, the default value 1 allows complete sampling of the highlight.

Appendix 2. Radiance model of the reactor setup

Materials (*.mat)

```
# Crumbled aluminium foil (metal)
void metal alfoil_mat
0
0
5 0.7 0.7 0.7 0.6 0.2

# White paper on the ground
void metal ground_mat
0
0
5 0.761 0.761 0.761 0 0

# photocatalytically active sample
void metal catalyst_mat
0
0
5 0.77 0.77 0.77 0 0

# Inner walls of the reactor
void metal innerreactor_mat
0
0
5 0.3 0.3 0.3 0 0

# Mirrors in the the luminaire
void metal mirror_mat
0
0
5 0.845 0.845 0.845 0.85 0

# Light1
void light lighting_mat
0
0
3 LR1 LB1 LG1
```

```
# Black paper
void metal black_mat
0
0
5 0.042 0.042 0.042 0.01 0

# Borosilicate glass
void dielectric glass_mat
0
0
5 1.0 1.0 1.0 1.4768 0

# Luminaire casing
void metal luminairecasing_mat
0
0
5 0.713 0.713 0.713 0.03 0

# Outerside walls of the reactor
void metal outerreactor_mat
0
0
5 0.678 0.678 0.678 0.03 0

# Antimatter (removes material)
void antimatter antimatter_mat
2 void reactorcasing_mat
0
0

# Light2
void light lighting_2_mat
0
0
3 LR2 LB2 LG2
```

Sampling points at 139, 150 and 185 mm height for simulation of the irradiation on the glass cover and the catalyst surface (*.pts)

```
.24271 .2815 .13901 0 0 1
.27014 .2815 .13901 0 0 1
.29757 .2815 .13901 0 0 1
.32500 .2815 .13901 0 0 1
.35243 .2815 .13901 0 0 1
.37986 .2815 .13901 0 0 1
.40729 .2815 .13901 0 0 1

.24271 .32500 .13901 0 0 1
.27014 .32500 .13901 0 0 1
.29757 .32500 .13901 0 0 1
.32500 .32500 .13901 0 0 1
.35243 .32500 .13901 0 0 1
.37986 .32500 .13901 0 0 1
.40729 .32500 .13901 0 0 1

.24271 .3685 .13901 0 0 1
.27014 .3685 .13901 0 0 1
.29757 .3685 .13901 0 0 1
.32500 .3685 .13901 0 0 1
.35243 .3685 .13901 0 0 1
.37986 .3685 .13901 0 0 1
.40729 .3685 .13901 0 0 1
```

```
.24271 .2815 .15001 0 0 1
.27014 .2815 .15001 0 0 1
.29757 .2815 .15001 0 0 1
.32500 .2815 .15001 0 0 1
.35243 .2815 .15001 0 0 1
.37986 .2815 .15001 0 0 1
.40729 .2815 .15001 0 0 1

.24271 .32500 .15001 0 0 1
.27014 .32500 .15001 0 0 1
.29757 .32500 .15001 0 0 1
.32500 .32500 .15001 0 0 1
.35243 .32500 .15001 0 0 1
.37986 .32500 .15001 0 0 1
.40729 .32500 .15001 0 0 1

.24271 .3685 .15001 0 0 1
.27014 .3685 .15001 0 0 1
.29757 .3685 .15001 0 0 1
.32500 .3685 .15001 0 0 1
.35243 .3685 .15001 0 0 1
.37986 .3685 .15001 0 0 1
.40729 .3685 .15001 0 0 1
```

```
.24271 .2815 .185 0 0 1
.27014 .2815 .185 0 0 1
.29757 .2815 .185 0 0 1
.32500 .2815 .185 0 0 1
.35243 .2815 .185 0 0 1
.37986 .2815 .185 0 0 1
.40729 .2815 .185 0 0 1

.24271 .32500 .185 0 0 1
.27014 .32500 .185 0 0 1
.29757 .32500 .185 0 0 1
.32500 .32500 .185 0 0 1
.35243 .32500 .185 0 0 1
.37986 .32500 .185 0 0 1
.40729 .32500 .185 0 0 1

.24271 .3685 .185 0 0 1
.27014 .3685 .185 0 0 1
.29757 .3685 .185 0 0 1
.32500 .3685 .185 0 0 1
.35243 .3685 .185 0 0 1
.37986 .3685 .185 0 0 1
.40729 .3685 .185 0 0 1
```

Lightsource geometry (lightsource.rad)

```
lighting_2_mat cylinder lighta_rad
0
0
7
0      -0.279 0.059
0      -0.254 0.059
0.014

lighting_2_mat cylinder lightb_rad
0
0
7
0      0.254  0.059
0      0.279  0.059
0.014

lighting_mat cylinder light_rad
0
0
7
0      -0.254 0.059
0      0.254  0.059
0.014

mirror_mat cylinder lightr1_rad
0
0
7
0      -0.2855       0.059
0      0.2855 0.059
0.0139

black_mat cylinder c1_rad
0
0
7
0      -0.295 0.059
0      -0.279 0.059
0.014

black_mat cylinder c2_rad
0
0
7
0      0.279  0.059
0      0.295  0.059
0.014
```

Mirror (type I) geometry (mirrorI.rad)

```
mirror_mat polygon ceilingm_rad
0
0
12
0.00   -0.295 0.04
0.005  -0.295 0.04
0.005  0.295  0.04
0.00   0.295  0.04

!gensurf       mirror_mat       sidem_rad\
'0.0045*s^2.5' '0.590*t' '0.04*s' 25 25 \
xform -t 0.0005 -0.295 0

mirror_mat polygon sideat_rad
0
0
12
0.00   -0.295 0.00
0.0005 -0.295 0.00
0.0005 0.295  0.00
0.00   0.295  0.00
```

Mirror (type II) geometry (mirrorII.rad)

```
black_mat polygon ceilingt_rad
0
0
12
0.00   -0.295 0.08
0.04875       -0.295 0.08
0.04875       0.295  0.08
0.00   0.295  0.08

!gensurf         mirror_mat         mirror\
'0.0487*(0.77606*s^4-\
0.5951*s^3+0.4611*s^2+0.3698*s)'
'0.590*t'\  '0.08*s'  25  25  |  xform  -t
0.0005 -0.295 0

mirror_mat polygon sideat_rad
0
0
12
0.00   -0.295 0.00
0.0005 -0.295 0.00
0.0005 0.295  0.00
0.00   0.295  0.00
```

Reactor Casing geometry (casing.rad)

```
ground_mat polygon floor_rad
0
0
12
0.00   0.00   0.00
0.65   0.00   0.00
0.65   0.65   0.00
0.00   0.65   0.00

reactorcasing_mat polygon back_rad
0
0
12
0.00   0.00   0.00
0.65   0.00   0.00
0.65   0.00   0.40
0.00   0.00   0.40


reactorcasing_mat polygon left_rad
```

```
reactorcasing_mat polygon shaft2_rad
0
0
12
0.075  0.65   0.35
0.075  0.80   0.35
0.575  0.80   0.35
0.575  0.65   0.35

reactorcasing_mat polygon shaft3_rad
0
0
12
0.075  0.65   0.05
0.075  0.80   0.05
0.075  0.80   0.35
0.075  0.65   0.35


reactorcasing_mat polygon shaft4_rad
```

```
0
0
12
0.00   0.00   0.00
0.00   0.65   0.00
0.00   0.65   0.40
0.00   0.00   0.40

reactorcasing_mat polygon right_rad
0
0
12
0.65   0.00   0.00
0.65   0.65   0.00
0.65   0.65   0.40
0.65   0.00   0.40

!genrbox glass_mat box 0.59 0.59 0.004 \
| xform -t 0.03 0.03 0.40
!genrbox reactorcasing_mat box 0.65 0.03\
0.004 | xform -t 0.00 0.00 0.40
!genrbox reactorcasing_mat box 0.65 0.03\
0.004 | xform -t 0.00 0.62 0.40
!genrbox reactorcasing_mat box 0.03 0.59\
0.004 | xform -t 0.00 0.03 0.40
!genrbox reactorcasing_mat box 0.03 0.59\
0.004 | xform -t 0.62 0.03 0.40

reactorcasing_mat polygon front1_rad
0
0
12
0.00   0.65   0.00
0.65   0.65   0.00
0.65   0.65   0.05
0.00   0.65   0.05

reactorcasing_mat polygon front2_rad
0
0
12
0.00   0.65   0.35
0.65   0.65   0.35
0.65   0.65   0.40
0.00   0.65   0.40

reactorcasing_mat polygon front3_rad
0
0
12
0.00   0.65   0.05
0.075  0.65   0.05
0.075  0.65   0.35
0.00   0.65   0.35

reactorcasing_mat polygon front4_rad
0
0
12
0.575  0.65   0.05
0.65   0.65   0.05
0.65   0.65   0.35
0.575  0.65   0.35

reactorcasing_mat polygon shaft1_rad
0
0
12
0.075  0.65   0.05
0.075  0.80   0.05
0.575  0.80   0.05
0.575  0.65   0.05
```

```
0
0
12
0.575  0.65   0.05
0.575  0.80   0.05
0.575  0.80   0.35
0.575  0.65   0.35

black_mat polygon shaftcloser_rad
0
0
12
0.075  0.80   0.05
0.575  0.80   0.05
0.575  0.80   0.35
0.075  0.80   0.35

antimatter_mat sphere sphere1_rad
0
0
4
0.0    0.325  0.2    0.07499

antimatter_mat sphere sphere2_rad
0
0
4
0.65   0.325  0.2    0.07499

reactorcasing_mat cylinder cylinder1_rad
0
0
7
0.00001      0.325  0.2
-0.16  0.325  0.2
0.075

reactorcasing_mat cylinder cylinder2_rad
0
0
7
0.64999      0.325  0.2
0.81   0.325  0.2
0.075

black_mat polygon cylindercloser1_rad
0
0
12
-0.15  0.250  0.275
-0.15  0.250  0.125
-0.15  0.400  0.125
-0.15  0.400  0.275

black_mat polygon cylindercloser2_rad
0
0
12
0.80   0.250  0.275
0.80   0.250  0.125
0.80   0.400  0.125
0.80   0.400  0.275
```

Luminaire geometry (luminaire.rad)

```
luminairecasing_mat polygon ceilin1l_rad
0
0
30
0.305  -0.305 0.00
0.305  0.305  0.00
-0.305 0.305  0.00
-0.305 -0.305 0.00
-0.295 -0.295 0.00
0.295  -0.295 0.00
0.295  0.295  0.00
-0.295 0.295  0.00
-0.295 -0.295 0.00
-0.305 -0.305 0.00

mirror_mat polygon ceiling1l_rad
0
0
30
0.295  -0.295 0.00
0.295  0.295  0.00
-0.295 0.295  0.00
-0.295 -0.295 0.00
-0.285 -0.285 0.00
0.285  -0.285 0.00
0.285  0.285  0.00
-0.285 0.285  0.00
-0.285 -0.285 0.00
-0.295 -0.295 0.00

luminairecasing_mat polygon frontl_rad
0
0
12
0.295  -0.295 0.00
0.295  -0.295 0.085
0.295  0.295  0.085
0.295  0.295  0.00
```

```
luminairecasing_mat polygon backl_rad
0
0
12
-0.295 -0.295 0.00
-0.295 -0.295 0.085
-0.295 0.295  0.085
-0.295 0.295  0.00

luminairecasing_mat polygon leftl_rad
0
0
12
0.295  0.295  0.00
0.295  0.295  0.085
-0.295 0.295  0.085
-0.295 0.295  0.00

luminairecasing_mat polygon rightl_rad
0
0
12
0.295  -0.295 0.00
0.295  -0.295 0.085
-0.295 -0.295 0.085
-0.295 -0.295 0.00

luminairecasing_mat polygon ceiling2l_rad
0
0
12
-0.295 -0.295 0.085
0.295  -0.295 0.085
0.295  0.295  0.085
-0.295 0.295  0.085

!xform -rz 0 -t 0.1925 0.00 0.00 -a 3 –t\
-0.1925 0 0 -a 2 -rz 180 lightsource.rad
!xform -rz -90 -t 0 0.285 0.00 -a 6 -t \ 0
-0.095 0 -a 2 -rz 180 mirrorI.rad
!xform -t 0.095 0 0.00 -a 3 -t -0.19 0\
0 -a 2 -rz 180 -t 0 0 0 mirrorII.rad
```

Reactor geometry (reactor.rad)

```
outerreactor_mat polygon floorr_rad
0
0
24
0.105  -0.10  0.00
0.185  -0.01  0.00
0.185  0.01   0.00
0.105  0.10   0.00
-0.105 0.10   0.00
-0.185 0.01   0.00
-0.185 -0.01  0.00
-0.105 -0.10  0.00
outerreactor_mat polygon frond1r_rad
0
0
12
0.185  0.01   0.00
0.185  0.01   0.12
0.185  -0.01  0.12
0.185  -0.01  0.00
outerreactor_mat polygon back1r_rad
0
0
12
-0.185 0.01   0.00
-0.185 0.01   0.12
-0.185 -0.01  0.12
-0.185 -0.01  0.00
outerreactor mat polygon frond2r rad
```

```
outerreactor_mat polygon border1r_rad
0
0
54
0.12   -0.13  0.15
0.22   -0.02  0.15
0.22   0.02   0.15
0.12   0.13   0.15
-0.12  0.13   0.15
-0.22  0.02   0.15
-0.22  -0.02  0.15
-0.12  -0.13  0.15
-0.105 -0.10  0.15
0.105  -0.10  0.15
0.185  -0.01  0.15
0.185  0.01   0.15
0.105  0.10   0.15
-0.105 0.10   0.15
-0.185 0.01   0.15
-0.185 -0.01  0.15
-0.105 -0.10  0.15
-0.12  -0.13  0.15
!genrbox glass_mat box 0.21 0.20 0.008\
| xform -t -0.105 -0.1 0.142
!genrbox glass_mat box 0.08 0.02 0.008\
| xform -t 0.105 -0.01 0.142
!genrbox glass_mat box 0.08 0.02 0.008\
| xform -t -0.185 -0.01 0.142
!genprism glass mat prism 3 0. 0 0.08 \
```

```
0
0
12
0.105  0.10   0.00
0.185  0.01   0.00
0.185  0.01   0.12
0.105  0.10   0.12
outerreactor_mat polygon frond3r_rad
0
0
12
0.105  -0.10  0.00
0.185  -0.01  0.00
0.185  -0.01  0.12
0.105  -0.10  0.12
outerreactor_mat polygon back2r_rad
0
0
12
-0.105 0.10   0.00
-0.185 0.01   0.00
-0.185 0.01   0.12
-0.105 0.10   0.12
outerreactor_mat polygon back3r_rad
0
0
12
-0.105 -0.10  0.00
-0.185 -0.01  0.00
-0.185 -0.01  0.12
-0.105 -0.10  0.12
outerreactor_mat polygon back2r_rad
0
0
12
-0.105 0.10   0.00
0.105  0.10   0.00
0.105  0.10   0.12
-0.105 0.10   0.12
outerreactor_mat polygon back3r_rad
0
0
12
-0.105 -0.10  0.00
0.105  -0.10  0.00
0.105  -0.10  0.12
-0.105 -0.10  0.12
outerreactor_mat polygon floor2r_rad
0
0
54
0.12   -0.13  0.12
0.22   -0.02  0.12
0.22   0.02   0.12
0.12   0.13   0.12
-0.12  0.13   0.12
-0.22  0.02   0.12
-0.22  -0.02  0.12
-0.12  -0.13  0.12
-0.105 -0.10  0.12
0.105  -0.10  0.12
0.185  -0.01  0.12
0.185  0.01   0.12
0.105  0.10   0.12
-0.105 0.10   0.12
-0.185 0.01   0.12
-0.185 -0.01  0.12
-0.105 -0.10  0.12
-0.12  -0.13  0.12
outerreactor_mat polygon frond12r_rad
0
0
12
0.22   0.02   0.12
0.22   0.02   0.15
0  0  0.09  -l  0  0  -0.008| xform  -t  0.105\
0.01 0.15 -a 2 -my -a 2 -mx
interface_mat polygon interface1_rad
0
0
12
0.105  -0.10  0.150
0.105  -0.10  0.142
0.105  0.10   0.142
0.105  0.10   0.150
interface_mat polygon interface2_rad
0
0
12
-0.105 -0.10  0.150
-0.105 -0.10  0.142
-0.105 0.10   0.142
-0.105 0.10   0.150
interface_mat polygon interface3_rad
0
0
12
-0.185 -0.01  0.150
-0.185 -0.01  0.142
-0.105 -0.01  0.142
-0.105 -0.01  0.150
interface_mat polygon interface4_rad
0
0
12
-0.185 0.01   0.150
-0.185 0.01   0.142
-0.105 0.01   0.142
-0.105 0.01   0.150
interface_mat polygon interface5_rad
0
0
12
0.185  0.01   0.150
0.185  0.01   0.142
0.105  0.01   0.142
0.105  0.01   0.150
interface_mat polygon interface6_rad
0
0
12
0.185  -0.01  0.150
0.185  -0.01  0.142
0.105  -0.01  0.142
0.105  -0.01  0.150
outerreactor_mat polygon specborder1_rad
0
0
12
0.105  -0.1   0.15
0.185  -0.01  0.15
0.185  -0.01  0.139
0.105  -0.1   0.139
outerreactor_mat polygon specborder2_rad
0
0
12
0.105  0.1    0.15
0.185  0.01   0.15
0.185  0.01   0.139
0.105  0.1    0.139
outerreactor_mat  polygon specborder3_rad
0
0
12
-0.105 -0.1   0.15
-0.185 -0.01  0.15
-0.185 -0.01  0.139
-0.105 -0.1   0.139
outerreactor mat  polygon specborder4 rad
```

```
0.22   -0.02  0.15
0.22   -0.02  0.12
outerreactor_mat polygon back12r_rad
0
0
12
-0.22  0.02   0.12
-0.22  0.02   0.15
-0.22  -0.02  0.15
-0.22  -0.02  0.12
outerreactor_mat polygon frond22r_rad
0
0
12
0.12   0.13   0.12
0.22   0.02   0.12
0.22   0.02   0.15
0.12   0.13   0.15
catalyst_nonactive_mat polygon ctn4_rad
0
0
12
0.110  0.0435 0.139
0.110  0.05   0.139
-0.110 0.05   0.139
-0.110 0.0435 0.139
!genrbox outerreactor_mat box 0.210 0.05\
0.00299 | xform -t -0.105 -0.10 0.139
!genrbox outerreactor_mat box 0.210\
-0.05  0.00299  |  xform  -t  -0.105  0.10\
0.139
outerreactor_mat polygon frond32r_rad
0
0
12
0.12   -0.13  0.12
0.22   -0.02  0.12
0.22   -0.02  0.15
0.12   -0.13  0.15
outerreactor_mat polygon back22r_rad
0
0
12
-0.12  0.13   0.12
-0.22  0.02   0.12
-0.22  0.02   0.15
-0.12  0.13   0.15
outerreactor_mat polygon back32r_rad
0
0
12
-0.12  -0.13  0.12
-0.22  -0.02  0.12
-0.22  -0.02  0.15
-0.12  -0.13  0.15
outerreactor_mat polygon back22r_rad
0
0
12
-0.12  0.13   0.12
0.12   0.13   0.12
0.12   0.13   0.15
-0.12  0.13   0.15
outerreactor_mat polygon back32r_rad
0
0
12
-0.12  -0.13  0.12
0.12   -0.13  0.12
0.12   -0.13  0.15
-0.12  -0.13  0.15
outerreactor_mat polygon ceiling1r_rad
0
0
54
0
0
12
-0.105 0.1    0.15
-0.185 0.01   0.15
-0.185 0.01   0.139
-0.105 0.1    0.139
outerreactor_mat polygon specborder5_rad
0
0
12
-0.185 -0.01  0.15
-0.185 0.01   0.15
-0.185 0.01   0.139
-0.185 -0.01  0.139
outerreactor_mat  polygon specborder6_rad
0
0
12
0.185  -0.01  0.15
0.185  0.01   0.15
0.185  0.01   0.139
0.185  -0.01  0.139
outerreactor_mat  polygon specborder7_rad
0
0
12
-0.105 -0.1   0.15
0.105  -0.1   0.15
0.105  -0.1   0.139
-0.105 -0.1   0.139
outerreactor_mat  polygon specborder8_rad
0
0
12
-0.105 0.1    0.15
0.105  0.1    0.15
0.105  0.1    0.139
-0.105 0.1    0.139
innerreactor_mat polygon inside1_rad
0
0
12
0.110  0.1    0.139
0.185  0.01   0.139
0.185  -0.01  0.139
0.110  -0.1   0.139
innerreactor_mat polygon inside2_rad
0
0
12
-0.110 0.1    0.139
-0.185 0.01   0.139
-0.185 -0.01  0.139
-0.110 -0.1   0.139
outerreactor_mat polygon bordercat1_rad
0
0
12
0.105  -0.1   0.139
0.105  0.1    0.139
0.110  0.1    0.139
0.110  -0.1   0.139
outerreactor_mat polygon bordercat2_rad
0
0
12
-0.105 -0.1   0.139
-0.105 0.1    0.139
-0.110 0.1    0.139
-0.110 -0.1   0.139
catalyst_nonactive_mat polygon catn1_rad
0
0
12
```

```
0.12   -0.13  0.15
0.22   -0.02  0.15
0.22   0.02   0.15
0.12   0.13   0.15
-0.12  0.13   0.15
-0.22  0.02   0.15
-0.22  -0.02  0.15
-0.12  -0.13  0.15
-0.105 -0.10  0.15
0.105  -0.10  0.15
0.185  -0.01  0.15
0.185  0.01   0.15
0.105  0.10   0.15
-0.105 0.10   0.15
-0.185 0.01   0.15
-0.185 -0.01  0.15
-0.105 -0.10  0.15
-0.12  -0.13  0.15
```

```
0.096  -0.1   0.139
0.096  0.1    0.139
0.105  0.1    0.139
0.105  -0.1   0.139
catalyst_nonactive_mat polygon catn2_rad
0
0
12
-0.092 -0.1   0.139
-0.092 0.1    0.139
-0.105 0.1    0.139
-0.105 -0.1   0.139
catalyst_mat polygon catalyst_rad
0
0
12
0.096  -0.0435      0.139
0.096  0.0435 0.139
-0.092 0.0435 0.139
-0.092 -0.0435      0.139
catalyst_nonactive_mat polygon catn3_rad
0
0
12
0.110  -0.0435      0.139
0.110  -0.05  0.139
-0.110 -0.05  0.139
-0.110 -0.0435      0.139
```

Appendix 3. The ideal flow model

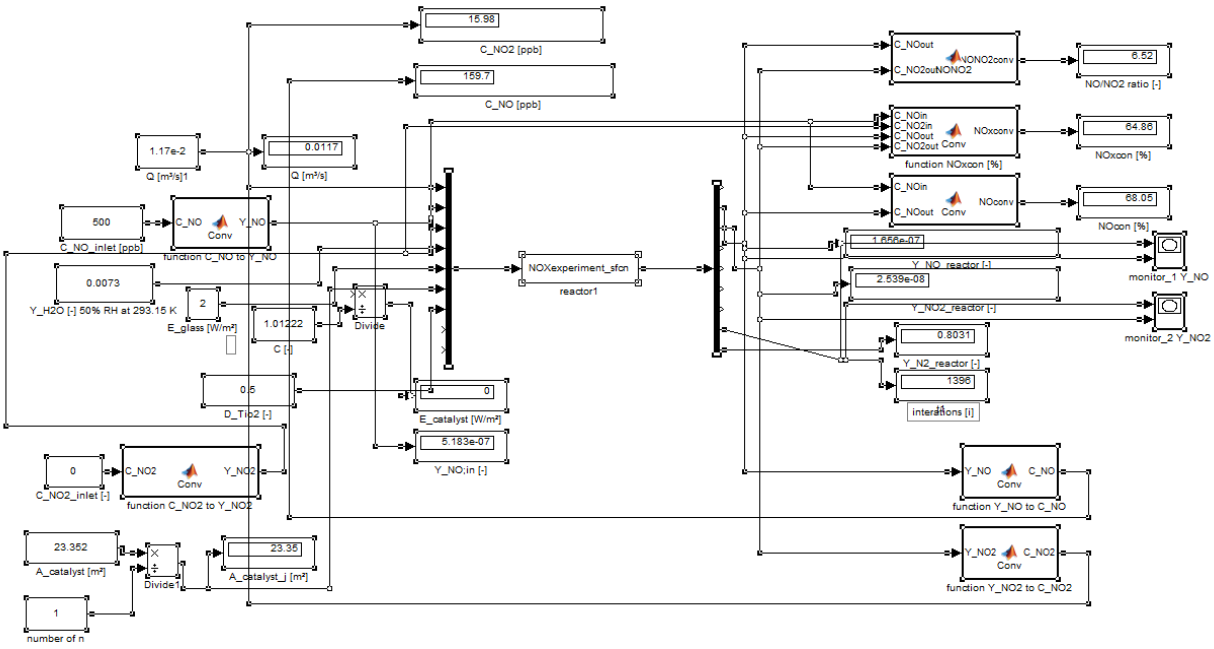

Figure 71: The Simulink model of the ideally mixed room model. The model can also be used to calculate the plug flow reactor by linking multiple *reactor1* nodes in series for the forward discretization routine.

The *NOexperiments_sfcn.m* file is written as:

```
function [sys,x0,str,ts] = NOXexperiment_sfcn(t,x,u,flag)
switch flag,
case 0,
[sys,x0,str,ts]=mdlInitializeSizes;
case 1,
sys=mdlDerivatives(t,x,u);
case 3,
sys=mdlOutputs(t,x,u);
case { 2, 4, 9 },
sys = [];
otherwise
error(['Unhandled flag = ',num2str(flag)]);
end

function [sys,x0,str,ts]=mdlInitializeSizes
sizes = simsizes;
sizes.NumContStates = 3;
sizes.NumDiscStates = 0;
sizes.NumOutputs = 9;
sizes.NumInputs = 9;
sizes.DirFeedthrough = 1;
sizes.NumSampleTimes = 1;
sys = simsizes(sizes);
x0 = [1e-6; 1e-7; 0.8]; % tweak to get better initial values
str = [];
ts = [0 0];

function sys=mdlDerivatives(t,x,u)
```

```
% Set input variables
Q_in=u(1);           % volumetric flow rate [m\.b3/s]
Y_no_in=u(2);        % mass fraction NO inlet [-]
Y_no2_in=u(3);       % mass fraction NO2 inlet [-]
Y_h2o_in=u(4);       % mass fraction H2O inlet [-]
E_s=u(5);            % average irradiance on the photocatalyst [W/m²]
A_catalyst=u(6);     % area photocatalyst [m²]
D_tio2=u(7);         % dosage [m²]
% rate constants
k_no=5.35e-13;      % [m²/(mol s)]
k_no2=1.98e-11;     % [m²/(mol s)]
K_no=2.09e1;        % [m³/(mol)]
K_no2=5.38;         % [m³/(mol)]
K_h2o=2.39e-3;      % [m³/(mol)]
alpha=7.30e-6;      % [mol/(W s)]ab5
beta=1.03333e-7;    % [mol (m²s)]
% other constants
rho_air=1.204;      % [kg/m³] density air at 293.15 kelvin
M_no=0.03000615;    % [kg/mol] molar mass
M_no2=0.04600558;   % [kg/mol] molar mass
M_h2o=0.01801532;   % [kg/mol] molar mass of water at 50% Rh at 293.15 Kelvin
Y_o2=0.189581;      % [-] mass percentage oxygen
V=1;                % [m³] volume room (has no influence in final answer)

% Defining matrix x
xdot=zeros(3,1);    % zeros(n,m)  n=rows m=columns

% x(1) = Y_no _reactor, x(2)=Y_no2 _reactor, x(3)=Y_n2 _reactor
C_NO=rho_air/M_no*x(1);
C_NO2=rho_air/M_no2*x(2);
C_H2O=rho_air/M_h2o*Y_h2o_in;

term1=(1+(4*alpha*E_s*(1+K_no*C_NO+K_no2*C_NO2+K_h2o*C_H2O))/(beta*K_h2o*C_H2
O))^0.5-1;
term2=(4*k_no*K_no*C_NO+2*k_no2*K_no2*C_NO2)*(1+K_no*C_NO+K_no2*C_NO2+K_h2o*C
_H2O);
term3=-k_no*K_no*C_NO*K_h2o*C_H2O*beta;
term4=(k_no*K_no*C_NO-k_no2*K_no2*C_NO2)*K_h2o*C_H2O*beta;

xdot(1)=(Q_in*rho_air/M_no*(Y_no_in-x(1))
+A_catalyst*(term3*term1/term2)*D_tio2)/V;
xdot(2)=(Q_in*rho_air/M_no2*(Y_no2_in-
x(2))+A_catalyst*(term4*term1/term2)*D_tio2)/V;
xdot(3)=1-x(1)-x(2)-x(3)-Y_h2o_in-Y_o2;
sys = xdot;

function sys=mdlOutputs(t,x,u)
sys = [u(1); x(1); x(2); u(4) ; u(5); u(6) ; u(7) ; t ; x(3)];
```

Appendix 4. Reactor model comparison with experiments

Table 27: The numerical data of the reactor model (Section 5.3.2) with which the experimental results [3] are estimated.

	Experimental results							Simulation	
	E_s [Wm^{-2}]	Q [L/min]	RH [%]	$C_{NO;in}$ [ppb]	$C_{NO2;in}$ [ppb]	$C_{NO;out}$ [ppb]	$C_{NO2;out}$ [ppb]	$C_{NO;out}$ [ppb]	$C_{NO2;out}$ [ppb]
1	3	3	50	983.1	10.2	877.3	33.6	898.2	60.4
2	5	3	50	975.5	9.7	832.7	41.2	868.5	66.7
3	8	3	50	999.3	11.6	820	51.3	867.3	73.7
4	10	3	50	976.6	11.6	779.1	52.4	831.4	74.6
5	13	3	50	980.5	12.9	766.9	58.2	817.1	77.1
6	1	3	50	482.7	4.7	433	16.1	434.4	31.7
7	2	3	50	496.7	7.7	408.9	27.3	431.3	37.1
8	4	3	50	493.3	3.6	392.2	29.6	402.8	39.0
9	6	3	50	482.8	3.6	362.6	34.4	357.1	38.5
10	8	3	50	469.1	10.9	341.9	44.3	348.7	38.0
11	10	3	50	493.3	13.6	356.5	49.3	359.9	39.7
12	13	3	50	476	16.2	325.7	51.9	327.1	37.0
13	10	1	50	472.7	1.5	141.6	36.8	95.9	11.2
14	10	2	50	487.6	4.7	270.3	48	286.4	33.1
15	10	3	50	493.3	13.6	356.5	49.3	360.1	39.7
16	10	5	50	492.9	0.1	399.1	27.7	405.5	38.1
17	10	3	10	489.5	0.3	435.9	11	422.1	35.2
18	10	3	20	497.6	4.5	420.7	21.1	407.2	39.4
19	10	3	30	485.2	0.5	400.3	17.6	376.0	38.7
20	10	3	40	496.4	5.4	377.6	34.9	373.5	39.9
21	10	3	50	493.3	13.6	356.5	49.3	360.1	39.7
22	10	3	60	484.6	11.6	306.4	53.6	339.4	38.0
23	10	3	70	485.9	4.2	287.2	49.3	326.4	36.8

Appendix 5. Radiance model of the benchmark room

Materials (*.mat)

```
# black reference floor
void metal blackfloor_mat
0
0
5 0.2 0.2 0.2 0 0
# R G B spec rough

# catalyst-coated wall/ceiling
void metal catalyst_mat
0
0
5 0.883 0.883 0.883 0 0

# Mirrors in the the luminaire
void metal mirror_mat
0
0
5 0.845 0.845 0.845 0.85 0

# Light1
void light lighting_mat
0
0
3 LR1 LB1 LG1
```

```
# Black paper/black
void metal black_mat
0
0
5 0.042 0.042 0.042 0.01 0

# Luminaire casing
void metal luminairecasing_mat
0
0
5 0.713 0.713 0.713 0.03 0

# Light2
void light lighting_2_mat
0
0
3 LR2 LB2 LG2

# Ideal mirror
void mirror idealmirror_mat
0
0
3 1 1 1
```

Room geometry (room_model.rad)

```
blackfloor_mat polygon floor_rad
0
0
12
3      4.7    0.00
3      -4.5   0.00
-3     -4.5   0.00
-3     4.7    0.00
catalyst_mat polygon ceilling_rad
0
0
12
3      4.5    3
3      -4.7   3
-3     -4.7   3
-3     4.5    3
catalyst_mat polygon extra1_rad
0
0
12
3      -4.5   2.832
3      -4.7   2.832
-3     -4.7   2.832
-3     -4.5   2.832
catalyst_mat polygon extra2_rad
0
0
12
3      4.5    0.48
3      4.7    0.48
-3     4.7    0.48
-3     4.5    0.48
absorber_mat polygon abs1_rad
0
0
12
3      4.7    0.0
3      4.7    0.48
-3     4.7    0.48
-3     4.7    0.0
```

```
absorber_mat polygon abs2_rad
0
0
12
3      -4.7   3
3      -4.7   2.832
-3     -4.7   2.832
-3     -4.7   3
catalyst_mat polygon back_rad
0
0
12
-3     -4.5   0
-3     -4.5   2.832
3      -4.5   2.832
3      -4.5   0
catalyst_mat polygon front_rad
0
0
12
-3     4.5    3
-3     4.5    0.48
3      4.5    0.48
3      4.5    3
idealmirror_mat polygon left_rad
0
0
12
-0.8   4.7    3
-0.8   -4.7   3
-0.8   -4.7   0
-0.8   4.7    0
idealmirror_mat polygon right_rad
0
0
12
0.8    4.7    0
0.8    -4.7   0
0.8    -4.7   3
0.8    4.7    3
!xform -rz 90 -t 0 -3.8 3 -a 5 -t 0 1.9 0
luminaire single.rad
```

Luminaire_single geometry (luminaire_single.rad)

```
luminairecasing_mat polygon ceilingls_rad
0
0
12
-0.098333 -0.590 0.085
-0.098333 0.590     0.085
0.098333 0.590      0.085
0.098333 -0.590     0.085
antimatter_cat_mat polygon anti_rad
0
0
12
-0.098333 -0.590 0
-0.098333 0.590     0
0.098333 0.590      0
0.098333 -0.590     0
luminairecasing_mat polygon leftls_rad
0
0
12
-0.098333 0.590     0.00
-0.098333 0.590     0.085
-0.098333 -0.590    0.085
-0.098333 -0.590    0.00
!xform lightsource_single.rad
!xform -t -0.098333 -0.295 0.00 -a 2 -rz
180 -t 0 0 0 -a 2 -my mirrorII.rad
```

```
luminairecasing_mat polygon rightls_rad
0
0
12
0.098333 -0.590     0.00
0.098333 -0.590     0.085
0.098333 0.590      0.085
0.098333 0.590      0.00
luminairecasing_mat polygon frontls_rad
0
0
12
-0.098333 0.590     0.00
-0.098333 0.590     0.085
0.098333 0.590      0.085
0.098333 0.590      0.00
luminairecasing_mat polygon backls_rad
0
0
12
-0.098333  -0.590   0.00
-0.098333 -0.590    0.085
0.098333 -0.590            0.085
0.098333 -0.590            0.00
!xform -rz -90 -t 0 0.590 0.00 -a 7 -t 0 -
0.098333 0 -a 2 -rz 180 mmirrorI_small.rad
```

Lightsource geometry (lightsource_single.rad)

```
lighting_2_mat cylinder lighta_rad
0
0
7
0      -0.574 0.059
0      -0.549 0.059
0.014
lighting_2_mat cylinder lightb_rad
0
0
7
0      0.549  0.059
0      0.574  0.059
0.014
lighting_mat cylinder light1_rad
0
0
7
0      -0.549 0.059
0      0      0.059
0.014
lighting_mat cylinder light2_rad
0
0
7
0      0      0.059
0      0.549  0.059
0.014
black_mat cylinder c1_rad
0
0
7
0      -0.590 0.059
0      -0.574 0.059
0.014
black_mat cylinder c2_rad
0
0
7
0      0.574  0.059
0      0.590  0.059
0.014
```

Mirror (type I) geometry (mirrorI.rad)

```
mirror_mat polygon ceilingm_rad
0
0
12
0.00   -0.098333 0.04
0.005  -0.098333 0.04
0.005  0.098333 0.04
0.00   0.098333 0.04
!gensurf        mirror_mat        sidem_rad
'0.0045*s^2.5' '0.19667*t' '0.04*s' 25 25
| xform -t 0.0005 -0.098333 0
mirror_mat polygon sideat_rad
0
0
12
0.00   -0.098333    0.00
0.0005 -0.098333    0.00
0.0005 0.098333     0.00
0.00   0.098333
```

Mirror (type II) geometry (mirrorII.rad)

```
black_mat polygon ceilingt_rad
0
0
12
0.00   -0.295 0.08
0.04875      -0.295 0.08
0.04875      0.295  0.08
0.00   0.295  0.08
!gensurf        mirror_mat        mirror\
'0.0487*(0.77606*s^4-\
0.5951*s^3+0.4611*s^2+0.3698*s)'
'0.590*t'\  '0.08*s'  25  25  |  xform  -t
0.0005 -0.295 0
mirror_mat polygon sideat_rad
0
0
12
0.00   -0.295 0.00
0.0005 -0.295 0.00
0.0005 0.295  0.00
0.00   0.295  0.00   0.00
```

Data points working plane

```
.0001  -4 .8 0 0 1
.0001  -3 .8 0 0 1
.0001  -2 .8 0 0 1
.0001  -1 .8 0 0 1
.0001  0 .8 0 0 1
.0001  1 .8 0 0 1
.0001  2 .8 0 0 1
.0001  3 .8 0 0 1
.0001  4 .8 0 0 1
```

```
.4 -4 .8 0 0 1
.4 -3 .8 0 0 1
.4 -2 .8 0 0 1
.4 -1 .8 0 0 1
.4 0  .8 0 0 1
.4 1  .8 0 0 1
.4 2  .8 0 0 1
.4 3  .8 0 0 1
.4 4  .8 0 0 1
```

```
.7999 -4 .8 0 0 1
.7999 -3 .8 0 0 1
.7999 -2 .8 0 0 1
.7999 -1 .8 0 0 1
.7999 0  .8 0 0 1
.7999 1  .8 0 0 1
.7999 2  .8 0 0 1
.7999 3  .8 0 0 1
.7999 4  .8 0 0 1
```

Other data points

```
.001 -4.49999 .00001 0 0 1
.001 -4 .00001 0 0 1
.001 -3.5 .00001 0 0 1
.001 -3 .00001 0 0 1
.001 -2.5 .00001 0 0 1
.001 -2 .00001 0 0 1
.001 -1.5 .00001 0 0 1
.001 -1 .00001 0 0 1
.001 -.5 .00001 0 0 1
.001 0 .00001 0 0 1
.001 .5 .00001 0 0 1
.001 1 .00001 0 0 1
.001 1.5 .00001 0 0 1
.001 2 .00001 0 0 1
.001 2.5 .00001 0 0 1
.001 3 .00001 0 0 1
.001 3.5 .00001 0 0 1
.001 4 .00001 0 0 1
.001 4.49999 .00001 0 0 1
.4 -4.49999 .00001 0 0 1
.4 -4 .00001 0 0 1
.4 -3.5 .00001 0 0 1
.4 -3 .00001 0 0 1
.4 -2.5 .00001 0 0 1
.4 -2 .00001 0 0 1
.4 -1.5 .00001 0 0 1
.4 -1 .00001 0 0 1
.4 -.5 .00001 0 0 1
.4 0 .00001 0 0 1
.4 .5 .00001 0 0 1
.4 1 .00001 0 0 1
.4 1.5 .00001 0 0 1
.4 2 .00001 0 0 1
.4 2.5 .00001 0 0 1
.4 3 .00001 0 0 1
.4 3.5 .00001 0 0 1
.4 4 .00001 0 0 1
.4 4.49999 .00001 0 0 1
.79999 -4.49999 .00001 0 0
1
.79999 -4 .00001 0 0 1
.79999 -3.5 .00001 0 0 1
.79999 -3 .00001 0 0 1
.79999 -2.5 .00001 0 0 1
.79999 -2 .00001 0 0 1
.79999 -1.5 .00001 0 0 1
.79999 -1 .00001 0 0 1
.79999 -.5 .00001 0 0 1
.79999 0 .00001 0 0 1
.79999 .5 .00001 0 0 1
.79999 1 .00001 0 0 1
.79999 1.5 .00001 0 0 1
.79999 2 .00001 0 0 1
.79999 2.5 .00001 0 0 1
.79999 3 .00001 0 0 1
.79999 3.5 .00001 0 0 1
.79999 4 .00001 0 0 1
.79999 4.49999 .00001 0 0 1

.001 -4.49999 2.99999 0 0 -
1
.001 -4 2.99999 0 0 -1
```

```
.4 2.5 2.99999 0 0 -1
.4 3 2.99999 0 0 -1
.4 3.5 2.99999 0 0 -1
.4 4 2.99999 0 0 -1
.4 4.49999 2.99999 0 0 -1
.79999 -4.49999 2.99999 0 0
-1
.79999 -4 2.99999 0 0 -1
.79999 -3.5 2.99999 0 0 -1
.79999 -3 2.99999 0 0 -1
.79999 -2.5 2.99999 0 0 -1
.79999 -2 2.99999 0 0 -1
.79999 -1.5 2.99999 0 0 -1
.79999 -1 2.99999 0 0 -1
.79999 -.5 2.99999 0 0 -1
.79999 0 2.99999 0 0 -1
.79999 .5 2.99999 0 0 -1
.79999 1 2.99999 0 0 -1
.79999 1.5 2.99999 0 0 -1
.79999 2 2.99999 0 0 -1
.79999 2.5 2.99999 0 0 -1
.79999 3 2.99999 0 0 -1
.79999 3.5 2.99999 0 0 -1
.79999 4 2.99999 0 0 -1
.79999 4.49999 2.99999 0 0
-1
.00001 4.49999 .25 0 -1 0
.00001 4.49999 .375 0 -1 0
.00001 4.49999 .5 0 -1 0
.00001 4.49999 .625 0 -1 0
.00001 4.49999 .75 0 -1 0
.00001 4.49999 .875 0 -1 0
.00001 4.49999 1.00 0 -1 0
.00001 4.49999 1.125 0 -1 0
.00001 4.49999 1.25 0 -1 0
.00001 4.49999 1.375 0 -1 0
.00001 4.49999 1.5 0 -1 0
.00001 4.49999 1.625 0 -1 0
.00001 4.49999 1.75 0 -1 0
.00001 4.49999 1.875 0 -1 0
.00001 4.49999 2.0 0 -1 0
.00001 4.49999 2.125 0 -1 0
.00001 4.49999 2.25 0 -1 0
.00001 4.49999 2.375 0 -1 0
.00001 4.49999 2.5 0 -1 0
.00001 4.49999 2.625 0 -1 0
.00001 4.49999 2.75 0 -1 0
.00001 4.49999 2.875 0 -1 0
.00001 4.49999 2.99999 0 -1
0
.4 4.49999 .00001 0 -1 0
.4 4.49999 .125 0 -1 0
.4 4.49999 .25 0 -1 0
.4 4.49999 .375 0 -1 0
.4 4.49999 .5 0 -1 0
.4 4.49999 .625 0 -1 0
.4 4.49999 .75 0 -1 0
.4 4.49999 .875 0 -1 0
.4 4.49999 1.00 0 -1 0
.4 4.49999 1.125 0 -1 0
.4 4.49999 1.25 0 -1 0
.4 4.49999 1.375 0 -1 0
```

```
.79999 4.49999 2.125 0 -1 0
.79999 4.49999 2.25 0 -1 0
.79999 4.49999 2.375 0 -1 0
.79999 4.49999 2.5 0 -1 0
.79999 4.49999 2.625 0 -1 0
.79999 4.49999 2.75 0 -1 0
.79999 4.49999 2.875 0 -1 0
.79999 4.49999 2.99999 0 -1
0
.00001 -4.49999 .00001 0 1
0
.00001 -4.49999 .125 0 1 0
.00001 -4.49999 .25 0 1 0
.00001 -4.49999 .375 0 1 0
.00001 -4.49999 .5 0 1 0
.00001 -4.49999 .625 0 1 0
.00001 -4.49999 .75 0 1 0
.00001 -4.49999 .875 0 1 0
.00001 -4.49999 1.00 0 1 0
.00001 -4.49999 1.125 0 1 0
.00001 -4.49999 1.25 0 1 0
.00001 -4.49999 1.375 0 1 0
.00001 -4.49999 1.5 0 1 0
.00001 -4.49999 1.625 0 1 0
.00001 -4.49999 1.75 0 1 0
.00001 -4.49999 1.875 0 1 0
.00001 -4.49999 2.0 0 1 0
.00001 -4.49999 2.125 0 1 0
.00001 -4.49999 2.25 0 1 0
.00001 -4.49999 2.375 0 1 0
.00001 -4.49999 2.5 0 1 0
.00001 -4.49999 2.625 0 1 0
.00001 -4.49999 2.75 0 1 0
.00001 -4.49999 2.875 0 1 0
.00001 -4.49999 2.99999 0 1
0
.4 -4.49999 .00001 0 1 0
.4 -4.49999 .125 0 1 0
.4 -4.49999 .25 0 1 0
.4 -4.49999 .375 0 1 0
.4 -4.49999 .5 0 1 0
.4 -4.49999 .625 0 1 0
.4 -4.49999 .75 0 1 0
.4 -4.49999 .875 0 1 0
.4 -4.49999 1.00 0 1 0
.4 -4.49999 1.125 0 1 0
.4 -4.49999 1.25 0 1 0
.4 -4.49999 1.375 0 1 0
.4 -4.49999 1.5 0 1 0
.4 -4.49999 1.625 0 1 0
.4 -4.49999 1.75 0 1 0
.4 -4.49999 1.875 0 1 0
.4 -4.49999 2.0 0 1 0
.4 -4.49999 2.125 0 1 0
.4 -4.49999 2.25 0 1 0
.4 -4.49999 2.375 0 1 0
.4 -4.49999 2.5 0 1 0
.4 -4.49999 2.625 0 1 0
.4 -4.49999 2.75 0 1 0
.4 -4.49999 2.875 0 1 0
.4 -4.49999 2.99999 0 1 0
.79999 -4.49999 .00001 0 1
```

```
.001 -3.5 2.99999 0 0 -1
.001 -3 2.99999 0 0 -1
.001 -2.5 2.99999 0 0 -1
.001 -2 2.99999 0 0 -1
.001 -1.5 2.99999 0 0 -1
.001 -1 2.99999 0 0 -1
.001 -.5 2.99999 0 0 -1
.001 0 2.99999 0 0 -1
.001 .5 2.99999 0 0 -1
.001 1 2.99999 0 0 -1
.001 1.5 2.99999 0 0 -1
.001 2 2.99999 0 0 -1
.001 2.5 2.99999 0 0 -1
.001 3 2.99999 0 0 -1
.001 3.5 2.99999 0 0 -1
.001 4 2.99999 0 0 -1
.001 4.49999 2.99999 0 0 -1
.4 -4.49999 2.99999 0 0 -1
.4 -4 2.99999 0 0 -1
.4 -3.5 2.99999 0 0 -1
.4 -3 2.99999 0 0 -1
.4 -2.5 2.99999 0 0 -1
.4 -2 2.99999 0 0 -1
.4 -1.5 2.99999 0 0 -1
.4 -1 2.99999 0 0 -1
.4 -.5 2.99999 0 0 -1
.4 0 2.99999 0 0 -1
.4 .5 2.99999 0 0 -1
.4 1 2.99999 0 0 -1
.4 1.5 2.99999 0 0 -1
.4 2 2.99999 0 0 -1
.4 4.49999 1.5 0 -1 0
.4 4.49999 1.625 0 -1 0
.4 4.49999 1.75 0 -1 0
.4 4.49999 1.875 0 -1 0
.4 4.49999 2.0 0 -1 0
.4 4.49999 2.125 0 -1 0
.4 4.49999 2.25 0 -1 0
.4 4.49999 2.375 0 -1 0
.4 4.49999 2.5 0 -1 0
.4 4.49999 2.625 0 -1 0
.4 4.49999 2.75 0 -1 0
.4 4.49999 2.875 0 -1 0
.4 4.49999 2.99999 0 -1 0
.79999 4.49999 .00001 0 -1
0
.79999 4.49999 .125 0 -1 0
.79999 4.49999 .25 0 -1 0
.79999 4.49999 .375 0 -1 0
.79999 4.49999 .5 0 -1 0
.79999 4.49999 .625 0 -1 0
.79999 4.49999 .75 0 -1 0
.79999 4.49999 .875 0 -1 0
.79999 4.49999 1.00 0 -1 0
.79999 4.49999 1.125 0 -1 0
.79999 4.49999 1.25 0 -1 0
.79999 4.49999 1.375 0 -1 0
.79999 4.49999 1.5 0 -1 0
.79999 4.49999 1.625 0 -1 0
.79999 4.49999 1.75 0 -1 0
.79999 4.49999 1.875 0 -1 0
.79999 4.49999 2.0 0 -1 0
0
.79999 -4.49999 .125 0 1 0
.79999 -4.49999 .25 0 1 0
.79999 -4.49999 .375 0 1 0
.79999 -4.49999 .5 0 1 0
.79999 -4.49999 .625 0 1 0
.79999 -4.49999 .75 0 1 0
.79999 -4.49999 .875 0 1 0
.79999 -4.49999 1.00 0 1 0
.79999 -4.49999 1.125 0 1 0
.79999 -4.49999 1.25 0 1 0
.79999 -4.49999 1.375 0 1 0
.79999 -4.49999 1.5 0 1 0
.79999 -4.49999 1.625 0 1 0
.79999 -4.49999 1.75 0 1 0
.79999 -4.49999 1.875 0 1 0
.79999 -4.49999 2.0 0 1 0
.79999 -4.49999 2.125 0 1 0
.79999 -4.49999 2.25 0 1 0
.79999 -4.49999 2.375 0 1 0
.79999 -4.49999 2.5 0 1 0
.79999 -4.49999 2.625 0 1 0
.79999 -4.49999 2.75 0 1 0
.79999 -4.49999 2.875 0 1 0
.79999 -4.49999 2.99999 0 1
0
.00001 4.49999 .00001 0 -1
0
.00001 4.49999 .125 0 -1 0
```

Appendix 6. User defined functions

```
/************************************************************************
Total species source/sink -
R.S. Pelzers 20130221
************************************************************************/

#include "udf.h"

#define MWNO 0.030 /* all molecular weights in (kg mol-1)*/
#define MWNO2 0.046
#define MWH2O 0.018
#define kNO 5.35e-13  /* all k's in (m2 mol-1 s-1)*/
#define kNO2 1.98e-11
#define KNO 2.09e1    /* all K's in (m3 mol-1)*/
#define KNO2 5.38
#define KH2O 2.39e-3
#define ALPHA 7.30e-6/* constant (mol W-1 s-1)*/
#define BETA 1.03e-7 /* constant (mol m-2 s-1)*/
#define E 10 /*irradiance W m-2*/
#define DTiO2 0.02 /*Photocatalyst content (g g-1); 0.5 standard*/
#define H 0.001 /* The cell height*/

/* added since 20121015 */
#define LUX 500 /* amount of lux on the working plane lx reference is 500 */

/* this is the diffusity for the mean age of air */
DEFINE_DIFFUSIVITY(mean_age_diff, c, t, i)
{
      return C_R(c,t) * 2.88e-05 + C_MU_EFF(c,t) / 0.7;
}

/* These are the new equations for the boundaries using the E-distribution */
DEFINE_SOURCE(E_rtotal, c, t, dS, eqn)
{
 real source;
 real term1;
 real term2;
 real term3;
 real term4;
 real termi;
 real termii;
 real termiii;
 real termiv;
 real av;
 /* E-profile for the irradiance on the floor */
 real x[ND_ND]; /* this will hold the position vector */
 real EE;
/* E-profile */
 real no  = C_YI(c,t,0);   /* mass fraction of NO at the wall */
 real no2 = C_YI(c,t,1);
 real h2o = C_YI(c,t,2);  /* mass fraction of H2O at the wall */
 real rho = C_R(c,t);
/* E-profile function */
 C_CENTROID(x,c,t);        /* this returns the position vector [x,y] of a cell */
if (x[1] >= 2.999 || EE <= 0)     /* ceiling function */
 EE = (0-0.00000244510953244039*pow((x[0]),10)+ 0.00011145142672695300 *pow((x[0]),9)-
0.0021985114944393*pow((x[0]),8)+ 0.0245889835241838*pow((x[0]),7)-
0.171622830788319*pow((x[0]),6)+ 0.775410197284759*pow((x[0]),5)-
2.27627914604337*pow((x[0]),4)+4.2372194784832*pow((x[0]),3)-
4.69183100626815*pow((x[0]),2)+2.6153482876321*(x[0])+ 0.384133193790361)*(LUX/500);
else if (x[1] <= 0.001 || EE <= 0)      /* floor function */
EE = (0-0.00000209232601798189*pow((x[0]),10)+ 0.00008534826171846663*pow((x[0]),9)-
0.0014115686495716 7*pow((x[0]),8)+ 0.0118141707107383*pow((x[0]),7)-
0.0480847417902372*pow((x[0]),6)+ 0.0360472589568389*pow((x[0]),5)+
0.46642675359801*pow((x[0]),4)-1.87786375402536000000
```

```
*pow((x[0]),3)+2.87768401611508*pow((x[0]),2) -1.48299773881759 *(x[0])+
2.98223980159895)*(LUX/500);
else if ((x[0]) <= 0.001|| EE <= 0)     /* left wall function */
EE =(0-0.421028512932445*pow((x[0]),10)+6.21741344645125*pow((x[0]),9)-
38.4597230992475*pow((x[0]),8)+129.439649815647*pow((x[0]),7)-
257.485853459534*pow((x[0]),6)+307.026490879403*pow((x[0]),5)-
210.425870234103*pow((x[0]),4)+71.5702599173953*pow((x[0]),3)-
5.43447511157067*pow((x[0]),2)-2.22920716630693*(x[0])+1.72022762937749)*(LUX/500);
else if ((x[0]) >= 8.999 || EE <= 0)    /* right wall function */
EE = (0-0.581145562513808*pow((x[0]),10)+8.60682583064381*pow((x[0]),9)-
53.6238774799334*pow((x[0]),8)+ 182.902986014625*pow((x[0]),7)-
372.390832303169*pow((x[0]),6)+ 462.750849776203*pow((x[0]),5)-
343.724224903334*pow((x[0]),4)+ 141.770717628704*pow((x[0]),3)-
26.6433656056686*pow((x[0]),2)+0.849167919830689*(x[0])+ 1.5810532149876)*(LUX/500);
else
 EE = 0;
/* E-profile function */
no  *= rho/MWNO;  /* converting to molar concentrations (mol m-3) */
 no2 *= rho/MWNO2;
 h2o *= rho/MWH2O;
  term1 = -kNO*BETA*KNO*no*KH2O*h2o;
 term2 = sqrt(1 + 4*ALPHA*EE*(1 + KNO*no + KNO2*no2 + KH2O*h2o)/(BETA*KH2O*h2o)) - 1;
 term3 = 4*kNO*KNO*no + 2*kNO2*KNO2*no2;
 term4 = 1 + KNO*no + KNO2*no2 + KH2O*h2o;
 av = DTiO2/H;
  termi = (kNO*KNO*no - kNO2*KNO2*no2)*KH2O*h2o*BETA;
 termii = sqrt(1 + 4*ALPHA*EE*(1 + KNO*no + KNO2*no2 + KH2O*h2o)/(BETA*KH2O*h2o)) - 1;
 termiii = 4*kNO*KNO*no + 2*kNO2*KNO2*no2;
 termiv = 1 + KNO*no + KNO2*no2 + KH2O*h2o;
  source = av*MWNO2*(termi*termii)/(termiii*termiv) +
av*MWNO*(term1*term2)/(term3*term4);
dS[eqn]=0;
  return source;
}

DEFINE_SOURCE(E_rNO, c, t, dS, eqn)
{
 real source;
 real term1;
 real term2;
 real term3;
 real term4;
 real av;
/* E-profile for the irradiance on the floor */
 real x[ND_ND], EE;
/* E-profile */
real no  = C_YI(c,t,0);   /* mass fraction of NO at the wall */
 real no2 = C_YI(c,t,1);
 real h2o = C_YI(c,t,2);  /* mass fraction of H2O at the wall */
 real rho = C_R(c,t);
/* E-profile function */
 C_CENTROID(x,c,t);       /* this returns the position vector [x,y] of a cell */

if (x[1] >= 2.999 || EE <= 0)     /* ceiling function */
 EE = (0-0.000002445109532440 39*pow((x[0]),10)+ 0.00011145142672695300 *pow((x[0]),9)-
0.0021985114944393*pow((x[0]),8)+ 0.0245889835241838*pow((x[0]),7)-
0.171622830788319*pow((x[0]),6)+ 0.775410197284759*pow((x[0]),5)-
2.27627914604337*pow((x[0]),4)+4.2372194784832*pow((x[0]),3)-
4.69183100626815*pow((x[0]),2)+2.6153482876321*(x[0])+ 0.384133193790361)*(LUX/500);
else if (x[1] <= 0.001 || EE <= 0)      /* floor function */
EE = (0-0.000002092326017981 89*pow((x[0]),10)+ 0.000085348261718 4663*pow((x[0]),9)-
0.00141156864957167*pow((x[0]),8)+ 0.0118141707107383*pow((x[0]),7)-
0.0480847417902372*pow((x[0]),6)+ 0.0360472589568389*pow((x[0]),5)+
0.46642675359801*pow((x[0]),4)-1.87786375402536000000
*pow((x[0]),3)+2.87768401611508*pow((x[0]),2) -1.48299773881759 *(x[0])+
2.98223980159895)*(LUX/500);
```

```
else if ((x[0]) <= 0.001|| EE <= 0)     /* left wall function */
EE =(0-0.421028512932445*pow((x[0]),10)+6.21741344645125*pow((x[0]),9)-
38.4597230992475*pow((x[0]),8)+129.439649815647*pow((x[0]),7)-
257.485853459534*pow((x[0]),6)+307.026490879403*pow((x[0]),5)-
210.425870234103*pow((x[0]),4)+71.5702599173953*pow((x[0]),3)-
5.43447511157067*pow((x[0]),2)-2.22920716630693*(x[0])+1.72022762937749)*(LUX/500);
else if ((x[0]) >= 8.999 || EE <= 0)    /* right wall function */
EE = (0-0.581145562513808*pow((x[0]),10)+8.60682583064381*pow((x[0]),9)-
53.6238774799334*pow((x[0]),8)+ 182.902986014625*pow((x[0]),7)-
372.390832303169*pow((x[0]),6)+ 462.750849776203*pow((x[0]),5)-
343.724224903334*pow((x[0]),4)+ 141.770717628704*pow((x[0]),3)-
26.6433656056686*pow((x[0]),2)+0.849167919830689*(x[0])+ 1.5810532149876)*(LUX/500);
else
 EE = 0;
/* E-profile function */
no  *= rho/MWNO;  /* converting to molar concentrations (mol m-3) */
 no2 *= rho/MWNO2;
 h2o *= rho/MWH2O;
term1 = -kNO*BETA*KNO*no*KH2O*h2o;
 term2 = sqrt(1 + 4*ALPHA*EE*(1 + KNO*no + KNO2*no2 + KH2O*h2o)/(BETA*KH2O*h2o)) - 1;
 term3 = 4*kNO*KNO*no + 2*kNO2*KNO2*no2;
 term4 = 1 + KNO*no + KNO2*no2 + KH2O*h2o;
 av = DTiO2/H;
source = av*MWNO*(term1*term2)/(term3*term4);
dS[eqn]=0;
return source;
}

DEFINE_SOURCE(E_rNO2, c, t, dS, eqn)
{
 real source;
 real term1;
 real term2;
 real term3;
 real term4;
 real av;
/* E-profile for the irradiance on the floor */
 real x[ND_ND]; /* this will hold the position vector [x,y] */
 real EE;
/* E-profile */
real no  = C_YI(c,t,0);    /* mass fraction of NO at the wall */
 real no2 = C_YI(c,t,1);
 real h2o = C_YI(c,t,2);   /* mass fraction of H2O at the wall */
 real rho = C_R(c,t);
/* E-profile function */
 C_CENTROID(x,c,t);              /* this returns the position vector [x,y] of a cell
*/
if (x[1] >= 2.999 || EE <= 0)     /* ceiling function */
 EE = (0-0.00000244510953244039*pow((x[0]),10)+ 0.00011145142672695300 *pow((x[0]),9)-
0.0021985114944393*pow((x[0]),8)+ 0.0245889835241838*pow((x[0]),7)-
0.171622830788319*pow((x[0]),6)+ 0.775410197284759*pow((x[0]),5)-
2.27627914604337*pow((x[0]),4)+4.2372194784832*pow((x[0]),3)-
4.69183100626815*pow((x[0]),2)+2.6153482876321*(x[0])+ 0.384133193790361)*(LUX/500);
else if (x[1] <= 0.001 || EE <= 0)      /* floor function */
EE = (0-0.00000209232601798189*pow((x[0]),10)+ 0.00008534826171846663*pow((x[0]),9)-
0.00141156864957167*pow((x[0]),8)+ 0.0118141707107383*pow((x[0]),7)-
0.0480847417902372*pow((x[0]),6)+ 0.0360472589568389*pow((x[0]),5)+
0.46642675359801*pow((x[0]),4)-1.87786375402536000000
*pow((x[0]),3)+2.87768401611508*pow((x[0]),2) -1.48299773881759 *(x[0])+
2.98223980159895)*(LUX/500);
else if ((x[0]) <= 0.001|| EE <= 0)     /* left wall function */
EE =(0-0.421028512932445*pow((x[0]),10)+6.21741344645125*pow((x[0]),9)-
38.4597230992475*pow((x[0]),8)+129.439649815647*pow((x[0]),7)-
257.485853459534*pow((x[0]),6)+307.026490879403*pow((x[0]),5)-
210.425870234103*pow((x[0]),4)+71.5702599173953*pow((x[0]),3)-
5.43447511157067*pow((x[0]),2)-2.22920716630693*(x[0])+1.72022762937749)*(LUX/500);
```

```
else if ((x[0]) >= 8.999 || EE <= 0)    /* right wall function */
EE = (0-0.581145562513808*pow((x[0]),10)+8.60682583064381*pow((x[0]),9)-
53.6238774799334*pow((x[0]),8)+ 182.902986014625*pow((x[0]),7)-
372.390832303169*pow((x[0]),6)+ 462.750849776203*pow((x[0]),5)-
343.724224903334*pow((x[0]),4)+ 141.770717628704*pow((x[0]),3)-
26.6433656056686*pow((x[0]),2)+0.849167919830689*(x[0])+ 1.5810532149876)*(LUX/500);
else
 EE = 0;
/* E-profile function */
 no  *= rho/MWNO;  /* converting to molar concentrations (mol m-3) */
 no2 *= rho/MWNO2;
 h2o *= rho/MWH2O;
  term1 = (kNO*KNO*no - kNO2*KNO2*no2)*KH2O*h2o*BETA;
 term2 = sqrt(1 + 4*ALPHA*EE*(1 + KNO*no + KNO2*no2 + KH2O*h2o)/(BETA*KH2O*h2o)) - 1;
 term3 = 4*kNO*KNO*no + 2*kNO2*KNO2*no2;
 term4 = 1 + KNO*no + KNO2*no2 + KH2O*h2o;
 av = DTiO2/H;
  source = av*MWNO2*(term1*term2)/(term3*term4);
dS[eqn]=0;
return source;
})

/* These are the old equations used by H.Cubillos*/
DEFINE_SOURCE(rtotal, c, t, dS, eqn)
{
 real source;
 real term1;
 real term2;
 real term3;
 real term4;
 real termi;
 real termii;
 real termiii;
 real termiv;
 real av;

 real no  = C_YI(c,t,0);   /* mass fraction of NO at the wall */
 real no2 = C_YI(c,t,1);
 real h2o = C_YI(c,t,2);  /* mass fraction of H2O at the wall */

 real rho = C_R(c,t);

 no  *= rho/MWNO;  /* converting to molar concentrations (mol m-3) */
 no2 *= rho/MWNO2;
 h2o *= rho/MWH2O;

 term1 = -kNO*BETA*KNO*no*KH2O*h2o;
 term2 = sqrt(1 + 4*ALPHA*E*(1 + KNO*no + KNO2*no2 + KH2O*h2o)/(BETA*KH2O*h2o)) - 1;
 term3 = 4*kNO*KNO*no + 2*kNO2*KNO2*no2;
 term4 = 1 + KNO*no + KNO2*no2 + KH2O*h2o;
 av = DTiO2/H;

 termi = (kNO*KNO*no - kNO2*KNO2*no2)*KH2O*h2o*BETA;
 termii = sqrt(1 + 4*ALPHA*E*(1 + KNO*no + KNO2*no2 + KH2O*h2o)/(BETA*KH2O*h2o)) - 1;
 termiii = 4*kNO*KNO*no + 2*kNO2*KNO2*no2;
 termiv = 1 + KNO*no + KNO2*no2 + KH2O*h2o;

 source            =            av*MWNO2*(termi*termii)/(termiii*termiv)            +
av*MWNO*(term1*term2)/(term3*term4);
 source *= MACH;
 dS[eqn]=0;

 return source;
}


DEFINE_SOURCE(rNO, c, t, dS, eqn)
{
 real source;
 real term1;
 real term2;
 real term3;
```

```
 real term4;
 real av;

 real no  = C_YI(c,t,0);   /* mass fraction of NO at the wall */
 real no2 = C_YI(c,t,1);
 real h2o = C_YI(c,t,2);  /* mass fraction of H2O at the wall */

 real rho = C_R(c,t);

 no  *= rho/MWNO;  /* converting to molar concentrations (mol m-3) */
 no2 *= rho/MWNO2;
 h2o *= rho/MWH2O;

 term1 = -kNO*BETA*KNO*no*KH2O*h2o;
 term2 = sqrt(1 + 4*ALPHA*E*(1 + KNO*no + KNO2*no2 + KH2O*h2o)/(BETA*KH2O*h2o)) - 1;
 term3 = 4*kNO*KNO*no + 2*kNO2*KNO2*no2;
 term4 = 1 + KNO*no + KNO2*no2 + KH2O*h2o;
 av = DTiO2/H;

 source = av*MWNO*(term1*term2)/(term3*term4);
 source *= MACH;
 dS[eqn]=0;

 return source;
}

DEFINE_SOURCE(rNO2, c, t, dS, eqn)
{
 real source;
 real term1;
 real term2;
 real term3;
 real term4;
 real av;

 real no  = C_YI(c,t,0);   /* mass fraction of NO at the wall */
 real no2 = C_YI(c,t,1);
 real h2o = C_YI(c,t,2);  /* mass fraction of H2O at the wall */

 real rho = C_R(c,t);

 no  *= rho/MWNO;  /* converting to molar concentrations (mol m-3) */
 no2 *= rho/MWNO2;
 h2o *= rho/MWH2O;

 term1 = (kNO*KNO*no - kNO2*KNO2*no2)*KH2O*h2o*BETA;
 term2 = sqrt(1 + 4*ALPHA*E*(1 + KNO*no + KNO2*no2 + KH2O*h2o)/(BETA*KH2O*h2o)) - 1;
 term3 = 4*kNO*KNO*no + 2*kNO2*KNO2*no2;
 term4 = 1 + KNO*no + KNO2*no2 + KH2O*h2o;
 av = DTiO2/H;

 source = av*MWNO2*(term1*term2)/(term3*term4);
 source *= MACH;
 dS[eqn]=0;

 return source;
}
```